ELECTRODE MATERIALS FOR RECHARGEABLE LITHIUM AND SODIUM BATTERIES

A thesis presented for the award of the degree of doctor of philosophy

By

Kefei Li
B. Eng., M. Eng., M. Sci.

University of Technology, Sydney
Faculty of Science

2016

Certificate of original authorship

This thesis is the result of a research candidature conducted jointly with another University as part of a collaborative Doctoral degree. I certify that the work in this thesis has not previously been submitted for a degree nor has it been submitted as part of requirements for a degree except as part of the collaborative doctoral degree and/or fully acknowledged within the text.

I also certify that the thesis has been written by me. Any help that I have received in my research work and the preparation of the thesis itself has been acknowledged. In addition, I certify that all information sources and literature used are indicated in the thesis.

Signature of student

15 December 2016

Acknowledgements

I would like to express my deep appreciation to my principal supervisor Prof. Guoxiu Wang and co-supervisor Dr. Hao Liu for their persistent guidance and support throughout my study at University of Technology, Sydney.

I also owe my thanks to staff members and research students including Dr. Ronald Shimmon, Dr. Yueping Yao, Dr. Linda Xiao, Dr. Bing Sun, Dr. Xiaodan Huang, Dr. Dawei Su, Dr. Zhimin Ao, Dr. Shuangqiang Chen, Dr. Ying Wang, Dr. Anjon Kumar Mondal, Mr. Jinqiang Zhang, Mr. Xiuqiang Xie, Ms. Katja Kretschmer, Mr. Xin Guo, Mr. Weizhai Bao, Mr. Jianjun Song, Ms. Yufei Zhao and Ms. Jin Xu who have work with me during my study at University of Technology, Sydney. Those brilliant people helped me build up a friendly research environment which is essential for my research project. In addition, I would like to give special thanks to Dr. Dawei Su and Dr. Hao Liu for their assists on transmission electron microscopy analysis. Finally, I would like to give special thanks to Dr. Steve Bewlay for his efforts on the thesis proofreading.

Table of contents

List of figures and tables

List of abbreviations

Abbreviation	Full name
a.u.	arbitrary unit
BET	Brunauer, Emmett and Teller
CF	carbon fiber
CMC	carboxymethyl cellulose
DMC	dimethyl carbonate
DME	1,2-dimethoxyethane
DMF	N,N-Dimethylformamide
DOL	1,3-dioxolane
EIS	electrochemical impedance spectroscopy
EC	ethylene carbonate
FEC	fluoroethylene carbonate
FESEM	field emission scanning electron microscopy
GO	graphene oxide
JCPDS	Joint Committee On Powder Diffraction Standards
NMP	1-methyl-2-pyrrolidinone
PAN	polyacrylonitrile
PVA	polyvinyl alcohol
PVDF	polyvinylidene fluoride
RGO	reduced graphene oxide
SEI	solid electrolyte interphase
SEM	scanning electron microscopy
TEM	transmission electron microscopy
TGA	thermogravimetric analysis
USABC	United States Advanced Battery Consortium
VC	vinylene carbonate
XRD	X-ray diffraction

Abstract

The development of lithium-ion batteries with higher power, higher energy, longer cycle life and lower cost is the focus of battery research at present, and the situation will remain the same in the foreseeable future. The research of rechargeable batteries may lead to better understanding on interfacial chemistries, the discovery of new battery chemistries and ultimately more powerful energy storage systems. This project aims at the application of carbon based composite materials as electrode materials in rechargeable lithium or sodium batteries and potential improvement in the performance of batteries via novel design of electrode materials. The electrospinning technique, microwave-assisted solvothermal synthesis process and inert gas thermal treatment have been utilized for material preparations. A series of experiments were designed to screen the most important factors that dominates the structural features of electrospun polymer fibers. One-dimensional carbon fibers and composite materials with desired structural features have been synthesized. The carbon fiber converted from electrospun polyacrylonitrile membranes are used as negative electrode materials in lithium and sodium cells, which showed stable reversible capacities of 118 mAh/g and 84 mAh/g for lithium and sodium, respectively. The antimony-carbon fiber composite materials were synthesized as alloy type negative electrodes for lithium-ion and sodium-ion batteries. The obtained material exhibited high reversible capacities of 562 mAh/g and 371 mAh/g in lithium and sodium cells, respectively. Due to the homogeneous distribution of nanosized antimony particles within the interconnected carbon fiber networks, this materials also exhibited good rate capabilities in sodium cells as it cycled at high current rates up to 1000 mA/g without severe capacity fading. The binder-free carbon electrode was used for the synthesis of composite sulfur cathode in a novel lithium-sulfur cell design, the resulted lithium-sulfur battery demonstrated a high reversible capacity of 1101 mAh/g at a high charge-discharge current of 1000 mA/g. In addition, a two dimensional graphene-based composite material containing antimony sulfide nanoparticles synthesized via microwave-assisted solvothermal approach was also investigated as potential negative electrode materials for rechargeable lithium or sodium batteries. High reversible capacities of 595 mAh/g in lithium cells and 560 mAh/g in sodium cells from this electrode materials were achieved. The material design with graphene nanosheets as the conductive substrate was proved effective for high rate charge-discharge as this composite material showed good rate capabilities under various current rates up to 1000 mA/g.

Chapter 1 Introduction

1.1 Research motivations

Since their first commercialization in 1990s, lithium-ion batteries have become the most important power sources in a variety of applications from portable electronics to electric vehicles. Nowadays lithium-ion batteries are considered to be the defacto standard of high performance electrochemical energy storage systems due to their superior combined properties including high power, high energy, long cycle life and relatively low cost. The history of lithium-ion battery development is one of the good examples of how pure and applied research work helps improve a technology and then transform it into useful products and greatly changes the lifestyle of the human race. However, the increasing demand in the consumer market for batteries with higher energy and lower price continuously drives the development of lithium-ion battery technology towards even higher qualities such as more flexible design, lighter weight, smaller sizes, higher power capability and energy density. As the potential energy storage systems for sustainable energy harvesting and electrical vehicles, lithium-ion batteries have received much attention from government-academia as well as industrial circles. The state-of-art lithium-ion battery technology is inadequate to meet the requirement for rechargeable energy sources in electric vehicles according to the United States Advanced Battery Consortium (USABC) objectives, and the further improvement of this technology will remain a challenge for scientists in the next few decades. The joint research efforts across multiple fields are targeting new materials for lithium-ion batteries with fundamental advantages that continue pushing the boundaries of energy and power density, safety, cycle life and cost. However, despite many classes of compounds with very different reaction mechanisms being investigated as potential electrode materials for lithium-ion batteries, real gain in the energy density of batteries over the past few years has been rather limited. The energy storage capability of current lithium-ion technology is still highly dependent on cathode materials, i.e. layered structure lithium metal oxides and their transition metal substituted variants (e.g. $LiCoO_2$, $LiMnO_2$, $LiFePO_4$, $LiNi_{1/3}Mn_{1/3}Co_{1/3}O_2$, and $LiNi_{0.8}Co_{0.15}Al_{0.05}O_2$). After years of pursuit, the battery community still has not found better alternatives to intercalation chemistry, and the increasing energy density of commercial lithium-ion batteries generation after generation is mainly attributed to the engineering efforts in advanced cell design and packaging, as well as battery management systems. The development of lithium-ion batteries with higher power, higher energy, longer cycle life and lower cost will remain the focus of battery research in the future, which may lead to better understanding on interfacial chemistries, the discovery of new battery chemistries and ultimately more powerful energy storage systems.

1.2 Objectives

The electrospinning technique has been applied for the synthesis of one-dimensional nanoarchitecture functional materials with electrospun polymer fiber as the skeleton. The synthesis of 1D composites based on carbon fibers containing nanoparticles as the secondary phase can be realized via a mild reaction route. In addition, the established laboratory synthesis route can be scaled up because the application of industrial scale electrospinning is a relatively mature field. The carbon fibers derived from electrospun polymer fibers naturally form a self-coherent, binder free bulk porous structure with good electrical conductivity. This unique structural feature of electrospun carbon fibers can be utilized for synthesis of electrode materials in fundamental research on energy storage technologies.

This project focus on the application of carbon based composite materials (including one-dimensional carbon-fibers based and two-dimensional graphene-based composite materials) as negative electrode materials in rechargeable lithium or sodium batteries and the potential technical measures that can improve their anodic reactivity hence improving the performance of rechargeable lithium or sodium batteries. The research activities focused on the following areas:

- The determination of optimized electrospinning operational parameters for the desired one-dimensional structural features.
- The investigation of reaction mechanisms of carbon-based composite materials derived from electrospun polymer fibers with lithium and sodium half-cells, with special focus on the effects of additives on the general electrochemical characteristics of the resultant fibrous composite electrodes.
- The application of the electrospinning technique as a synthesis route for composite electrode materials.
- The investigation of reaction mechanisms of graphene-antimony sulfide composite materials with lithium and sodium half-cells, especially the effects of morphological features of secondary nanoparticles on the electrochemical characteristics of the resultant composite electrodes.

1.3 Research methodology

The general research strategy presented in this thesis is to synthesis nanostructure composite material with carbon fiber and/or graphene nanosheets, and evaluate their performance as electrode materials for rechargeable lithium or sodium batteries. The electrospinning, microwave-assisted solvothermal synthesis approach and subsequent inert gas annealing process are employed for composite material synthesis. The compositions of synthesized materials are then characterized with conventional ex-situ techniques including Gas adsorption surface area analysis (Brunauer, Emmett and Teller method), Raman spectroscopy, X-ray diffraction (XRD), thermogravimetric analysis (TGA). Morphology visualizations of materials are conducted by scanning electron microscopy (SEM) and transmission electron microscopy (TEM). These techniques have unique capabilities in revealing the nature of electrode material as well as electrode reactions. The as-prepared materials are made into porous electrodes for coin cells assembly. Galvanostatic charge-discharge cycle tests, cyclic voltammetry (CV), and electrochemical impedance spectroscopy (EIS) are used as the electrochemical characterization methods. The intensive multidisciplinary research efforts across the fields of solid-chemistry, electrochemistry, computational chemistry, physics, material science and engineering, etc. are expected to help the development of advanced electrode materials for rechargeable lithium and sodium batteries diverging from the old empirical approach.

1.4 Contributions

This project is aiming at the synthesis of novel anode materials for lithium and sodium rechargeable batteries with facile synthesis approaches which have important technological potential. The electrospinning and microwave-assisted solvothermal reaction techniques are used as the main synthesis methods for anode materials preparation. Better understanding of lithium and sodium electrochemical cells is also an essential part of this project. Electrode materials are assessed with cell level analysis in terms of their impact on energy and power capabilities of batteries. For the research outcomes, electrospun PAN-derived carbon fiber sheets were adopted as a liquid sulfur cathode substrate for lithium-polysulfide cells which worked well in terms of reversible capacities and rate capabilities. The antimony-carbon fiber/graphene composite alloy type negative electrode materials and antimony sulfide graphene composite converse type negative electrode materials are both confirmed as high capacity (above 370 mAh/g), high rate (up to 1A/g charge/discharge rate) anode materials for lithium and sodium rechargeable cells, respectively. The different designs of composite materials are proved to be effective as they fulfilled most of requirements for high performance battery applications.

1.5 Thesis Outline

The thesis comprises of eight chapters in total. Chapter 1 (Introduction) provides general information on this PhD research project including a brief description of research strategy and research objectives. Chapter 2 gives a critical review of research and development of the lithium rechargeable battery and sodium rechargeable battery, especially the factors that currently limiting the performance of state-of-art lithium-ion batteries. Chapter 3 is the research methodology and experimental section, in which the material synthesis and characterization technique adopted for this project are explained. Chapter 4 to 7 presents the results and discussion regarding different electrode materials investigated within the scope of this research project. Chapter 8 is the concluding chapter, which includes the summary of this project and future recommendations.

Chapter 2 Literature Review

2.1 Brief history of lithium-ion battery development

“Battery” typically refers to a device that is composed of single or multiple electrochemical cells. The electrochemical cell consists of a positive electrode (electron acceptor), a negative electrode (electron donor) and an electrolyte (ionic and electronic conductor). In a conventional cell configuration, the two electrodes are solid and kept apart from each other by an electrolyte-permeable separator. In multiple-cell battery packs, those electrochemical cells are connected either in series or in parallel to fulfill the requirement of voltage and capacity. During operation, the charged electrochemical cells are connected externally and output energy at a certain voltage ($\boldsymbol{U}$) typically with a constant current ($\boldsymbol{I}$) for a variable time ($\Delta \boldsymbol{t}$), and the power output of a battery ($\boldsymbol{P}$) can be calculated with the equation 2-1. The amount of electrical energy stored in a battery ($\boldsymbol{Q}$) can be expressed per unit of weight (*Wh/kg*) or per unit of volume (*Wh/L*).

$$\boldsymbol{P} = \boldsymbol{U} \times \boldsymbol{I} \qquad 2\text{-}1$$

Lithium is the most attractive negative electrode for high energy density batteries because of its lightest equivalent weight (M = 6.94 g/mol) and the lowest electrochemical potential (-3.04 V versus standard hydrogen electrode) of all elements. Studies of lithium batteries began in the 1950s as the surface passivation mechanisms of lithium metal in a number of non-aqueous electrolytes were discovered, which made scientists realized that metallic lithium actually remains stable behind the solid-liquid interphase.[1] The stability of the lithium metal surface in those electrolytes was attributed to a passivation layer generated during the direct chemical reactions between lithium and electrolyte radicals. The passivation layer was found to be compatible with lithium transportation between electrolyte and lithium. The anode meanwhile prevents further reactions of electrolytes on the surface of lithium. This discovery soon helped facilitate the development of high energy density lithium battery systems. Within a very short period after its introduction to the consumer market, the primary (non-rechargeable) lithium battery systems with superior energy density supplanted other battery systems such as Nickel-cadmium (Ni-Cd), and Ni-metal hydride (Ni-MH) and seized the dominant place in portable electronics.

The development of lithium secondary (rechargeable) batteries lagged behind lithium primary batteries. The concept of using metallic lithium as the negative electrode in the primary batteries proved difficult to be implemented in secondary batteries. Preliminary investigations of cycling of lithium metal in organic electrolytes showed that the reaction is not entirely reversible due to the breakdown of the passivation layer on the surface lithium. With the bare lithium exposed to electrolyte during cyclic charge-discharge processes, further reaction continues, causing the repeated dissolution-deposition process of lithium. The deposition of lithium leads to lithium dendrite formation as a result of non-uniform current distribution, which can cause serious safety issues including short circuit and thermal runaway of lithium batteries.[2] The first attempt to resolve this issue was the design of high temperature molten salt systems with lithium-aluminum (Li-Al) alloy and iron sulfide (FeS) as anode and cathode, respectively. However, this system showed very limited cycle life due to large volume changes of the electrodes during operation which made large scale implementation difficult .[3] Other measures including modifications of separator and electrolytes in order to suppress the detrimental effect of dendritic lithium growth were also investigated.[4] The Exxon company later announced a room-temperature lithium secondary battery system (Li/TiS_2). The Li/TiS_2 battery was composed of electrochemical cells using lithium metal as negative electrode, lithium perchlorate ($LiClO_4$) in 1, 3-dioxolane (DOL) solution as liquid electrolyte, and TiS_2 as positive electrode. Both electrolyte and positive electrode were the best choices at the time because the good cycling efficiency of lithium and smooth lithium deposition morphology was found in DOL electrolyte, and TiS_2 has a very favorable layered-type structure which is stable framework for lithium intercalation reactions. Understanding the ion intercalation mechanisms was an offshoot from research works on the superconductivity of materials where scientists explored the physical properties of various compounds after intercalating ions or electron-donating molecules into host materials.[5] The lithium intercalation in the host lattice of layered TiS_2 was found to be highly reversible, and the structural change of TiS_2 upon lithium insertion and extraction was negligible since there no phase transition occurs. The whole intercalation process can be expressed in equation 2-2.

$$\boldsymbol{x}\mathrm{Li} + \mathrm{MS}_{\boldsymbol{y}} \frac{\leftarrow charge}{discharge\rightarrow} \mathrm{Li}_{\boldsymbol{x}}\mathrm{MS}_{\boldsymbol{y}}, (\mathrm{M} = \mathrm{Ti}, \mathrm{Mo}, \boldsymbol{y}{=}2) \tag{2-2}$$

$$\boldsymbol{x}\mathrm{Li} + \mathrm{MO}_{\boldsymbol{y}} \frac{\leftarrow charge}{discharge\rightarrow} \mathrm{Li}_{\boldsymbol{x}}\mathrm{MO}_{\boldsymbol{y}}, (\mathrm{M} = \mathrm{Co}, \mathrm{Mn}, \mathrm{Ni}, \boldsymbol{y}{=}2) \tag{2-3}$$

After Li/TiS_2, a variety of lithium secondary batteries with different combinations of intercalation electrodes and electrolytes based on similar battery chemistry were manufactured as coin cells (as shown in equation 2-3). Their applications were rather limited due to relatively short cycle lives upon deep discharge.[6] By the end of 1970s it was realized that most of the intercalation compounds remain single phase only for a relatively narrow range of $\boldsymbol{x}$ values (see equation 2-2) and they cannot be cycled with $\boldsymbol{x}$ crossing the phase transition points of the host materials. Taking Li_xMoS_2 for instance, this intercalation compound can insert lithium up to $\boldsymbol{x} = 3$ undergoing several stages of phase transitions, but this intercalation process is partially irreversible. The reversible lithium intercalation in Li_xMoS_2 is limited to the range of $\boldsymbol{x} \leq 0.8$.[7] The intercalation cathode materials are generally made in the charged state (without free lithium inside them) prior to the cell assembly because they are both oxygen and moisture sensitive in the discharged state. Therefore lithium metal is need as the counter electrode and the source of free lithium in the electrochemical cell. After discharge process, the lithiated intercalation cathode materials normally possess a potential ranging from below 3 V to about 4 V against Li/Li^+ redox couple.

The lithium secondary batteries with metallic lithium suffered from significant penalties in cycle life and safety due to lithium plating as well as occasional dendritic lithium. The plating of lithium occurs on the surface of metallic lithium anodes during the charge process and plated lithium can detach from the bulk lithium anode and become inert in subsequent discharge process. This leads to low cycling efficiency and constant capacity fading. In order to balance the loss of active material, excess of lithium at the anode side is required for this particular type of cell. The cycling efficiency ($\boldsymbol{E}$) of lithium batteries can be defined (as shown in equation 2-4) by the charge of lithium consumed ($\boldsymbol{Q_c}$), the amount of excess lithium ($\boldsymbol{Q_{ex}}$), and the cycle number ($\boldsymbol{n}$). The cycling efficiency can also be used to calculate the relative excess lithium ratio ($\boldsymbol{R}$) of lithium required for a given cycle number $\boldsymbol{n}$ (as shown in equation 2-5).[3]

$$\boldsymbol{E} = \frac{\boldsymbol{Q_c - Q_{ex} / n}}{\boldsymbol{Q_s}} \qquad 2\text{-}4$$

$$\boldsymbol{R = n} \times (\boldsymbol{1 - E}) \qquad 2\text{-}5$$

Low lithium cycling efficiency leads to a large $\boldsymbol{R}$ number which is unsuitable for practical applications of lithium secondary batteries. As aforementioned, these lithium anodes did show high cycling efficiency in $LiClO_4$/DOL electrolyte, however, no such product became available on the market to date. This is attributed to the unstable lithium perchlorate salt as well as highly explosive tendencies of DOL solvent, which makes this type of electrolyte risky to use in practical batteries.

The research efforts on lithium metal compatible electrolytes eventually lead to the important discovery of lithium permeable solid electrolyte interphases (SEI). SEI is a thin layer formed on the surface of lithium metal due to the synergetic effects from the decomposition of salt and solvent in certain electrolytes. The SEI is electronically insulating, which help protecting the lithium metal from further reactions with electrolyte. But it is also conductive for lithium ions, which help maintaining a stable electrode-electrolyte interphase for lithium ion exchange.[8] Supplementing the improvement of electrode and electrolyte materials, improvements in the design of lithium secondary batteries were also investigated. These measures included lowering the depth of discharge and limiting the charge current densities.[9] Non-aqueous organic electrolytes for lithium batteries generally have low conductivities for both electron and lithium ion transport, thereby limiting the capacity available at high rates of charge/discharge. Porous electrodes soaked with large amounts electrolyte can greatly impede the overall conductivity of lithium batteries. Therefore electrodes must be made very thin (100 ~ 300 μm thickness) so that the resistance against lithium ion transport within electrodes can be minimized.[10]

The obstacles for lithium metal anodes in lithium batteries triggered the design of lithium secondary batteries with both negative and positive electrodes made from intercalation compounds. Lithium intercalation cathodes showed excellent cycle performance in lithium half cells without detrimental effects such as consumption of electrodes or electrolytes. The replacement of lithium metal anodes with intercalation materials forms a so-called “rocking chair” or “swing” cell configuration (as shown in

Figure 2.1). This configuration allows completely reversible intercalations of lithium ions in tandem at both anode and cathode ends, hence supporting prolonged cycle life for lithium secondary batteries.[11,12]

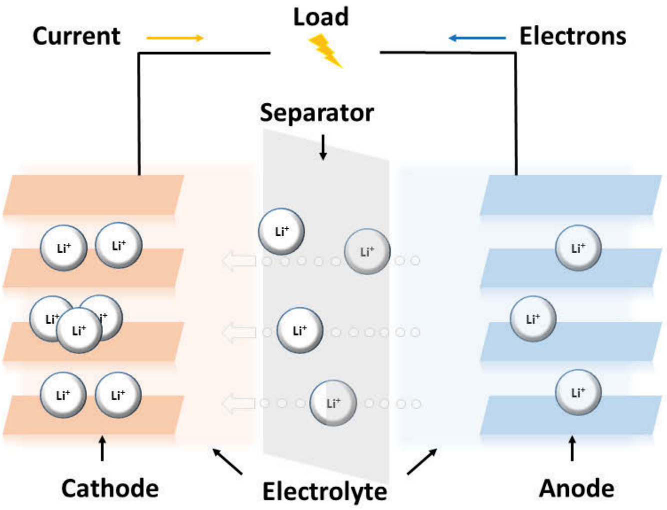

Figure 2.1 Schematic view of a "rocking chair" cell configuration based on the movement of lithium ions between two intercalation compounds.

In general, the intercalation compounds as anodes should have a much lower chemical potential versus lithium metal compared to the intercalation compounds used as cathode materials. Graphite, WO_2 and MoO_2 have all been investigated as negative electrode materials due to their high theoretical volumetric capacities.[13] Graphite can intercalate with lithium ions in a stoichiometry up to LiC_6 (as shown in equation 1-6) at an intercalation voltage close to that of lithium metal (~0.1 V versus Li^+/Li), which gives a high theoretical specific capacity of 372 mAh/g. These excellent features of graphite outperform two of the metal oxide type anode materials, making it the best candidate as an anode for intercalation type lithium secondary batteries. However, early attempts to integrate graphite anodes into lithium secondary batteries were unsuccessful. The absence of compatible organic electrolytes caused serious issues including electrolyte reduction on fresh graphite surfaces and co-intercalation of electrolyte species into graphite interlayers, which subsequently destroyed the graphite structure by exfoliation. These electrolyte-related problems were not resolved until the cycling performance improvement of graphite anodes in ethylene carbonate (EC) co-solvent electrolytes was discovered in the early 1990s.[14,15] The addition of EC in electrolyte initiated a passivation mechanism on the surface of graphite anodes, which is similar to the passivation mechanisms of surface layers formed on metallic lithium in non-aqueous electrolytes. Such a lithium ion conducting surface passivation film protected the graphite anode during initial lithium insertion processes. Although the formation of surface films on graphite is an irreversible reaction, it only occurs in the first cycle and the formation of new surface layers is inhibited during subsequent intercalation process.[16,17]

$$\boldsymbol{x}\mathrm{Li}^+ + \mathrm{C}_6 \, \frac{\leftarrow discharge}{charge \rightarrow} \, \mathrm{Li}_{\boldsymbol{x}}\mathrm{C}_6,\ (0 \leq \boldsymbol{x} \leq 1) \qquad 2\text{-}6$$

$$\mathrm{LiMO}_2 + \mathrm{C}_6 \, \frac{\leftarrow discharge}{charge \rightarrow} \, \mathrm{Li}_{1-\boldsymbol{x}}\mathrm{MO}_2 + \mathrm{Li}_{\boldsymbol{x}}\mathrm{C}_6,\ (\mathrm{M} = \mathrm{Co, Mn, Ni}) \qquad 2\text{-}7$$

In the “rocking chair” cell configuration, the graphite anode is made in a discharged state because graphite becomes highly active once intercalated with lithium and forms $\mathrm{Li}_x\mathrm{C}_6$ compound. Thus, graphite anodes need to be coupled with an air stable cathode made in a discharged state, which also acts as the source of lithium. The cycle of ‘rocking chair’ batteries always starts with a charging process, with the reduction (lithiation) of anodes and oxidation (delithiation) of cathodes proceeding in parallel (as shown in equation 2-7). Transition metal oxide type intercalation cathodes (e.g. $\mathrm{LiCoO_2}$, $\mathrm{LiMnO_2}$, and $\mathrm{LiNiO_2}$) all have a high oxidation reactivity in their charged states, high voltage beyond the thermodynamic stability window of electrolytes can cause highly exothermic reactions during battery operation. Therefore an electrolyte stable against both lithiated graphite anodes and de-lithiated cathodes at low and high potentials is indispensable.[15,18]

In the early 1990s, Sony announced its lithium-ion battery technology using the lithium cobalt oxide/hard carbon electrode couple based on the ‘rocking chair’ configuration. Soon the symbol ‘Li-ion’ became familiar to the public with the rapidly expanded market of consumer electronics e.g. cellular phones, camcorders, laptops and a wide range of personal entertainment devices. Compared with lithium secondary batteries containing metallic lithium anodes, lithium-ion batteries showed great improvement in terms of safety and cycle life. However, the useable energy of lithium-ion batteries are limited due to safety restrictions that originate from the cathode material. Delithiated $Li_{1-x}CoO_2$ cathode in commercial products is restricted to $\boldsymbol{x}$ values less than 0.5 (see equation 2-7) to avoid the release of oxygen from $LiCoO_2$ cathode, at which point the cell charging cut-off voltage is below 4.2 V versus Li/Li^+, and the intercalation reaction of $LiCoO_2$ gives a specific capacity ca. 140 mAh/g (only half of the theoretical value). The replacement of soft carbons by graphite in commercial lithium-ion batteries shows how higher specific capacity electrodes eventually give in to the requirements on total volumetric capacity and average voltage of the complete battery which determines the ultimate energy density of practical batteries. Soft carbon in a practical electrode typically offers a reversible specific capacity of ca. 550 mAh/g and a volumetric capacity of ca. 800 mAh/g, while hard carbon (graphite) in a practical electrode offers a reversible specific capacity of ca. 370 mAh/g and a volumetric capacity of ca. 750 mAh/L. However, the slightly lower average voltage of graphite compared with that of soft carbon versus Li/Li^+ results in a larger voltage difference between the anode and cathode, hence the higher energy density of lithium-ion batteries.

Further improvements in lithium-ion battery energy and power density are expected from the innovation of high voltage lithium intercalation chemistry with specially designed combinations of cathode, electrolyte and anode materials. The possible new cathode candidates are expected to have (i) a molecular mass comparable to $LiCoO_2$, (ii) the ability to exchange more than one electron per unit reversibly in its redox oxidation state, and (iii) a highly stable framework structure during intercalation reactions.[19] As for anodes, the goal of ongoing research efforts is to identify alternatives to carbon or graphite with both high capacities as well as more positive intercalation voltages versus Li/Li^+. An elevated intercalation voltage of anodes can avoid the detrimental effects of lithium plating during high rate charging processes, therefore improving the safety of lithium-ion batteries under abusive conditions.

2.2 Intercalation cathode materials

In intercalation-based lithium secondary batteries, cathode materials serve as a solid state host network which accommodates the extraction and insertion of charge carriers. The intercalation compounds of interests are mainly layered transition metal oxides, metal chalcogenides, olivine, and tavorite structure polyanion compounds. Among these intercalation cathode materials, lithiated transition metal oxide and polyanion compounds are more favorable for battery applications due to their high average operating voltages (3 - 5 V), high specific capacities (100 – 200 mAh/g) which result in high specific and volumetric energy capacities.

Layered structure $LiCoO_2$ has superior combined properties including high specific capacity and volumetric capacity, high operating voltage, good cycling performance[20] and low self-discharge rate and it is to date the most successful cathode material being applied in commercial lithium-ion batteries. The main drawbacks of $LiCoO_2$ cathode are the high cost of cobalt raw materials, its poor thermal stability and low tolerance for high rates and deep discharge. The Li and Co atoms are located in octahedral sites which occupy alternating layers and form a hexagonal symmetry in $LiCoO_2$ (as shown in Figure 2.2a). Above 200°C, the crystal structure of partially delithiated $LiCoO_2$ easily collapses accompanied by an exothermic reaction with oxygen release. This will ignite most organic electrolytes and cause thermal runaway of electrochemical cells.[21,22] Because of this poor thermal stability of $LiCoO_2$, advanced designs in electrochemical cells are required to ensure the safe operation of lithium-ion batteries using $LiCoO_2$ as cathode. Deep discharge of $LiCoO_2$ with more than 50% lithium of $LiCoO_2$ being extracted can induce lattice distortion from hexagonal symmetry and cause capacity deterioration. Metal element doping in $LiCoO_2$ has been studied and shows limited improvements in cycling performance in the case of deep discharge.[23–25] A common and effective approach to address this issue is via coating of various other metal oxides which constrain the structure change of $LiCoO_2$, by which the $LiCoO_2$ cathode can survive a deep state of discharge (releasing more energy via charge transfer) over a longer cycle life due to the enhanced structure stability.[26]

Layered $LiNiO_2$ shares the same crystal structure as $LiCoO_2$ (as shown in Figure 2.2a) and has a theoretical specific capacity very close to $LiCoO_2$. The $LiNiO_2$ cathode is supposed to be better a choice for lithium-ion batteries owing to the availability of raw materials compared to the $LiCoO_2$ cathode. However, the stoichiometric $LiNiO_2$ is metastable due to the tendency of Ni^{2+} ion to substitute Li^+ sites within the crystal frameworks during delithiation, which leaves the $Li_{1-x}Ni_{1+y}O_2$ as the major phase that serves the cathode role. Layered structure $Li_{1-x}Ni_{1+y}O_2$ has even lower thermal stability compared with $LiCoO_2$, causing obstacles for its implementation as a cathode material

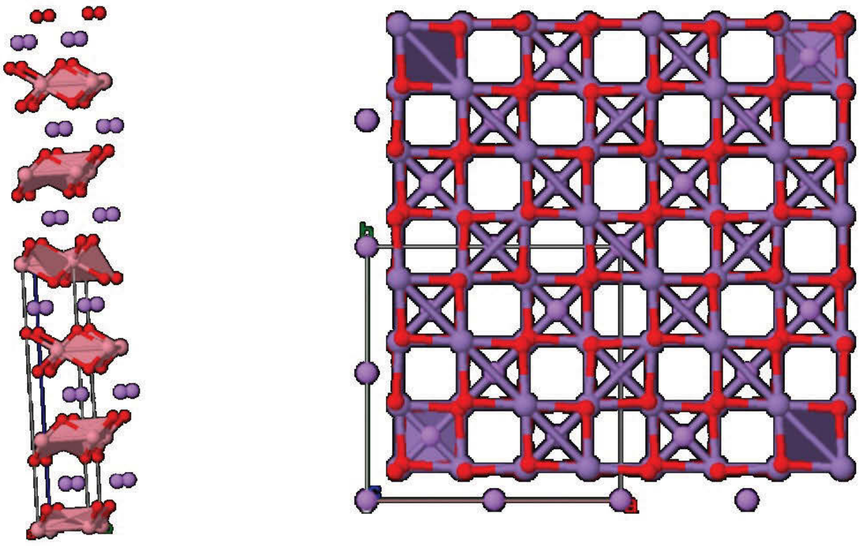

(a) Layered structure $LiCoO_2$

(b) Spinel structure $LiMn_2O_4$

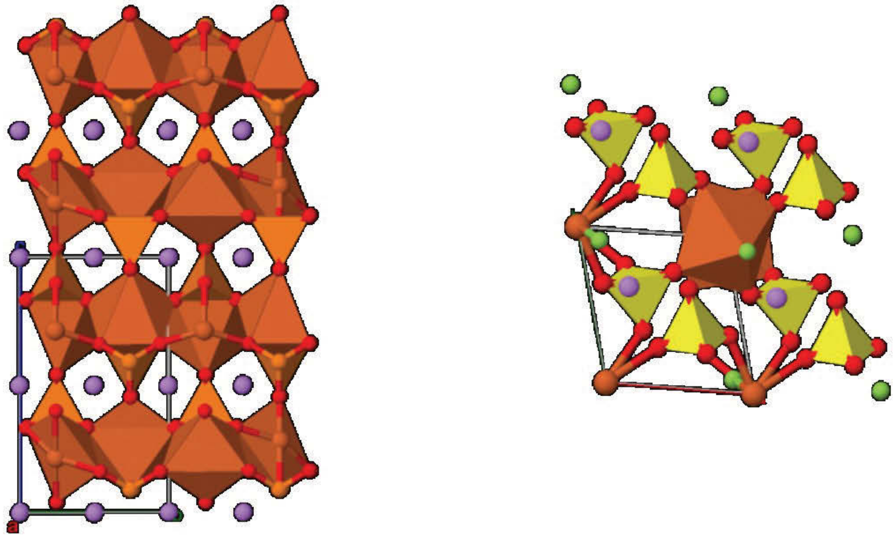

(c) Olivine structure $LiFePO_4$

(d) Tavorite structure $LiFeSO_4F$

Figure 2.2 Schematic illustration of high voltage lithium intercalation compounds with layered, spinel, olivine and tavorite crystal structures, in which the unassociated dots represent lithium ions.[27]

in commercial lithium-ion batteries.[28] Instead of $Li_{1-x}Ni_{1+y}O_2$, the $LiNi_{0.8}Co_{0.15}Al_{0.05}O_2$ (NCA) cathode[29] with higher attainable specific capacity (about 200 mAh/g) and longer calendar life has become the main form of lithiated nickel-based cathode in commercial lithium-ion batteries. In addition, the presence of both nickel and manganese in $LiNi_xMn_yCo_{1-x-y}O_2$ cathode is also found effective to enhance the structural stability of the host framework, which offers improved electrochemical performance including good rate capability, higher attainable specific capacity and an operating voltage close to that of $LiCoO_2$ cathode.[30,31] The common forms of $LiNi_xMn_yCo_{1-x-y}O_2$ cathode materials used in state-of-art commercial lithium-ion batteries include $LiNi_{0.33}Mn_{0.33}Co_{0.33}O_2$ (NMC 333), $LiNi_{0.5}Mn_{0.3}Co_{0.2}O_2$ (NMC 532), and $LiNi_{0.4}Mn_{0.4}Co_{0.2}O_2$ (NMC 442), etc. In general, a higher Ni ratio in NMC cathode results in higher attainable specific capacities, while lower Ni ratio results in better thermal stability of the cathode.[32]

Layered structure $LiMnO_2$ is another major cathode material for lithium-ion batteries. The main advantage of $LiMnO_2$ cathode is the low-cost, manganese-based raw material, which is more environmentally friendly when compared with $LiCoO_2$ or $LiNiO_2$. The application of $LiMnO_2$ cathode is hindered by its relatively poor stability upon lithium intercalation. The dissolution of manganese ions from the $LiMnO_2$ framework and accompanied valence change of Mn^{3+} ions during lithium extraction result in the crystal structure transforming from a layered structure to a spinel structure.[33] The strategy of metal element substitution is also an effective method to improve $LiMnO_2$ cathode. For instance, the $LiNi_{0.5}Mn_{0.5}O_2$ cathode offers both high energy density, low cost and acceptable cycling life. The addition of Ni can help realize high level lithium extraction without causing the structural deformation in $LiNi_{0.5}Mn_{0.5}O_2$ cathode. However, this material still suffers from low rate capability due to its relatively high resistance against lithium diffusion.[34]

Besides layered structure manganese cathodes, spinel $LiMn_2O_4$ is a cathode material which also benefits from low cost manganese raw material.[35] The lithium ion diffusion in this spinel host framework is realized through vacant tetrahedral and octahedral interstitial sites in the three-dimensional structure, in which lithium atoms occupy tetrahedral 8a sites and manganese atoms are located in octahedral 16d sites in a ccp array of oxygen anions (as shown in Figure 2.2b). The dissolution of manganese from manganese-based transition metal oxide cathodes is a common phenomenon that leads to cell performance deterioration.[36] In the case of spinel $LiMn_2O_4$ cathodes, undesirable side reactions also include release of oxygen from the $LiMn_2O_4$ framework and the high level decomposition of the electrolyte, which result in poor stability of $LiMn_2O_4$ cathode upon high charge/discharge rate operation or long-term cycling. The low rate capability of spinel $LiMn_2O_4$ cathode is due to the tendency of structural deformation from spinel to tetragonal $LiMn_2O_4$ under high rates, which greatly impeded its extent of application in lithium-ion batteries.

Polyanion compounds with $(XO_4)_3^-$ (X = P, S, Si, As, Mo, W) groups as the skeleton of a host framework generally offer high structural stability as well as high cathode redox potential therefore they are attractive cathode materials for lithium-ion batteries from safety aspects.[37] The phospho-olivine structure $LiFePO_4$, with lithium and iron atoms occupying octahedral sites and phosphorus atoms occupying tetrahedral sites within a slightly distorted hexagonal close-packed oxygen array (as shown in Figure 2.2c), is a very representative material among polyanion cathodes. The $LiFePO_4$ cathode has excellent thermal stability and rate capability (after downsizing to nanoscale and coating

Table 2.1 Electrochemical characteristics of the major intercalation cathode materials for lithium-ion batteries.[38]

Framework	Material Composition	Theoretical Specific Capacity (mAh/g)	Theoretical Volumetric Capacity (mAh/cm^3)	Average Voltage (V vs Li/Li$^+$)
Layered	$LiCoO_2$,	274	1363	3.8
	$LiNi_{0.33}Mn_{0.33}Co_{0.33}O_2$	280	1333	3.7
	$LiNi_{0.8}Co_{0.15}Al_{0.05}O_2$	279	1284	3.7
Spinel	$LiMn_2O_4$	148	596	4.1
	$LiCo_2O_4$	142	704	4.0
Olivine	$LiFePO_4$	170	589	3.4
	$LiMnPO_4$	171	567	3.8
Tavorite	$LiVPO_4F$	156	484	4.2
	$LiFePO_4F$	151	487	3.7

with conductive agent), which makes it a good candidate as a cathode material for high power lithium-ion batteries, but its low average voltage, low ionic conductivity and low electrical conductivity greatly hindered its electrochemical performance. Downsizing the $LiFePO_4$ particles to the nanoscale and chemical conductive coating are helpful to improve the overall conductivity of $LiFePO_4$ cathode but the resultant nanostructured $LiFePO_4$ electrodes often suffered from reduced volumetric capacities. Compared to olivine structure $LiFePO_4$, olivine structure $LiMnPO_4$ cathode can offer a higher specific energy in rechargeable cells due to its slightly higher average voltage (~0.4 V higher). However, the lower conductivity of $LiMnPO_4$ compared to that of $LiFePO_4$ inevitably neutralized the potential advantages in increased specific energy of $LiMnPO_4$ cathode due to other technical measures required (i.e. downsizing particle sizes to nano scale, conductive coating, etc.) for its implementation in lithium-ion batteries.[39] Other olivine structure cathode materials such as $Li_3V_2(PO_4)_3$, $LiCoPO_4$ and its solid solution derivatives (i.e. $LiNi_{0.5}Co_{0.5}PO_4$ and $LiMn_{0.33}Fe_{0.33}Co_{0.33}PO_4$) are also under development but their combined properties including power density, energy density, structure stability upon long-term lithium intercalation, and processing costs are not yet satisfactory for practical batteries applications.[40–43]

Tavorite structured $LiFeSO_4F$, composed of long chains with two slightly distorted $Fe^{2+}O_4F_2$ oxyfluoride octahedrons connected in the trans position by F vertices (as shown in Figure 2.2d), has a high average voltage, high electrical and ionic conductivity but a low specific capacity.[44] The $LiFeSO_4F$ cathode can offer reasonable specific energy in lithium-ion batteries with a relatively low manufacturing cost due to the natural abundance of its precursor materials. The results from *ab initio* calculation of tavorite structured compounds suggested that the intrinsic diffusion channels in materials such as $LiFeSO_4F$ with low activation energies allow fast charge and discharge rates comparable to olivine structured $LiFePO_4$ with smaller grain sizes.[45] $LiVSO_4F$ with a similar tavorite structure also has high capacity and good rate capability, but it is excluded from the candidate list of electrode material for lithium-ion batteries due to its low average voltage (ca. 1.8 V) and the possible low-level toxicity of vanadium.

2.3 Intercalation type negative materials

The intercalation type anode materials currently being adopted in commercial lithium-ion batteries can be divided into two major categories: (i) carbon anode and (ii) lithium titanium oxide. The intercalation type carbon anodes in commercial lithium-ion batteries include graphite and other hard carbons, both of them have certain degree of graphitic character which offers good electrical conductivity and ion conductivity, and its structure can be well maintained upon lithium intercalation due to low volume expansion and the stable SEI formation in organic electrolytes mixed with EC (as shown in Figure 2.3).

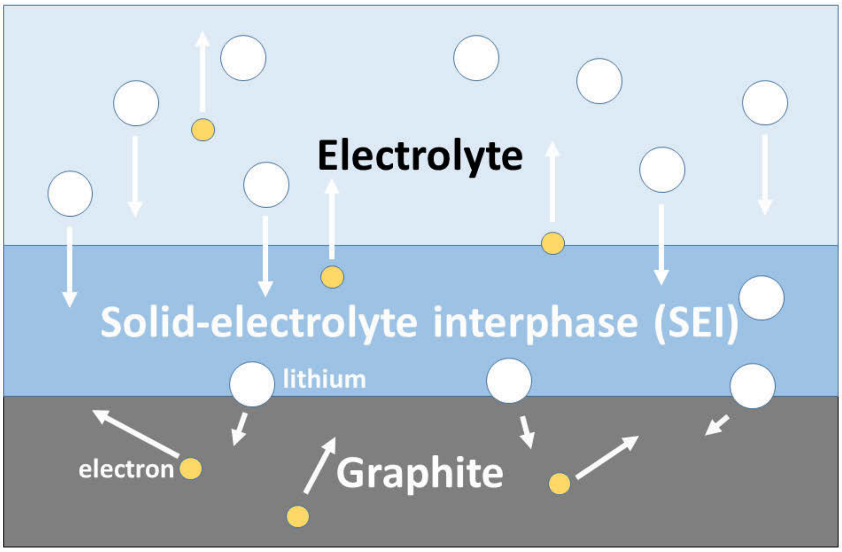

Figure 2.3 Schematic illustration of the solid-electrolyte interphase (SEI) on graphite anode in lithium-ion batteries.

Pure graphite anodes that have large graphite grains can attain a charge capacity close to the theoretical value, but the uniaxial volume expansion and contraction of graphite is a disadvantage for the long term cycling of lithium-ion batteries.[46,47] On the contrary, other hard carbon anodes with small graphitic grains in random orientation have a lower scale volume expansion rate due to the disordered structure which leads to isotropic strain upon lithiation. The structural defects also provide extra volume for lithium storage therefore the specific capacity of hard carbon anodes may surpass that of graphite.[48] For these hard carbon anode materials, high surface area and high fraction of exposed graphite edge planes are less favorable structural features for lithium-ion batteries applications because extra lithium ions will be consumed during the irreversible SEI formation in the initial cycle. This results in low first cycle coulombic efficiency, thereby decreasing the maximum achievable energy of the lithium-ion cells.[49] Well-engineered graphitic carbon anodes enabled the commercial lithium-ion battery technology two decades ago, and they are still playing an indispensable role in the state-of-art lithium-ion batteries due to their incomparable combined properties including natural abundance, low cost in raw materials, low average voltage, high volumetric and gravimetric charge capacity, as well as low irreversible capacity during the initial formation cycle of lithium-ion cells. The low initial irreversible capacity or (high first cycle coulombic efficiency) is an overwhelming advantage to these anode materials in a cell configuration with charge-balanced electrodes.

Spinel lithium titanium oxide ($Li_4Ti_5O_{12}$) is another intercalation type anode which has been utilized in lithium-ion batteries. $Li_4Ti_5O_{12}$ anodes operate at a high average voltage around 1.55 V, which is within the stability window of common electrolytes. The negligible volume change of $Li_4Ti_5O_{12}$ upon lithium intercalation and the superior thermal stability of $Li_4Ti_5O_{12}$ offers improved safety for lithium-ion batteries under high rate charge/discharge conditions. Theoretically, the electronic and ionic conductivity of $Li_4Ti_5O_{12}$ anodes can be promoted via nano downsizing. However, the formation of surface passivation layers has been confirmed with $Li_4Ti_5O_{12}$ anodes, although some researchers claim otherwise.[50,51] The SEI formation on the surface of $Li_4Ti_5O_{12}$ anodes is highly dependent on the electrode morphology. In addition, release of oxygen from the $Li_4Ti_5O_{12}$ framework can further accelerate the reactions between lithiated $Li_4Ti_5O_{12}$ and organic electrolytes at the electrode/electrolyte interphase as the temperature increases. Therefore SEI stabilizing agents are required for $Li_4Ti_5O_{12}$ anodes to suppress the interfacial reactions at high charge/discharge rates.

2.4 Alloy type negative electrode materials

Among those elements that electrochemically alloy with lithium, silicon and tin both have good combined properties including cost, environmental friendliness, and relatively low operating voltage and have attracted intensive research interests for alloy anodes in rechargeable lithium batteries. Compared with carbon-based anode materials in commercial lithium-ion batteries, anode materials with high loadings of silicon or tin inherently offer better safety in case of fire incident of lithium batteries owing to the much lower energy release from combustion products SiO_2 and SnO_2. Other metal elements such as silver, magnesium, and lead etc. also have been investigated due to their low voltage characteristics upon alloying with lithium, but eventually discarded from the list of potential alloy anode materials because of their relatively poor combined properties.

Silicon has a very small voltage plateau near 50 mV versus lithium upon lithiation, and it offers the highest theoretical specific capacity (3579 mAh/g) known so far, based on its lithium-rich lithiated analogue $Li_{15}Si_4$.[52] However, the $Li_{15}Si_4$ phase is metastable and has only been observed in electrochemical lithiation of Si near room temperature. Bulk Si undergoing a complete cycle of lithiation and delithiation essentially forms amorphous Si with structural feature completely different from its original phase.[53] The lithiation process initiates a huge amount of volume expansion of Si (up to 280%) and volume contraction follows in the subsequent delithiation process. Such a large scale volume change of Si leads to disruption of the electrode/electrolyte interphases, high internal stress within electrodes and, as a result, inevitable capacity fading of lithium cells. Therefore the design of nanosized Si incorporated with other inactive materials as a composite anode is usually adopted as a compromise in order to achieve a long and stable cycling performance for Si anodes. The downsizing of bulk Si to a scale of a few hundreds of nanometers has a great impact on electrode/electrolyte interphases, fracturing of lithiated Si grains as well as the packing density and stress levels in Si anodes upon lithiation. There have been a large number of reports on Si-C composite anode materials which utilize the conductive, low volume expansion properties of carbonaceous material and the high energy of silicon. Such designs usually encapsulate nanosized silicon in a complex carbonaceous microstructure, or nanosized silicon evenly dispersed through a highly conductive carbon matrix. Either way, the carbon acts as a conductive path for lithium diffusion and buffers the stress from volume expansion of lithiated silicon. For example, Si composite anodes with a combination of VGCF (vapor grown carbon fiber) and MWCNTs (multi-walled nanotubes) have shown excellent cycling results, in which VGCF accommodates the micrometer scale volume changes and the MWCNTs ensure an electrical conductive network between the VGCF and Si alloy.[54] However, synthesis of Si-C composite via a high temperature approach is not recommended because the thermal route will initiate the formation of SiC, which is normally an inactive compound towards lithiation and difficult to be detected by XRD due to its amorphous state.[55] The intrinsic disadvantages of Si-C composite designs include highly porous structure and low initial coulombic efficiency (ICE). The carbon microstructures in Si-C composites are designed to have high void spaces in order to accommodate the volume change of lithiated silicon, but this inevitably decreases the volumetric capacities of Si-C composite anode. The highly porous structure also leads to high surface area which is associated with large irreversible capacity, hence further decreasing the total energy available for a full cell using such alloy anodes. Only in rare cases have studies on Si-C anode included the details regarding volumetric capacity and relevant estimated energy of the full cell.[56] The low initial coulombic efficiency of Si/C anode is attributed to the amorphous nature of carbonaceous material as well as the high surface area of the Si/C composite. The low initial coulombic efficiency and low volumetric capacity of Si/C anode more or less negate the potential advantages of Si/C composite designs for practical lithium-ion batteries due to the limited total energy density at full cell level. There have been large numbers of publications on the topic of Si alloy anodes that claim stable cycling performance and high specific capacity of Si/C composite anode, but most of these research works are carried out using half-cell configurations without given detailed information regarding the volumetric density of the synthesized composite materials used, hence making these inspiring results on silicon alloy anodes not so outstanding from a practical point of view.

Tin is another active material for alloy anodes and has already been applied in a commercial lithium-ion battery product: the "Nexelion" cell with Sn-Co-C alloy anodes made by Sony since 2005. The Sn-Co-C anode in Nexelion cells contains alloy particles with about 1 μm size and the composition of their alloy is determined to be $Sn_{30}Co_{30}C_{40}$, which provide a reversible specific capacity around 400mAh/g.[57] This composite material contains nano Sn-Co grains which are evenly distributed throughout the carbon matrix, thereby preventing agglomeration of larger Sn regions during cell cycling. Except for Sn, Cobalt was the only transition metal that did not form carbides under equilibrium conditions, therefore Co became the sole choice as a secondary metal element in Sn-M-C composites that can maintain an amorphous-nanocrystalline active environment with Sn while accommodating volume expansion. The atomic ratio of Sn and Co is also found restricted to 1:1 in order to achieve maximum energy due to the formation of inactive and metastable phases.[58] In addition, the cycling test of Nexelion

14430 cell showed its capacity retention rate typically drops to 80% after around 220 cycles, with an average coulombic efficiency of 99.9% per cycle.[59]

In principle, the large volume expansion of alloy anodes triggers a series of detrimental effects on the long term cycling of lithium-ion cells as it is difficult to maintain good contact of active materials within electrodes and at electrode/electrolyte interphases, and prevent detachment of alloy particles during lithiation. In such cases, binders with stronger adhesion than conventional Polyvinylidene fluoride (PVDF) binder are often required. PVDF coatings normally forms thin polymer threads due to the low conductivity of PVDF molecules, which leaves the majority surface area of alloy particles exposed to electrolyte. The expansion of alloy particles during lithiation causes SEI growth also associated with electrolyte decomposition. Metastable phases of passivation layers on electrode surfaces can causes exposure of PVDF to electrolyte and severe swelling of this PVDF binder.[60] The accumulated decomposition products of electrolyte further isolate small portion of alloy particles and increase the electrode impedance. The poly(carboxylic acid) based water-soluble binders, i.e. carboxymethyl cellulose (CMC), have been recognized as excellent binders and alternatives to PVDF binder for alloy type anodes.[54,61–63] Although bulk poly(carboxylic acid) has brittle mechanical properties , its polymer chains are stretchable at a relatively small scales and easily withstand the large volume expansions of alloy particles during lithiation.[62] In addition, the hydrogen bonds formed between alloy surfaces and poly(carboxylic acid) are fairly weak and can be rebuilt spontaneously, therefore the correlation between improved cycling performance and increased carboxylic acid groups in poly(carboxylic acid) binders appear to be reasonable.[54,61]

The empirical evidence from the development of lithium secondary batteries imply that the cycling performance of certain types of electrode is highly dependent on the electrolyte components, including the type of salt, solvents, solution concentration, and additives, etc. This rule also applies to alloy anodes. Capacity loss can be reduced greatly when carefully chosen additives are present in the electrolyte in conjunction with proper binders. It is generally recognized that vinylene carbonate (VC) and fluoroethylene carbonate (FEC) additive in electrolytes can improve the cycling performance of Si anodes.[64,65] Conventional electrolyte for lithium-ion batteries are $LiPF_6$ solutions with various types of carbonate solvents. $LiPF_6$ salt can react with moisture content in electrolyte and generate HF as a hydrolysis product which react with exposed Si. This reaction may lead to surface cracking of Si alloys.[66,67] The addition of FEC in $LiPF_6$ electrolyte is believed to inhibit the decomposition of $LiPF_6$ salt and electrolyte solvents, resulting in a more stable SEI without continuous thickness growth during repeated lithiation/delithiation processes. The addition of FEC in $LiPF_6$ electrolyte is intended to help forming passivation layers that contains rich lithium alkyl carbonates, polycarbonate and polyenes but a small ratio of LiF on the alloy surface, hence preventing the electrolyte solvent from further decomposition.[68–70] In Sn alloy anodes, the situation is quite different. The passivation mechanism of Sn metal in organic electrolyte disappears at around 1.5 V, which means the electrolyte reduction remains constant whenever the electrolyte is in contact with exposed Sn, leaving the lithiation process unable to proceed.[71] Additives including VC and FEC in $LiPF_6$ electrolytes have been noted to generate beneficial effects for Sn alloy anode in terms of cycling performance.[72]

2.5 Conversion type negative electrode materials

Nanostructured binary transition metal compounds have been demonstrated that can react with lithium via a reversible conversion reaction route. The complete conversion reaction involves two stages (i) reduction of compounds and alloy reaction between lithium and metal/semi-metal elements, and (ii) formation of a Li_2O framework. Such conversion type anodes benefit from the high capacities which are mainly attributed to the formation of lithium alloy with metals, therefore potentially having a great impact on the specific energy of lithium cells.[73–76] As a result, the family of transition metal oxide compounds have attracted intensive research interests in the field of electrode materials for rechargeable lithium batteries.

Conversion type iron oxide electrodes with large specific capacity are among the representative conversion transition metal oxide compounds firstly being reported.[77,78] The initial work inspired many followed publications presenting various types of α-Fe_2O_3 and γ-Fe_2O_3 with sophisticated nanoarchitectures obtained from diversified synthesis routes, and with an average specific capacity above 900 mAh/g as well as good rate capability. [79–84] However, subsequent improvements of these electrodes producing more stable SEIs, high coulombic efficiency, and good capacity retention rates over a long term cycle life have been rather rare.

CoO and Co_3O_4 are among the most explored transition metal oxides for their application as negative electrode in lithium-ion batteries. Similar to iron oxide negative electrodes, the conversion reaction from Co_3O_4 to form metallic Co and Li_2O had already been observed in earlier studies,[85] but it was not until a high degree of reversibility for the conversion reaction was claimed in 2000 that intensive efforts to evaluate the performance of these phases were triggered.[75] Nanostructured CoO has been shown to efficiently reform after full charge-discharge cycles versus lithium with a high capacity above 600mAh/g, regardless of differences in microarchitectures and morphologies.[86–92] The higher theoretical specific capacity of Co_3O_4 has attracted much research interest for exploiting the full potential of this material. Advanced synthetic approaches include template-assisted crystal growth, pulsed-laser thin-film deposition, radio-frequency sputtering, high energy mechanical milling, spray pyrolysis, bio-assisted crystal growth and inverse microemulsions.[93–101] Despite the relatively high specific capacities as well as good capacity retention from several tens to a few hundreds of charge-discharge cycles being reported, the further improvement of Co_3O_4 anode specific capacity towards the theoretical limit has proved rather difficult. The challenge in developing practical Co_3O_4 negative electrode is owing to the nature of the conversion reaction between Co_3O_4 and lithium, which is not entirely reversible. The conversion reaction process is also highly dependent on the morphology features (e.g. crystalline size, specific surface area) of Co_3O_4 material and the rate of reactions (i.e. the charge/discharge current density). The electrochemical reactions between Co_3O_4 and lithium are proceed from the lithium insertion into the Co_3O_4 framework and formation of $Li_xCo_3O_4$, which decomposes and transforms into Li_2O and CoO upon further reduction.[93,96] The oxidation of nanostructured Co_3O_4 in anodes generally leads to oxidation of Co and formation of CoO, which is the main active phase for further reaction instead of Co_3O_4. [98,100,102] The partial irreversibility in the conversion process of Co_3O_4 anode is the primary reason for charge/discharge inefficiencies and it needs to be addressed before the wide application of Co_3O_4 anode materials in lithium secondary batteries.

Copper oxide was one of the early electrode materials exploited for lithium primary batteries.[103] Nanostructured CuO have also been investigated as conversion type anode materials for lithium secondary batteries,[104,105] where Cu_2O serves as the main intermediate phase throughout the charge and discharge process.[106] As a result, the cycling inefficiency observed in CuO anodes is similar to other conversion type transition metal oxide compounds, also affected by partially irreversible reactions.

Cr_2O_3 with a theoretical specific capacity up to 1058 mAh/g and a low average voltage at about 0.2 V is one of the most attractive anodes for lithium batteries. Like many other conversion type anode materials, the Cr_2O_3 anode can easily obtain a gravimetric capacity exceeding its long-term theoretical value during the first cycle lithiation due to full reduction to elemental chromium.[107,108] However, the coulombic efficiency of Cr_2O_3 anode is relatively low due to the irreversible conversion process of Cr_2O_3 (with only CrO phase being recovered after delithiation) as well as undesired electrolyte decomposition.[109,110] Hence, the cycling performance of Cr_2O_3 anodes in lithium batteries is generally inadequate especially when thin film deposition or mesoporous nanoarchitecture designs are applied at the expense of reduced volumetric capacity. In addition, the carcinogenic nature of Cr_2O_3 also limits its industrial applications.

MnO_2 is another candidate for high capacity anodes in lithium batteries.[111,112] The complete conversion of MnO_2 can deliver a theoretical specific capacity of 1233 mAh/g at an average voltage of ~0.4 V versus lithium, but the high oxidizing tendency of manganese poses technical challenges for achieve such high capacity with full reduction of manganese to its metallic state.[113] Manganese oxides including MnO have been studied and showed much smaller specific capacities in lithium half-cells compared to their theoretical values.[114,115] In addition, rather low initial coulombic efficiencies in the first cycle and drastic capacity decays with increasing cycle numbers were also observed with manganese oxide anodes. The further exploration into the reaction mechanism of manganese oxides as negative electrodes have also led to conflicting conclusions from difference research groups.[116]

Other transition metal oxide such as NiO,[117,118] MoO_2,[119–121] MoO_3,[122–124] and RuO_2[125] have also been investigated as anode materials for lithium batteries, but these high capacity anode materials all presented limited cycle lives suggesting they are inadequate to serve as anode materials in lithium secondary batteries through conversion reactions. Some transition metal sulfide compounds can also react with lithium through the electrochemical conversion mechanism and may potentially serve as high capacity negative electrodes for lithium batteries.[126–130] However, the reduction of transition metal sulfides leads to the formation of polysulfide species in organic electrolytes. As a result, the conversion type transition metal sulfides also experience capacity fading owing to the cumulative formation of lithium sulfide layers on electrode surfaces.[131]

Except for transition metal chalcogenide compounds, transition metal phosphide, transition metal nitride, and transition metal fluoride compounds have all been investigated as conversion type negative electrode materials for lithium-ion batteries. These materials also show high specific capacity for lithium storage via partially reversible conversion reactions, and progressive capacity fading over several charge-discharge cycles has been observed as well.[132] Despite the very appealing capacities shown by different conversion type compounds as mentioned above, their applications in practical lithium batteries have still been impeded by their relatively high average voltages, low cycling efficiencies and fast capacity decay. The shortcomings of conversion type negative electrodes originate from their fundamental reaction mechanisms, leaving many difficult challenges from the materials design perspective.

2.6 Key indices of electrode materials for lithium-ion batteries

The state-of-art lithium-ion battery technology is reaching its limit in terms of energy density due to the intrinsic limitations of electrode materials. In commercial lithium-ion batteries, graphite which usually serves as anode material shows excellent performance including low cost, low voltage hysteresis, low volume expansion upon lithiation, low irreversible capacity, good thermal stability, good rate capability, good densification during electrode fabrication, as well as the resultant high gravimetric and volumetric charge capacity. The combination of all these good properties of graphite makes the searching for alternative negative electrode materials a very challenging mission. Researchers have been focusing on two particular types of materials, e.g. anode materials based on alloy reactions and conversion reactions. Both have the potential to deliver a much higher specific capacity compared with graphite. However, the difficulties in discovery of new anode materials are usually underestimated due to the complexity of evaluation regarding these negative electrode materials. For instance, the majority of literature on novel electrode materials usually consists of a set of electrochemical and material characterization means which are not related to the improvement of lithium secondary cells in terms of volumetric energy and cycle stability. The most frequently reported improvement in negative electrode material studies focus on higher specific capacities compared to that of graphite, regardless of the densification properties, irreversible capacities, voltage hysteresis, stability of electrode/electrolyte interphases, depletion of electrolyte, etc. Other key factors that determine whether an anode material is suitable for commercial lithium rechargeable battery applications include volumetric capacity, and capacity retention rate upon long term cycling in a full-cell configuration. Unfortunately, in the evaluation of potential anode materials for lithium-ion batteries these factors are usually not mentioned. Based on conclusions on materials specific capacities alone is insufficient because it is not the main factor that dictates the practical, long-term energy density of lithium-ion batteries. The estimation of energy density of any lithium cell is based on both negative and positive electrodes. More importantly, the positive electrodes that contain active lithium materials serve as the donor of lithium ions, therefore the cathode dictates the amount of free lithium and subsequently the overall energy density of the cell. The high average voltages (between lithiation and delithiation) versus Li/Li^+ and capacities of cathode materials obtained in half-cells cycling tests can be used to estimate the energy densities of lithium full-cells if they have negligible volume change during the lithium intercalation reactions. The estimation of cathode energy can provide a rough idea on how much of an intercalation type cathode can affect the overall energy density of lithium cells by mathematical modelling. However, such an approach is not applicable in the case of anode materials due to the absence of corresponding cathode voltages and capacity in lithium half-cells. As a result, most literatures have used the term ‘specific capacity’ (mAh/g) as the major index for anode materials of interest. For practical battery applications, the commonly accepted index for battery energy density is calculated based on volume (Wh/L) instead of weight (Wh/kg), because the volume reserved for electrode materials in most cell designs is fixed. Therefore, the use of volumetric energy to evaluate a full cell makes more sense than the presentation of the lithium storage capabilities in half-cell tests. In addition, the porous nature of many reported anode materials with absence of their data on volumetric densities make the estimation of their impact on the energy density of a complete lithium full cell impossible, hence the claim of improvement with novel anode materials in terms of high specific capacity may be meaningless.[133]

The critical factors for the evaluation of alloy type anodes on the energy density of lithium-ion batteries include volumetric capacity, average voltage, and the volume expansion rate of active materials in the anode. The volume expansion of alloy based anodes upon lithiation are well-known to be greater than that of graphite. Thus, negative electrodes are typically made with high porosity, leaving enough free space to accommodate the volume change of the alloy. The high porosity anode has high surface area and results in a high irreversible capacity loss as well as decreased coulombic efficiency when compared with graphite anodes.[134] The irreversible capacity loss and decreased coulombic efficiency have been associated with the fracture and the disconnection of active material particles and electrolyte decomposition during the growth of electrode/electrolyte interphase. As shown in Figure 2.4, even a slight drop in coulombic efficiency (*e.g.* 0.3%) can result in drastic capacity loss of rechargeable cells over a prolonged cycle life.[135]

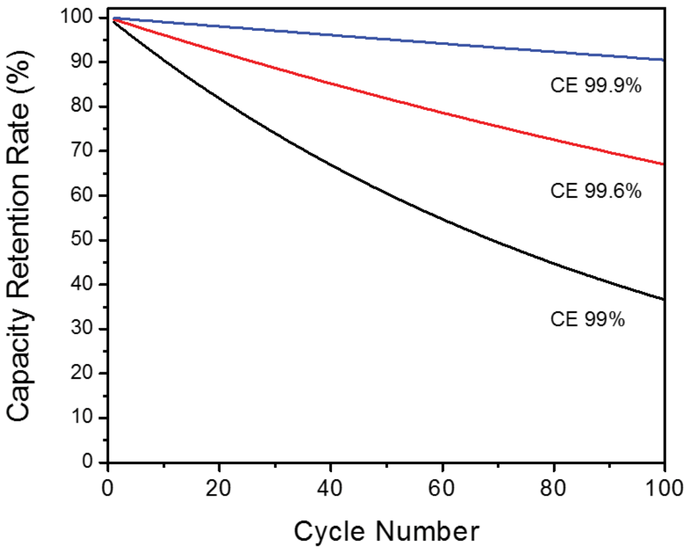

Figure 2.4. Capacity retention rates with coulombic efficiencies of 99%, 99.6%, and 99.9% after 100 cycles of charge-discharge.

In order to evaluate the energy storage capability of anode materials that experience considerable volume change during cycling, their volumetric capacities should be calculated based on the fully lithiated state (maximum volume) instead of prior to lithiation, especially for alloy type electrode materials which always show large volume change during lithiation/de-lithiation processes.[55] Since the practical energy density of a full cell is proportional to the cell voltage divided by the cell stack volume, considering the relatively small quantity of active material contained in anode, its volume has much less impact than its voltage on the overall energy density of a full cell. Therefore the energy of a full cell is more highly dependent on the anode voltage than the basic anode material's capacity. As a result, anode materials with low operating voltages versus Li/Li^+ are more favorable for battery applications compared with those that have high average voltage levels.

For conversion anode materials, i.e. nanostructured transition metal oxide, sulfide, phosphides, and fluorides, their reactions with lithium ions always undergo a complete change in both composition and structure, causing voltage hysteresis between charge and discharge processes. The voltage hysteresis between charge and discharge process causes considerable energy loss for lithium cells over many cycles of operation. The low potentials where conversion reactions take place are usually outside the range for reduction reactions of most electrolyte species used for lithium-ion batteries hence leaving obstacles for the formation of a stable electrode-electrolyte interphase on an anode surface.[136] The absence of stable passivation layer on the anode will inevitably cause side reactions that consume electrolyte as well as free lithium. Therefore, obtaining long term charge-discharge cycles with conversion type anode materials in lithium cells has proved impractical. Nanostructured materials for electrodes are generally obtained from complex synthesis routes, with extremely large surface areas and low volumetric densities, hence making the majority of conversion anode materials less attractive for battery applications due to their high material processing cost, low cycle efficiencies, and low volumetric capacities.

2.7 Electrolytes for lithium-ion batteries

Electrolytes play a fundamental role in terms of current (power) density, time stability, and safety of batteries. Electrolytes that connect both electrodes are essential components for batteries and the composition of electrolyte has a great influence over the battery performance via the interfacial chemistry. Consistent research efforts over the last few years have provided fundamental understanding of the electrode/electrolyte interphase formation mechanisms as well as the kinetics of lithium ion transportation in bulk electrolytes. Besides ionic conductivity, a good electrochemical stability and compatibility with the electrodes is also desirable for electrolyte optimization. Electrochemical stability is evaluated by considering the electrode/electrolyte interfacial resistance, the voltage window and the electrolyte behavior during battery cycling. Therefore, the design of liquid electrolytes for lithium-ion batteries in practice is usually a compromise with co-solvent systems to achieve the balance of many constraints (e.g. electronic and ionic conductivity, dielectric permittivity, viscosity, and interfacial stability against anode and cathode, materials). Juggling all these variables via ‘trial and error’ can be a laborious approach for finding an optimized electrolyte formula.[137]

The ionic transport properties that determine the mobility of ions inside a media are generally considered as the most important properties of the electrolyte. As the rate of electrochemical reactions in any given system is highly depending on the mobility of ions, the ionic conductivity of electrolyte is one of the main factors that limits the energy as well as the power capability of lithium-ion batteries. The ionic conductivity ($\boldsymbol{\sigma}$) can be expressed as a function of the free ion number $\boldsymbol{n}$, the ionic mobility $\boldsymbol{\mu}$, the valence order of ionic species $\boldsymbol{Z}$, and the unit charge of electrons $\boldsymbol{e}$ (as shown in equation 2-8).[138]

$$\sigma = \sum n\mu Ze \tag{2-8}$$

The typical nonaqueous electrolyte used in most lithium-ion batteries today comprises lithium hexafluorophosphate ($LiPF_6$) salt, mixed carbonate and ester solvents. Such a complex electrolyte system result in a modest ionic conductivity about 10 mS/cm at room temperature. Aqueous electrolyte systems offers advantages in high ionic conductivity and lower manufacturing cost of batteries, but they are still excluded from rechargeable lithium batteries because of their narrow stable voltage windows greatly limiting the energy storage capability of lithium batteries. Only a few lithium salts other than $LiPF_6$ are qualified as electrolyte solutes for lithium-ion batteries, namely lithium perchlorate ($LiClO_4$), lithium hexafluoroarsenate ($LiAsF_6$), lithium tetrafluoroborate ($LiBF_6$), and Lithium triflate (LiTf).[139] These salts all have good solvation capabilities in common electrolyte solvents while their dissociated ions are electrochemically inert to other components within the cell. Nevertheless, the position of $LiPF_6$ as the electrolyte solute for industrial applications remains unchallenged because of its well-balanced properties. Similar to the situation of lithium salts, the number of qualified solvents in the pool of nonaqueous polar solvents is also limited for lithium-ion battery electrolytes. The restrictions for electrolyte solvents are set by the (i) operating voltages of both negative and positive electrodes and (ii) the ability to dissociate the lithium salt.[140] Ethylene carbonate (EC) with high dielectric permittivity is an indispensable solvent in almost all electrolytes for lithium-ion batteries due to its unique effect on the

SEI formation at graphitic anode surfaces. Low viscosity solvents such as acyclic carbonate and carboxylic esters including dimethyl carbonate (DMC), diethyl carbonate (DEC), and ethyl methyl carbonate (EMC) are also commonly used electrolyte solvents due to their ability to help reduce the electrolyte overall viscosity. The use of mixed solvents undoubtedly causes difficulties in finding electrolytes with optimized (not maximum) ion conductivities because a large number of electrolyte formulas have to be experimentally examined in lithium cells with multiple interacting variables (i.e. lithium salt type, concentration, solvent type, charge/discharge current density and the operation temperature) before an optimal electrolyte formula for cell operation can be decided. [141]

Compared with modification of electrolytes by introducing new solute or solvents, the electrolyte additive approach is more economical and attractive for industrial applications. Additives in lithium-ion battery electrolyte are usually selected due to their higher reactivity to interphase redox processes compared with bulk electrolyte components. A small amount of additives (e.g. vinylene carbonate, fluoroethylene carbonate) in electrolytes can react first on electrode surfaces during the initial cycle of batteries, thus serving as the sacrificial media that help to maintain the electrode/electrolyte interphases for the subsequent charge-discharge cycles. Nevertheless, the use of additives has limited effects on the overall performance of lithium-ion batteries because the additive concentration in electrolyte is rather small and the utilization of electrolyte additives are mainly only focused on the improvement of electrode/electrolyte interphase properties.[142–145]

2.8 Lithium secondary batteries beyond intercalation chemistry

Lithium-ion batteries offer the highest energy density among all know battery systems and have seized the dominant market position in portable electronic devices for over two decades. But the power and energy from large size lithium-ion battery packs based on graphite/NMC electrode couples are far too low compared with what a typical 4-cylinder petrol engine can offer. Most electric vehicles available to consumers today offer a competitive price at the expense of driving ranges and power, while the high end electric vehicles, *e.g.* Tesla model S, with a driving range equivalent to conventional vehicles are only available to a niche market due to their high costs in manufacturing and marketing. As a result, the market penetration of electric vehicles in the transport sector is still very small at the moment. The fundamental chemistry of lithium-ion batteries poses inherent limits on their energy storage capability, and this situation is unlikely to change unless new battery chemistries emerge. Lithium-sulfur and lithium-oxygen are two major categories of post lithium-ion battery chemistries that have attract massive research interest owing to the high theoretical energy density of Li/S and Li/O_2 redox couples. The successful development of rechargeable lithium-sulfur batteries or rechargeable lithium-oxygen batteries are expected to greatly extend the driving range of fully electric vehicles.

Rechargeable lithium-sulfur (Li-S) batteries are a conversion-based energy storage system which utilizes the reaction between lithium and sulfur. The main advancement in the conceptual design of Li-S batteries is the substitution of cobalt containing cathode materials with low cost and naturally-abundant sulfur, which may bring significant reduction in battery cost compared with lithium-ion batteries. A typical Li-S battery system consist of a lithium metal anode, a sulfur containing cathode, and a non-aqueous electrolyte. The complete reaction can give a theoretical gravimetric energy density of 2500 Wh/kg or a volumetric energy density of 2800 Wh/L based on an optimistic model as shown in equation 2-9, in which the sulfur molecules are completely reduced to lithium sulfide (Li_2S) at the cathode end, where each sulfur atom accepts 2 electrons and generates a specific capacity of 1675 mAh/g, and the whole process is completely reversible.[146]

$$2Li^+ + S \xrightarrow[charge\rightarrow]{\leftarrow discharge} Li_2S \qquad 2\text{-}9$$

The concept of Li-S batteries was proposed in the 1960s when lithium secondary batteries along with other electrochemical battery systems were all in their early stage of development.[147] In general, the discharge process of Li-S batteries can be divided into three major stages (i) the reduction of insoluble sulfur and formation of high order (long chain length) polysulfides (Li_2S_n, $6 \leq n \leq 8$), (ii) reduction of high order polysulfides and formation of low order (short chain length) polysulfides (Li_2S_n, $3 \leq n \leq 5$), and (iii) reduction of low order polysulfides and formation of insoluble solid lithium sulfides (Li_2S_2, Li_2S).[148] The soluble polysulfide species can diffuse through the electrolyte and separator during the battery operation, and eventually form a deposit of Li_2S_2 and Li_2S on the surface of the lithium anode. The irreversible deposition of Li_2S leaves insulating layers, which cause continuous losses of active materials upon repeated charge/discharge processes. Meanwhile, the conversion from sulfur to soluble polysulfides and then to insoluble polysulfides also leads to the structural instability of sulfur cathodes due to the large volume expansion of sulfur upon lithiation. Most of the intermediate polysulfide species (Li_2S_n, $3 \leq n \leq 8$) are soluble in commonly employed Li-S electrolyte which contains 1, 3-dioxolane and glycol ethers (i.e. dimethoxyethane, tetraethylene glycol dimethyl ether) mixed solvents, and can migrate between anode and cathode under the effect of concentration gradient. The dissolution of polysulfide species causes rapid capacity fading of Li-S batteries in the first few charge/discharge cycles. The free migration of high order polysulfides to anodes, reduction of high order polysulfides to low order polysulfides at the anode, migration of low order polysulfides to the cathode and reformation of high order polysulfides, forms the unique shuttle mechanism of Li-S batteries. The shuttle mechanism of polysulfide species is helpful for the overcharge protection of cells, but it also consumes more energy during the charging stage. The self-discharge behavior associated with the polysulfide-shuttle is also the main reason that causes low coulombic efficiency of Li-S batteries. Li-S batteries with room temperature ionic liquids as electrolyte can achieve higher coulombic efficiency and good capacity retention rate compared with Li-S batteries using conventional liquid electrolytes.[149,150] In general, the ionic liquid is able to suppress the dissolution of sulfur thereby enhancing the cycle performance of the sulfur cathode, but the high synthesis cost of ionic liquids means this is not a practical approach for industrial applications.[137] The dissolution and migration of polysulfide species is inevitable due to the high donor ability of ether-based solvent and the concentration gradient in electrolyte of Li-S batteries. As a result, charged Li-S cells will lose stored energy in a continuous manner, along with a drop of open-circuit potential upon storage. As a result, the state-of-art Li-S batteries still have a series of issues including low coulombic efficiency, short cycle life, high self-discharge rate, and safety hazards. These issues originate from the fundamental chemistry of Li/S redox couple and pose the major obstacles to making this particular type of battery system ready for industrial production.

The majority of studies on Li-S batteries were aiming at the goal of optimized design of composite sulfur cathodes, through which polysulfide mitigation can be suppressed, thereby enhancing the overall performance of Li-S batteries. A great number of porous sulfur cathodes have been synthesized via the above mentioned strategy, with host structures including conductive carbonaceous materials,[151–164] conductive polymers,[165–170] and even electrochemically insulating architectures with high micro-porosity such as silica and titanium dioxide[171–175]. The common form of cyclic octasulfur (S_8) exhibits a unique temperature-viscosity behavior in its molten state, achieving a minimum viscosity near the temperature 155°C within the range from 115°C to 190°C.[176] This unique feature of sulfur has led to a convenient synthesis strategy for sulfur composite cathode materials, in which molten sulfur flows into porous host structures due to the capillary effect. The charge/discharge cycling tests reported in the literature have showed promising results as the stable cycling of composite sulfur cathodes and high specific capacity of sulfur both have been demonstrated, which is a significant improvement over bare sulfur cathodes. This strategy is unable to resolve all the problems associated with sulfur dissolution and migration of soluble polysulfide species within current Li-S cell configurations.

In order to utilize the advantage of the high energy density of sulfur, a composite cathode must provide enough electronic conductivity as well as void spaces to buffer the volume expansion of sulfur during lithiation. However, the achievable energy and power from Li-S cells is not so attractive for practical battery applications due to the low gravimetric density of sulfur ($2.07 g/cm^3$) and poor conductivity (1×10^{-15} S/m). In order to realize the target of an electrode areal capacity equivalent to that of the state-of-the-art lithium-ion battery, high areal sulfur-loading levels on the cathode are required for Li-S cells. On the other hand, the high weight ratio of sulfur in cathodes often results in a low sulfur utilization rate and low power (current) capability. On the other hand, sulfur is slightly soluble in commonly used electrolyte solvents for lithium-ion batteries, but polysulfide anions can form readily in these electrolyte solvents. This feature of polysulfide species has led to the strategy of adopting semi-liquid sulfur cathodes with a high electrolyte/electrode volume ratio for improved performance of Li-S batteries.[177,178]

Compared with massive volume of literature on novel cathode materials for lithium-sulfur batteries, the research on the evolution of polysulfides during the reactions between sulfur and lithium is rather rare. This is partially attributed to the difficulties in in situ characterization techniques which continuously monitoring the reduction and oxidation process of polysulfides. The Gibbs free energies (ΔG^0) of soluble polysulfide anions are very close to each other, and intermediate polysulfide species co-existent in the electrolyte through a series of chemical equilibria.[179,180] In addition to phase instability, the air-sensitivity of polysulfides also poses technique challenges for acquiring relevant knowledge towards a full understanding of lithium-sulfur reaction kinetics.

As a member of the metal-air battery family, research on primary Li-Air batteries already started in the middle of 1990s.[181,182] The emergence of rechargeable lithium-oxygen battery research was triggered by the discovery of rechargeable behavior of metallic lithium in pure oxygen environment. This revealed the possibility of developing energy storage systems based on lithium-oxygen reactions with superior energy density more or less equivalent to internal combustion engine (ICE).[183,184] Similar to Li-S batteries, the high expectation of the energy density of Li-O_2 batteries is overly optimistic because the early estimations on the specific energy of Li-O_2 systems were solely based on lithium metal anode with the weight of other cell components being excluded, hence the calculation lead to a breathtaking theoretical specific energy up to 10 kWh/kg. Nevertheless, intensive research efforts have been devoted into this field trying to achieve better understanding of the reaction kinetics behind the rechargeable behavior of Li-O_2 systems. In general, there are two types of lithium-oxygen secondary batteries, one is a nonaqueous system using aprotic electrolytes and another is an aqueous system using water-containing electrolytes. The reversible reactions in nonaqueous and aqueous rechargeable Li-O_2 batteries can be described in simple forms as shown in equation 2-10 and 2-11, respectively. The main research interests are focusing on the nonaqueous Li-O_2 secondary batteries because they offer higher theoretical energy density over the aqueous ones.

$$2Li^+ + O_2 \xrightarrow[charge\rightarrow]{\leftarrow discharge} Li_2O_2, \qquad 2\text{-}10$$

$$4Li^+ + 6H_2O + O_2 \xrightarrow[charge\rightarrow]{\leftarrow discharge} 4(LiOH\cdot H_2O), \qquad 2\text{-}11$$

However, system level analysis of rechargeable Li-O_2 batteries have led to the rather pessimistic conclusion that it is difficult for any practical Li-O_2 battery configuration (which still has not been attained) to achieve a gravimetric or volumetric energy density equal to state-of-art commercial Li-ion batteries.[185] The large gap between the theoretical energy density and the estimated attainable energy density in practical applications is mainly attributed to the technological limitations on oxygen storage. Large reservoirs for ultra-high purity oxygen are indispensable for Li-O_2 battery systems regardless of the cell configuration. In addition to the significantly lower energy density compared to advanced lithium-ion batteries, the slow charge/discharge kinetics of the Li-O_2 couple also poses limits on the power capability of potential Li-O_2 battery systems because recharging is only possible at very small currents.

The operation of Li-O_2 batteries involves complex products compatible with lithium, oxygen and electrolytes which must maintain the reversibility of Li-O_2 redox reactions.

Various electrolyte components including carbonates,[186–190] ethers,[191–194] DMSO,[195–197] and ionic liquids[198–200] as well as polymer membranes[201–205] investigated in Li-O_2 batteries have all lead to inadequate performance. Unfortunately, up to date stable electrodes and electrolyte components for Li-O_2 batteries with full recovery of O_2 over a complete charge/discharge cycle have not yet been confirmed. In general, the reproducibility of Li-O_2 batteries charge/discharge capacities and cycle-life is rather difficult compared with that of lithium-ion batteries. This status of Li-O_2 battery research is partially attributed to the high sensitivity of reactions in Li/O_2 system toward electrolyte impurities.[206] While most research efforts are focusing on the rechargeability of Li-O_2 batteries, little attention has been given to the safety issues relating to the operation of Li-O_2 systems, which is an important factor setting the energy density for practical applications. The recharge behavior of Li-O_2 batteries is highly dependent on the metastable lithium superoxide and lithium peroxide compounds together with organic solvents that have an inflammable nature and explosive tendencies.[137] Compared with small scale laboratory test devices, the combination of these chemically active species with a highly energetic lithium anode poses much more serious threats to the safe operation of large scale Li-O_2 battery systems.

2.9 Revival of research interest in room-temperature rechargeable sodium batteries

Early research on rechargeable batteries with sodium as the negative electrode originated in the 1980s, which is similar to the history of lithium batteries.[207–209] In general, the research and development of sodium-ion batteries shares the same knowledge base with lithium-ion batteries. Sodium is a less attractive anode candidate for batteries due to its higher equivalent weight (M = 22.99g/mol) and less negative electrochemical potential (-2.71 V versus standard hydrogen electrode) compared with lithium. But the natural abundance of sodium on earth, hence the cost reduction in raw materials is a key factor for consideration regarding the potential application of sodium batteries in large scale energy storage systems. Unlike lithium batteries, the development of sodium secondary batteries is mainly focused on the high temperature energy storage systems such as sodium-sulfur batteries and Na-$NiCl_2$ batteries (also known as ZEBRA batteries) in which sodium is kept in liquid form (above 98°C).[210,211] The specifications of these sodium batteries determined their limited applications in a few niche markets such as aerospace. After the successes of lithium primary batteries and subsequent lithium secondary batteries were embraced by the public, research interests were even more focused on lithium-ion batteries, leaving sodium batteries given less attention in the past. [212]

There is general agreement across scientific, economic and political communities that the transportation sector in the future will involve intensive use of electric motors in order to improve the round-trip efficiency of energy consumption as well as control the level of air pollutants from vehicles.[213] Other non-lithium energy storage technologies under developed such as fuel cells still require major technology breakthrough before they can compete with lithium-ion batteries in terms of energy density, production cost, lifespan, and operation cost besides the system-level round-trip efficiency.[214] The lead-acid batteries installed in most vehicles today can only support limited functions such as engine ignition or lighting, and they are not suitable to serve as the main power source for electric vehicles due to their limited energy densities. Lithium-ion battery technology is relatively mature and the production of large battery packs specifically for automotive purpose have been established without facing very difficult technical challenges. However, the scenario of large scale implementation of lithium-ion batteries to replace the internal combustion engines in automotive industry has risen concerns about the volume of lithium production as well as lithium reserves, and the potential resource shortage of lithium in the near future have been brought into discussion.[215–219] Meanwhile, with thorough studies from almost every aspect of lithium-ion batteries for more than four decades, it has become more and more clear that the possibility of drastic increase in the energy density is rather limited with lithium intercalation chemistry.[220] As a result, many academic and industrial research teams begin to investigate sodium intercalation compounds as well as room temperature sodium-ion battery systems with the hope of finding a low cost energy storage alternative to lithium-ion batteries.[212,221] In principle, the design of room temperature sodium-ion batteries can directly inherit most of the architecture of commercial lithium-ion batteries. Therefore the commercialization of sodium-ion battery technology can utilize the existing supply chain for lithium-ion battery production once sodium-ion batteries with equivalent performance to lithium-ion batteries become a reality. However, as useful as the research on new battery technology has been, great challenges in the development of commercial sodium-ion batteries are conspicuous.

The success of sodium-ion batteries inevitably requires both negative and positive electrodes with excellent characteristics similar to that of graphite, lithium cobalt oxide and their derivatives. However, both theoretical and experimental studies on a variety of positive electrodes for sodium batteries have shown that high voltage sodium intercalation compounds all have lower average operating voltages compared with their lithium analogs, which means sodium-ion batteries utilizing those potential cathode materials most likely will deliver lower level specific energy or volumetric energy density compared to lithium-ion batteries.[222,223]

Graphite, which is now the main choice of negative electrode for lithium-ion batteries, has a relatively small interlayer space for the insertion of sodium ions. It is generally accepted that graphitic carbon has only minimal capacity for sodium intercalation. Therefore other hard carbons with disordered graphitic planes are considered as the main anode candidates for sodium-ion batteries.[224]

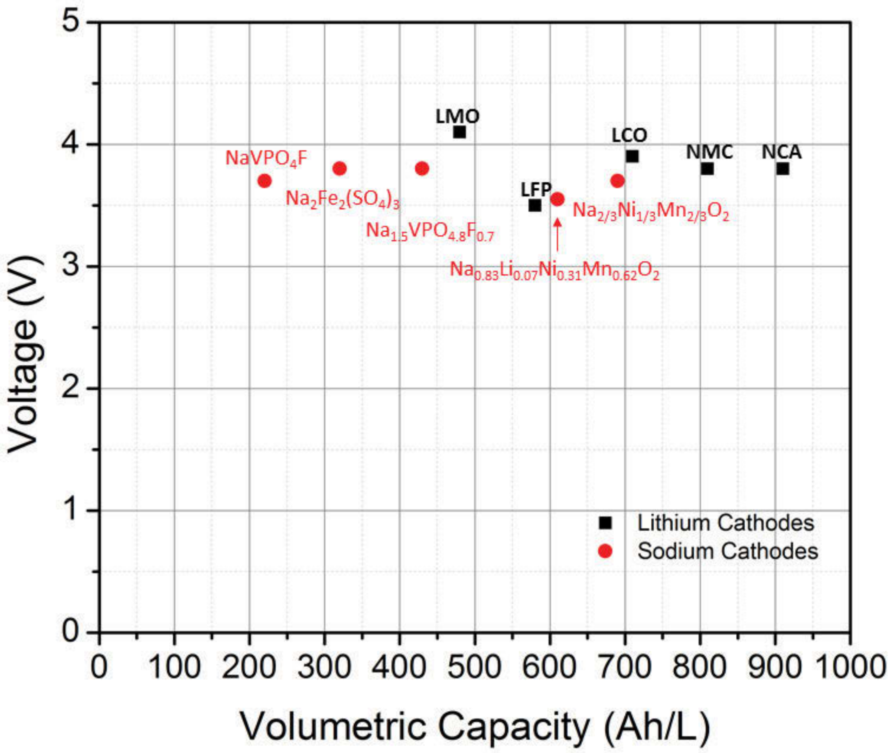

Figure 2.5. Average operating potentials versus volumetric capacity (Ah/L) of selected cathode materials for intercalation type lithium or sodium secondary batteries. The voltages of cathode materials are taken vs. Na^+/Na for sodium electrodes, or vs. Li^+/Li for lithium electrodes, respectively.[213,225]

A large volume change of anodes is associated with intercalation of relatively large sodium ions, so improvements in cycling performance have been mainly attributed to the use of better electrode binders such as carboxymethyl cellulose (CMC) and SEI stabilizing additives in carbonate-based electrolytes. These cannot be considered an ultimate solution, because stable SEI formation mechanism on the anode side of sodium-ion batteries is yet to be proven.[212] For cathode materials, the large size of sodium ions also poses intrinsic limitations on the achievable energy density of potential sodium-ion battery systems. As shown in Figure 2.5, much lower gravimetric and volumetric energy are certainly expected from sodium-ion batteries compared with that of lithium-ion batteries, regardless of the anodic reaction mechanisms (either intercalation, conversion or alloy reactions).[213,225] Therefore the applications of room temperature sodium-ion batteries are considered more suitable for medium and large scale stationary energy storage systems (which is similar to high temperature sodium secondary systems), rather than as power sources for portable electronics or small electric vehicles.

Chapter 3 Research strategy and experimental design

This chapter provides an overview of the general research methodology and experiment work- flow adopted for the complete research project including material synthesis, material physical property characterizations and electrochemical performance characterizations. The materials of interest in this particular project include carbon fibers, metal-carbon composite, metal chalcogenides and metal chalcogenides/carbon composite with nanoarchitectures. These materials are investigated as negative electrode materials in both lithium and sodium half-cells to evaluate their potential as anode materials for rechargeable lithium and sodium batteries. Electrospinning, solvothermal (including microwave assisted solvothermal) and high temperature annealing techniques are employed for material synthesis. Material characterization methods such as scanning electron microscopy, transmission electron microscopy, X-ray diffraction, thermal gravimetric analysis, Raman spectroscopy, etc. have been intensively involved for determining the properties of relevant materials as well as the failure mechanisms of electrodes in lithium battery related research. Detailed information regarding lithiation, delithiation, as well as failure mechanisms of electrodes during cycling will be obtained through a combination of these techniques. In this research project, scanning electron microscopy, transmission electron microscopy and x-ray powder diffraction are the main material characterization measures employed to determine the microstructural features of synthesized materials. The assembly of coin cells and relevant electrochemical tests including cyclic voltammetry, galvanostatic charge-discharge and electrochemical impedance spectroscopy will also be indispensable for more detailed exploration of the reactions of potential electrode materials for lithium and sodium secondary batteries.

3.1 Electrospinning technique for material synthesis

One-dimensional structure has been an objective for research due to its intriguing structure-related properties (e.g. large surface to volume ratio) in a variety of applications including filtration, medical treatment, photonics and electronics as well as energy storage. Electrospinning (electrostatic spinning) technique is a facile yet dynamic method to fabricate large scale non-woven materials based on polymer fibers. It is relatively convenient to synthesis one-dimensional pristine fibers or one-dimensional composite materials from precursor solutions via the electrospinning technique. The electrospinning technique is a variant of electrostatic spray (electrospray) process, which utilizes the high voltage induced liquid jet formation mechanism. It differs from the electrospray process in which small droplets and then solid particles are formed. The electrospinning process is aiming for the formation of solid fibers by stretching a continuous electrified polymer jet via electrostatic attraction and evaporation of solvents. The general material synthesis route utilizing electrospinning technique is shown in Figure 3.1. The electrospinning apparatus includes (i) a high voltage supplier which outputs a few tens of kV, (ii) a grounded collector, (iii) an electronic syringe pump, and (iv) a spinneret aperture.

During the electrospinning operation, polymeric solutions are fed through the spinneret by the syringe pump at a fixed, relatively low feed rate (normally at 1mL/hours), the solvent and solute in the extruded solutions are then separated under high strength electrostatic fields. The solvent evaporates while a jet of polymeric material forms stretched long polymer fibers accumulated on the surface of the collector layer by layer in a randomized manner. The resulted electrospun material normally appears to be a two-dimensional polymeric sheet in bulk with a high porosity architectures at the micrometer size scale.

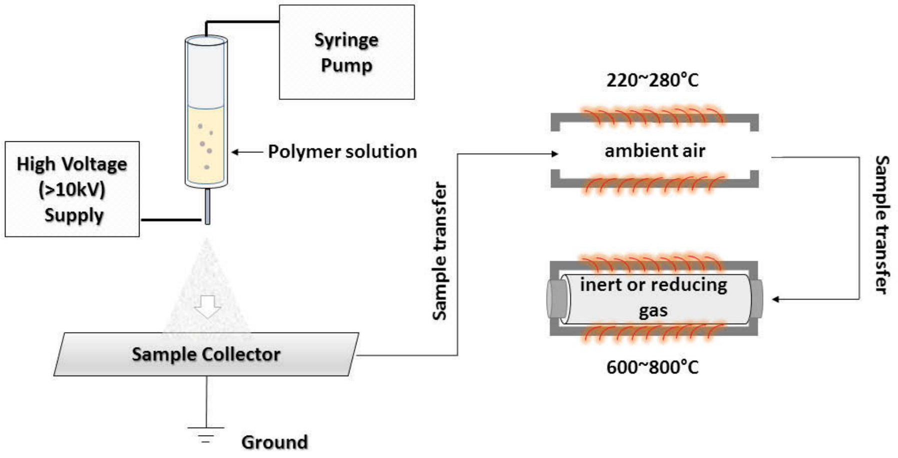

Figure 3.1 Schematic illustration of standard material synthesis procedures involving electrospinning and post thermal treatment.

Although electrospinning can be realized with a simple apparatus, its detailed mechanisms are rather complicated. The morphological features, mainly the fiber diameter, of electrospun materials, are highly dependent on a variety of factors. These include the type of precursor polymers, type of solvents, solution concentration, solution temperature, solution viscosity, solution conductivity, solution feeding rate, operation voltage, spinneret design, collector geometry and ambient conditions (e.g. humidity level, temperature level, etc.), some of which are interactive and inevitably increase the difficulties in determining the optimized electrospinning parameters. As a result, the process scale-up for electrospinning technology remains an issue for industrial application due to low material throughput, poor reproducibility and lack of precision control over the fabrication process, leaving large space for further improvements. In addition, the average length of electrospun fibers from many classes of materials are just a few millimeters or less, which is inadequate for some practical applications.[226]

The design of electrospinning apparatus includes direct electrospinning and co-electrospinning. The former refers to the simplest set up for electrospinning which is mostly used for bare polymer fiber synthesis, while the later refers to advanced apparatus with multi-channel solution transport system which allow electrospinning of two or more independent solutions in one process. The tuning of material composition and microarchitecture is normally difficult to obtain via direct electrospinning from single homogenous polymeric solution. In contrast, the co-electrospinning process utilizing a coaxial multi-channel spinneret offers more convenience in the synthesis of one-dimensional materials with complex microarchitectures such as core-shell or hollow fibers by electrospinning with two of more solutions simultaneously. In this project, all electrospinning work is carried with a direct electrospinning apparatus. The direct electrospinning process generally has a low productivity as the stretching of polymer molecules under high electrostatic charge is limited to small quantity of polymer solutions, and the composition of generated fibers is also limited for every single run of electrospinning process. Multiple needle arrays have been proposed to address this issue for large scale fiber productions but it is rather difficult to attain a design of spinnerets that can ensure the electric field strength is identical for all needle tips. The electrospinning device used in this project is a Nano NC® electrostatic spinning/spray integrated system with a direct spinning configuration.

Thermoplastic polyacrylonitrile (PAN) with a molecular weight above 150,000 g/mol is an ideal polymer source for synthesizing 1D carbon fibers via electrospinning and subsequential annealing and has been proven an excellent precursor after decades of industrial fiber production. Electrospun PAN fibers can maintain their morphology very well during high temperature pyrolysis, which is critical for material synthesis specifically targeting one-dimensional structures. 10% (weight/volume percentage concentration, w/v) PAN (M_w = 150,000g/mol) in N, N-Dimethylformamide (DMF) polymeric solution is used as the precursor solution for electrospinning in this project. The presence of co-existing bead and fiber morphology is a common issue for electrospun materials. The formation of beads is generally believed to be the results of higher surface tension and viscoelastic forces of polymer solutions compared with electrostatic repulsion forces, therefore the undesirable bead morphology can be suppressed with increased levels of applied voltage and solution viscosity (polymer concentration). In some cases, small amount of metal salts are included as solution additives in order to aid the electrospinning technique for synthesis of composite materials based on one-dimensional hydrocarbon fibers.

Electrospun PAN fibers are not suitable to serve directly as electrode materials for lithium or sodium batteries, but carbon fibers derived from PAN fibers can be used directly as binder-free, self-standing electrode materials, or as conductive substrates for synthesis of composite electrode materials. Thermal pyrolysis treatment is a well-established process to convert the organic materials into carbonaceous material. During the carbonization process, the electrospun fibers are surrounded by an inert or reducing atmosphere, with typical pyrolysis temperatures ranging from 700 to 1000°C. In order to maintain the original morphology of electrospun fibers, the thermal decomposition process of polymer fiber is divided into two stepwise stages. The first stage is commonly referred as the stabilization process where the polymer fibers is burned in ambient air at a temperature below 350°C, and the second stage is known as the carbonization process where the treated polymer fibers is heated in inert or reducing atmosphere at a temperature above 600°C. During the stabilization process, the prominent C≡N bonds in PAN polymer break and C=N bonds along with C=C and C-H bonds reform into a more stable aromatic cyclized ladder structure. Such deformation of molecular structure within the polymer fibers is beneficial as it prevents the fiber structure from melting down in the subsequent higher temperature annealing. During high temperature annealing, the remaining polymer molecules further decompose and leave a more carbonized structure. The temperature for the carbonization process are chosen from the thermal characteristics of polymer samples as well as the operation limits of the furnace. The carbon fibers prepared in such a way are normally amorphous in nature with rich C-H bonds. In the case of polymer fibers containing metallic or intermetallic secondary phases, the applied annealing temperature is also limited by the melting point of these metal elements because liquid metal may eventually accumulate and penetrate the walls of carbon fibers. The gas flow rate during carbonization is also critical for the surface features of resultant carbon fibers. A higher gas flow rate and slower temperature increase during the pyrolysis process of polymer fibers is more favorable for maintaining the integrity of carbon fibers. A strong gas flow flushes away released CO_2 thus prevent further reactions between CO_2 and carbon, which can lead to undesirable surface porosity or fracture of carbon fibers.

3.2 Solvothermal synthesis route

Hydrothermal and solvothermal are very common laboratory-scale synthesis routes in nanoscience and nanochemistry. The reactions are usually carried out in Teflon-lined stainless steel autoclaves which create a closed high temperature, high pressure environment therefore promoting nucleation and growth kinetics of crystallites that are difficult to achieve at ambient conditions. Both hydrothermal and solvothermal methods are capable of manipulating the nanoarchitectures of materials from precursors via control of experimental parameters including reaction time, temperature, surfactants, salt precursors, and solvents. The difference between hydrothermal and solvothermal synthesis routes is that hydrothermal uses aqueous precursor solutions whereas solvothermal uses nonaqueous precursor solutions. However, these expressions are sometimes confused in literature due to the complexity of precursor solution systems. In general, solvothermal synthesis is preferred over hydrothermal routes because it offers more benefits from additional sol-gel processes, and permits more precisely control of size, shape distribution of desired nanomaterials.

Conventional hydrothermal and solvothermal synthesis routes conducted with autoclaves often suffer from poor quality control over synthesized materials such as heterogeneity and batch-to-batch variations. The strong oxidizing or reducing agents used for reactions usually have high toxicities, and there is a risk of explosions due to high pressure in sealed reactors. All this makes both these synthesis routes difficult to scale up. These issues are partially attributed to the inherent limitations in the design of autoclaves, where a steep temperature gradient is inevitable during the synthesis process. Microwave-assisted hydro/solvothermal method is performed within a microwave reactor which offers a facile but fast synthesis approach using microwave heating to obtain nanomaterials at relatively lower temperatures and pressures thereby saving both time and energy in materials preparation.

3.3 Material characterizations

Scanning electron microscopy (SEM), transmission electron microscopy (TEM), Nitrogen adsorption surface area analysis (Brunauer, Emmett and Teller method), and

Raman spectroscopy were employed to examine material structures and phases. Powder X-ray diffraction (XRD) and thermogravimetric analysis (TGA) were used as the main technical means to determine the composition of composite materials.

3.3.1 Scanning electron microscopy

Scanning electron microscopes (SEMs) are a type of electron microscope that produce images of the surface area on a sample by scanning the sample with a focused beam of electrons. Common SEM operation is carried out under high vacuum conditions, where a beam of electrons emitted from an electron gun interacts with atoms in the sample thereby producing a wide range of signals that can be interpreted to reveal the surface topography and composition of samples. The image in a SEM may be obtained from detecting emitted secondary electrons from atoms excited by the electron beam on the surface of specimen. The number of secondary electrons depends on the angle at which electron beam contacted the surface of specimen. By scanning the sample and collecting the secondary electrons with a special detector, an image displaying the topography of the surface is hence created. SEM can achieve a high resolution at the scale of a few nanometers. Depending on the SEM instrument model, the observation of sample specimens can also be carried in low vacuum or even in wet conditions. The model of SEM employed for this research project was a Zeiss Supra 55VP which is located in the microstructural analysis unit (MAU) in the University of Sydney, Technology.

In a typical SEM, an electron beam is thermionically created with a tungsten filament cathode. The electron beam with the energy ranging from 0.2 KV to 30 KV, is focused by condenser lenses to a spot of a few nanometers wide. The beam passes through the electron column, which deflect the beam in the X and Y axes so that it scans in a raster pattern over a rectangular area of the sample surface. When the electron beam interacts with the sample, the energy of electrons is partially absorbed in the surface volume of specimen which extends to a few micrometers (usually less than 5 μm) into the surface. The size of the interaction surface volume depends on the electron's landing energy, the atomic number of the specimen and the specimen's density. The energy exchange between the electron beam and the sample results in the reflection of high-energy electrons by elastic scattering, emission of secondary electrons by inelastic scattering and the emission of electromagnetic radiation, all of which can be detected individually by specialized detectors. The beam current absorbed by the specimen can also be detected therefore images based on the current distribution on specimen can be created. Electronic amplifiers of various types are used to amplify the signals, which are displayed as variations in brightness on a computer monitor. Each pixel of computer video memory is synchronized with the position of the beam on the specimen in the microscope, and the resulting image is therefore a distribution map of the intensity of the signal being emitted from the scanned area of the specimen.

Magnification in a SEM can be controlled over a wide range up to 500,000 times. The image magnification of the SEM is not a function of the power of the objective lens but results from the ratio of the dimensions of the raster on the specimen and the raster on the display device. Assuming that the display screen has a fixed size, higher magnification results can be obtained by reducing the size of the raster on the specimen, and vice versa. Magnification is therefore controlled by the current supplied to the ***X***, ***Y*** scanning coils, or the voltage supplied to the ***X***, ***Y*** deflector plates.

SEM can also be used to perform analysis on the composition of samples via back-scattered electrons and characteristic X-ray techniques. Back-scattered electrons (BSE) are beam electrons reflected from the sample by elastic scattering and readily reveal the physical distribution of different chemical phases in the sample. Back-scattered electrons are typically emitted from a depth under the sample surface, therefore the resolution of back-scattering image is not as good as for secondary electrons. BSE are often used in analytical SEM along with the spectra made from wavelength-dispersive X-Ray spectroscopy (WDS) or energy dispersive X-ray spectroscopy (EDS), because the intensity of the BSE signal is strongly related to the atomic number of the specimen. BSE images can provide information about the distribution of different elements in the sample. Characteristic X-rays are emitted when the electron beam removes an inner shell electron from the atoms in the sample, causing a higher-energy electron to fill the shell and release energy. The emitted X-rays have energy characteristic of parent elements and therefore can be used to identify the composition and estimate the abundance of elements in the sample.

SEM operation has requirements on the electrical conductivity of specimens, and electrically grounded specimen holders need to be used to prevent the accumulation of electrostatic charge at the surface of specimens. All samples must be cleaned, dried and cut into an appropriate size to fit the top of the specimen holder. Nonconductive specimens tend to charge when in contact with the electron beam inside the specimen chamber, especially in secondary electron imaging mode. The charge can release electrical arcs that cause scanning faults and other image artifacts. Therefore samples with poor electrical conductivity are usually coated with an ultrathin layer of electrically conducting material on the surface, either by vacuum sputter coating or by vacuum evaporation. Common conductive materials used for SEM specimen coating include graphite, gold, and platinum. Coating with heavy metal elements is more effective on samples with low atomic numbers because additional metal layers on the specimen surface generally increases the signal/noise ratio hence degrading image quality. Back scattered electron imaging, quantitative X-ray analysis, and X-ray mapping of specimens often requires that the surfaces be ground and polished to a smooth surface. Specimens that require WDS or EDS analysis are often coated with carbon. Embedding specimen in a resin with further surface polishing to a mirror-like finish are also used for SEM sample preparation when operation with backscattered electrons or quantitative X-ray microanalysis are required.

3.3.2 Transmission electron microscopy

Transmission electron microscopy (TEM) is a microscopy technique utilizing interactions between electrons and the specimen with the electron beam being transmitted through the specimen. It has been a major analysis means for a range of scientific fields that are associated with material research due to its significant advantages in revealing information regarding the structure and composition of sample materials. TEM images are normally obtained through specially designed detectors which receive the emitted signals from samples. The contrast level of low magnification TEM images is a reflection of electron absorption in the sample material, where electron-dense compounds in the sample cast shadows on the detector screen thereby producing a two-dimensional projection of material in the sampled section. TEM is capable of visualizing samples at a much higher resolution compared to SEM owing to the small wavelength of propagating electrons which is generated by the high accelerating voltage, which enables the examination of fine details of sample material at the atomic level. In practice, the highest achievable resolution of TEM is limited to ~0.1 nm due to the physical limitations of objective lens system. Alteration of operation modes of TEM allows direct observation of chemical identity, crystal orientation, electronic structure and sample induced electron phase shift in addition to the electron absorption based image, the electron wave interactions are more complex in such cases and expertise is necessary for the analysis of observed high magnification TEM images.

Manipulation of the electron beam with TEM is possible due to two physical effects. First, the interaction between electrons and applied magnetic field leads to the movement of electrons following the left hand rule, thus allowing electromagnets to manipulate the electron beam. The use of magnetic fields allows for the formation of a magnetic lens of variable focusing power, the lens shape originating due to the distribution of magnetic flux. Secondly, electrons in electrostatic fields show a tendency to be deflected through a constant angle, therefore a shift in the beam path can be done by coupling two deflections in opposing directions with a small intermediate gap in the TEM column. Based on these two effects, accurate control over the beam path is possible for TEM operation. The optical configuration of a TEM can be rapidly changed by these lenses in the beam path.

Sample preparation procedures for TEM are more complex compared with that for SEM. TEM specimens are required to be no more than few hundreds of nanometers thick, as unlike neutron or X-Ray radiation the electron beam interacts readily with the sample, an effect that increases as a function of the square of atomic number. High quality samples will have a small thickness that is comparable to the mean free path of the electrons that travel through the samples, which may be only a few tens of nanometers. Preparation of TEM specimens is specific to the material under analysis and the desired information to obtain from the specimen. As such, many generic techniques have been used for the preparation of the required thin sections. Powder materials with nanoarchitectures are usually small enough to be electron transparent thus their specimen can be easily prepared by placing a drop of dilute sample solution onto a support grid. In material science and metallurgy the specimens may require etching to obtain thin layer specimens that allows electron beam penetration. Constraints on the thickness of the material are mainly limited by the scattering cross-section of the atoms from which the material is comprised. The normal thickness requirement for electron transparent specimens is around 100 nm, but this value is also subject to the electron beam accelerating voltage.

TEM specimen stage designs include airlocks to allow for insertion of the specimen holder into the vacuum with minimal increase in pressure in other areas of the microscope. Poor vacuum during TEM operation can cause severe issues on the specimen during observation due to the electron beam-induced deposition which causes electrical discharge, TEM operation with high voltage requires high vacuum conditions in the range of 10^{-7} to 10^{-9} Pa. The specimen holders are adapted to hold a standard size of grid upon which the sample is placed or a standard size of self-supporting specimen. Standard TEM grid are a 3.05 mm diameter ring made from copper, gold or platinum, with a thickness and mesh size below 100 μm. The sample is placed onto the inner area having diameter of approximately 2.5 mm.

The side-entry sample holder is the most common design in TEM configurations, where the specimen is placed in the hollow tip of a long metal (brass or stainless steel) rod. Along the rod are several polymer vacuum rings to allow for the formation of a vacuum seal of sufficient quality, when inserted into the stage. The stage is thus designed to accommodate the rod, placing the sample either in-between or near the objective lens, dependent upon the objective design. When inserted into the stage, the side entry holder has its tip contained within the TEM vacuum, and the base is presented to atmosphere, the airlock formed by the vacuum rings. Insertion procedures for side-entry TEM holders typically involve the rotation of the sample to trigger micro switches that initiate evacuation of the airlock before the sample is inserted into the TEM column. Once inserted into a TEM, the sample often has to be manipulated to present the region of interest to the beam path, such as in single grain diffraction, in a specific orientation. To accommodate this, the TEM stage may provide four degrees of freedom for the motion of the specimen including the translation of the sample in the X, Y plane of the sample, Z plane height adjustment of the sample holder, and at least one rotation degree of freedom for the sample. Most modern TEMs provide the ability for two orthogonal rotation angles of movement with specially designed double-tilt sample holders.

Imaging methods in TEMs utilize the information contained in the electron waves exiting from the sample to form an image. Projector lenses allow for the correct positioning of this electron wave distribution onto the viewing system. The observed intensity of the image can be approximated as proportional to the time-average amplitude of the electron wave functions. Different imaging methods therefore attempt to modify the electron waves exiting the sample in a form that is useful to obtain information with regards to the sample, or beam itself. The observed image depends not only on the amplitude of beam, but also on the phase of the electrons, although phase effects may often be ignored at lower magnifications. Higher resolution imaging requires thinner samples and higher energies of incident electrons. Therefore the sample can no longer be considered to be absorbing electrons, via a Beer's law effect, rather the sample can be modeled as an object that does not change the amplitude of the incoming electron wave function. The sample modifies the phase of the incoming wave; this model is known as a “pure phase” object, for sufficiently thin specimens, phase effects dominate the image, complicating analysis of the observed intensities. For example, to improve the contrast in the image the TEM may be operated slight defocused purposely to enhance contrast, owing to convolution by the contrast transfer function of the TEM. Contrast formation in the TEM is highly dependent on the operation mode. Complex imaging techniques, which utilize the unique ability to change lens strength or to deactivate a lens, allow for many operating modes. These modes may be used to discern information that is of particular interest to the investigator. The most common mode of operation for a TEM is the bright field imaging mode. In this mode the contrast formation, when considered classically, is formed directly by occlusion and absorption of electrons in the sample. Thicker regions of the sample, or regions with a higher atomic number will appear dark, whilst regions with no sample in the beam path will appear bright – hence the term "bright field". The image is in effect assumed to be a simple two dimensional projection of the sample down the optic axis, and to a first approximation may be modelled via Beer's law, more complex analyses require the modelling of the sample to include phase information. Samples can exhibit diffraction contrast, whereby the electron beam undergoes

Bragg scattering, which in the case of a crystalline sample, disperses electrons into discrete locations in the back focal plane. By the placement of apertures in the back focal plane, i.e. the objective aperture, the desired Bragg reflections can be selected (or excluded), thus only parts of the sample can cause the electrons to scatter and the selected reflections will end up projected onto the imaging apparatus. If the selected reflections do not contain scattered beam (which will appear at the focal point of the lens), then the region of imaging will appear dark, which gives the image known as the dark-field image.

Modern TEM models usually offer specimen holder tilt functions that allows rotation of the specimen within a range of angles in order to obtain specific diffraction conditions, and apertures placed above the specimen allow the user to select electrons that would otherwise be diffracted in a particular direction from entering the specimen Applications for this method include the identification of lattice defects in crystals. By carefully selecting the orientation of the sample, it is possible to not only determine the position of defects but also to determine the type of defect present. If the sample is oriented so that one particular plane is only slightly tilted away from the strongest diffracting angle (known as the Bragg Angle), any distortion of the crystal plane that locally tilts the plane to the Bragg angle will produce particularly strong contrast variations. However, defects that produce only displacement of atoms that do not tilt the crystal to the Bragg angle (i. e. displacements parallel to the crystal plane) will not produce strong contrast.

Crystal structure can also be investigated by high-resolution transmission electron microscopy (HRTEM), also known as phase contrast TEM. When utilizing a Field emission source and a specimen of uniform thickness, the images are formed due to differences in phase of electron waves, which is caused by specimen interaction. Image formation is generated by the complex modulus of the incoming electron beams. As such, the image is not only dependent on the number of electrons hitting the screen, making direct interpretation of phase contrast images more complex. However this effect can be used to an advantage, as it can be manipulated to provide more information about the sample, such as in complex phase retrieval techniques. As previously stated, by adjusting the magnetic lenses such that the back focal plane of the lens rather than the imaging plane is placed appropriately in the imaging apparatus a diffraction pattern can be generated. For thin crystalline samples, this produces an image that consists of a pattern of dots in the case of a single crystal, or a series of rings in the case of a polycrystalline or amorphous solid material. For the single crystal case the diffraction pattern is dependent upon the orientation of the specimen and the structure of the sample illuminated by the electron beam. This image provides the investigator with information about the space group symmetries in the crystal and the crystal's orientation to the beam path. This is typically done without utilizing any information but the position at which the diffraction spots appear and the observed image symmetries. Analysis of diffraction patterns beyond point-positions can be complex, as the image is sensitive to a number of factors such as specimen thickness and orientation, objective lens, spherical and chromatic aberration. Although quantitative interpretation of the contrast shown in lattice images is possible, it is inherently complicated and can require extensive computer simulation and analysis, such as electron multi-slice analysis. The TEM characterization work in this project was mainly conducted on a JEOL JEM-2011 electron microscope at the Institute for Superconducting and Electronic Materials (ISEM), University of Wollongong.

3.3.3 Powder X-ray diffraction

X-ray diffraction (XRD) is an analysis technique based on constructive interference of monochromatic X-rays (single wavelength with little deviation) with a crystalline sample, in which the periodic atoms or ions deflect the beam of incident X-rays into specific directions. The interaction of the incident radiation with the sample produces constructive interference (and a diffracted wave) when conditions satisfy Bragg's Law, which relates the wavelength of electromagnetic radiation to the diffraction angle and the lattice spacing in a crystalline sample. The smallest lattice spacing can be detected by a XRD instrument with the Cu radiation source is about 0.77 Å, which can be further enhanced down to about 0.35 Å by using a Mo radiation source. XRD technique is commonly used for identifying the crystal structure of solid materials, the characteristic x-ray diffraction pattern generated by measuring the angles and intensities of these diffracted beams provides a unique "fingerprint" of the materials present in the sample. When properly interpreted, this fingerprint allows identification of the crystalline form by comparison with standard reference patterns and measurements. In addition, the mean positions of the atoms in the crystal, their chemical bonds as well as various other information can also be determined by XRD measurements.

Crystals are considered as regular arrays of atoms, when an X-ray wave strikes a crystal material it generates a regular array of secondary spherical waves emitting from the excited electrons in the sample material. The majority of the scattered waves have the same wavelength as the excitation source (X-ray). This phenomenon is known as Rayleigh or elastic scattering, and the array of spherical waves add constructively in a few specific directions governed by the Bragg's law (as shown by equation 3-1).

$$2\boldsymbol{d}\sin\boldsymbol{\Theta} = \boldsymbol{n\lambda} \qquad 3\text{-}1$$

Here $\boldsymbol{d}$ is the spacing between crystallite planes, $\boldsymbol{\Theta}$ is the incident angle, $\boldsymbol{n}$ is a small integer, and $\boldsymbol{\lambda}$ is the wavelength of the beam. These specific directions appear as spots on the diffraction pattern called reflections. Thus, X-ray diffraction results from an electromagnetic wave (the X-ray) impinging on a regular array of electrons (in the repeating arrangement of atoms or ions within the material). Since many inorganic and organic materials comprise various crystalline structures, XRD analysis has found applications in many fields of scientific research. For materials science, XRD analysis is the primary characterization technique to determine the crystal structure of compounds, it can also be used for the characterization of amorphous materials, as long as suitable reference patterns are known or can be constructed by computer simulation.

X-rays are used to produce the diffraction pattern because their wavelength λ is typically the same order of magnitude (1~100 Å) as the spacing d between planes in the crystal. In principle, any wave impinging on a regular array of electrons produces diffraction. To produce significant diffraction, the spacing between the electrons and the wavelength of the impinging wave should be similar in size. The typical sub-nanometer level X-ray wavelength is ideal for determination of crystallite structure which is on the scale of covalent chemical bond-lengths and the radius of a single atom. Long wavelength photons such as ultraviolet radiation cannot provide sufficient resolution in mapping the atomic positions while short wavelength photons such as gamma radiation are generally difficult to focus and their strong interaction with atoms is destructive to the crystalline structure of sample material.

In general, single-crystal XRD offers more detailed structural information than any other XRD techniques, however, the samples of interest may not have a sufficiently large and uniform crystalline form. Rather than single-crystal XRD, various other X-ray methods such as powder X-ray diffraction and small-angle X-ray scattering (SAXS) can be applied. In powder diffraction, each possible crystalline orientation is present equally when the sample is in a fine powder form. The powder sample is filled in a disc shape sample container with its surface carefully flattened. The sample container is put on one axis of the diffractometer and tilted by an angle $\boldsymbol{\Theta}$ while a detector rotates around it on an arm at twice this angle. This configuration is known as the Bragg–Brentano $\Theta:2\Theta$ configuration. Another configuration is the Bragg–Brentano $\Theta:\Theta$ configuration in which the sample is stationary while the X-ray tube and the detector are rotated around it with fixed a $2\boldsymbol{\Theta}$ angle formed between the tube and the detector. This configuration is most convenient for loose powders. In this research project, the XRD instrument employed for power XRD measurements is a Siemens D5000 Diffractometer, which is located at microstructural analysis unit (MAU) in the University of Technology, Sydney. The minimum amount of sample required for a single run of XRD measurement is about 10 mg.

The most widespread use of powder diffraction is in the identification and characterization of crystalline solids, each of which produces a distinctive diffraction pattern. Both the positions (corresponding to lattice spacing) and the relative intensity of the lines in a diffraction pattern are indicative of a particular phase and material, and the size of X-ray diffraction peak is determined by the density of electrons within the specific crystalline structure. A multi-phase mixture, e.g. a ternary composite material, will show more than one pattern superposed, allowing for determination of the relative concentrations of phases in the mixture. Crystal structure determination from powder diffraction data can be challenging due to the overlap of reflections from a powder sample. A crystal structure, together with instrumental and microstructural information, is used to generate a theoretical diffraction pattern that can be compared to the observed data. A least squares procedure is then used to minimize the difference between the calculated pattern and each point of the observed pattern by adjusting model parameters.

3.3.4 Thermogravimetric analysis

Thermogravimetric (TG) technique is a method of thermal analysis, in which changes in physical and chemical properties of sample materials are measured as a function of increasing temperature, and as a function of time. The data generated from material combustion in typical TG measurement can provide useful information regarding the physical phenomena the sample shows at elevated temperature, such as vaporization, sublimation, desorption, thermal reaction, decomposition and phase transition reactions. TG analysis is commonly used to determine selected characteristics of materials that exhibit either mass loss or gain due to decomposition, oxidation or other reactions and loss of volatiles (such as moisture). Common applications of TG analysis are (1) materials characterization through analysis of characteristic decomposition patterns, (2) studies of degradation mechanisms and reaction kinetics, (3) determination of organic content in a sample, and (4) determination of inorganic (e.g. ash) content in a sample. Results may be useful for corroborating predicted material structures or simply used as a chemical analysis. It is an especially useful technique for the study of polymeric materials, including thermoplastics, thermosets, elastomers, composites, plastic films, fibers, coatings and paints.

Thermogravimetric analysis relies on a high degree of precision in three measurements: mass change, temperature, and temperature change. Therefore, the basic instrumental requirements for TG analysis are a precision balance with a pan loaded with the sample, and a programmable furnace. The TG furnace is equipped with a thermocouple to monitor accurate measurements of the temperature by comparing its voltage output with that of the voltage-versus-temperature table stored in the computer’s memory. A reference sample may be placed on another balance in a separate chamber. The atmosphere in the sample chamber may be purged with an inert gas to prevent oxidation or other undesired reactions. A different process using a quartz crystal microbalance has been devised for measuring smaller samples on the order of a microgram. TG analysis can be programmed either at a constant heating rate, or at heating to acquire a constant mass loss with time. Though a constant heating rate is more common, a constant mass loss rate can illuminate specific reaction kinetics.

The TG analysis instrument continuously weighs a sample as it is heated to the designated temperatures which is up to 2000 °C depending the specific instrument model. As the temperature increases, various components of the sample are decomposed and the weight percentage of each resulting mass change is recorded. Results are plotted with temperature on the X-axis and mass loss on the Y-axis. The data can be adjusted using curve smoothing and first derivatives are often also plotted to determine points of inflection for more in-depth interpretation. If the identity of the product after heating is known, then a ceramic yield can be found from analysis of the ash content. By taking the weight of the known product and dividing it by the initial mass of the starting material, the mass percentage of all inclusions can be found. Knowing the mass of the starting material and the total mass of inclusions, such as ligands, structural defects, or side-products of reaction, which are liberated upon heating, the stoichiometric ratio can be used to calculate the percent mass of the substance in a sample. The results from thermogravimetric analysis may be presented by (1) mass versus temperature (or time) curve, referred to as the thermogravimetric curve, or (2) rate of mass loss versus temperature curve, referred to as the differential thermogravimetric curve. Though this is by no means an exhaustive list, simple thermogravimetric curves may contain the following features (i) a horizontal portion, or plateau that indicates constant sample weight, (ii) a curved portion; the steepness of the curve indicates the rate of mass loss, (iii) an inflection (at which d$\boldsymbol{w}$/d$\boldsymbol{t}$ is a minimum close to zero). Certain features in the TG curve that are not readily seen can be more clearly discerned in the first derivative TG curve. For example, any change in the rate of weight loss can immediately be seen in the first derivative TG analysis curve as a trough, or as a shoulder or tail of a peak, indicating two consecutive or overlapping reactions. Differential TG curves also can show considerable similarity to differential thermal analysis (DTA) curves, which can permit easy comparisons of different samples in terms of thermal decomposition behaviors.

TG analysis has a wide variety of applications, including the evaluation of the thermal stability of a material under a certain atmosphere, and trace element identification. TG analysis also gives the upper limit temperature of a material, beyond which the material will begin to degrade. Mass losses or gains due to oxidation reactions are the most common phenomenon observed in the thermal treatment of materials, therefore this technique can be used to study the resistance to oxidation of a wide range of materials. If a species is thermally stable in a pre-determined temperature range against selected atmosphere, there will be no observed mass change, corresponding to a negligible slope in the weight-temperature plots. In this research project, TG analysis is employed mainly to determine the amount of metal or metal chalcogenides in carbon-rich composite materials. The TG measurements were performed with a TA Instruments® SDT 2960 thermogravimetric analyzer. Combustion of carbon-rich materials during TG analysis is a factor which needs to be treated with caution, as it may lead to release of particles in the form of smoke, which causes the loss of metallic or intermetallic elements from the sample without oxidation and further affects the accuracy of TG analysis results. The commonly used approach to avoid poor control over experimental accuracy during TG analysis is to reduce the gas flow and temperature ramp rates to the minimum level so that the highly undesirable release of smoke from sample material combustion can be suppressed.

3.3.5 Raman spectroscopy

Raman spectroscopy is a spectroscopic technique based on inelastic scattering of monochromatic light, usually from a laser beam. Photons of the laser light are absorbed by the sample, interact with molecular vibrations, phonons or other excitations in a material, and are then reemitted. The frequency of reemitted photons in monochromatic light changes upon interaction within a sample. The Raman effect refers to the shift of frequency of the reemitted photons towards lower or higher range in comparison with original frequency of the laser beam. The interpretation of frequency shifts provides information about vibrational, rotational and other low frequency transitions in molecules. It is commonly used in chemistry to identified unique patterns of specific molecules. The highly selective Raman spectroscopy allows easy identification and differentiation of chemical species with similar molecular structures, such as symmetric linkages (e.g. -C=C-, -C-S-) whose responses are generally weak in infrared spectra. Raman spectra can be collected from a very small volume specimen without the specimen being fixed or sectioned, and water content in the sample generally does not cause interference in Raman spectrum. This property facilitates the direct Raman spectrum measurements of a variety of materials including solids (e.g. particles, pellets, powers, films, fibers), semi-liquids (gels, pastes), and gases through a transparent media.

Raman shifts are typically recorded in wavenumbers, which have units of inverse length, as this value is directly related to energy. In order to convert between spectral wavelength and shift wavenumbers in Raman spectra, equation 3-2 can be used:

$$\Delta w = 1/\lambda_0 - 1/\lambda_1 \qquad 3\text{-}2$$

where Δw is the Raman shift expressed in wavenumber, λ_0 is the excitation wavelength, and λ_1 is the Raman spectrum wavelength. The unit chosen for expressing wavenumber in Raman spectra is commonly inverse centimeters (cm^{-1}). Since wavelength is often expressed in units of nanometers (nm), the formula above can scale for this unit conversion explicitly, giving equation 3-3:

$$\Delta w(cm^{-1}) = [1/\lambda_0\,(nm^{-1}) - 1/\lambda_1(nm^{-1})]\times 10^7 \qquad 3\text{-}3$$

Raman spectroscopy is commonly used in chemistry, since vibrational information is specific to the chemical bonds and symmetry of molecules. Therefore, it provides a fingerprint by which the molecule can be identified. The fingerprint region of organic molecules is in the (wavenumber) range 500–2000 cm^{-1}. The band areas of Raman spectrum are proportional to concentration, making Raman amenable to straightforward quantitative analysis as isolated sharp bands are often present in the spectrum.

In electrode material research, Raman spectroscopy is frequently used to analyze C-C bond types in carbonaceous materials where XRD measures are generally powerless due to the small size of sp^3 carbon domains mixed in a predominantly sp^2 carbon matrix (or vice versa). In a typical Raman spectra of carbon material, two major band peaks i.e. the D band (k point phonons of A_{1g} symmetry) and G band (phonons of E_{2g} symmetry) can be observed. The D band and the G band correspond to the vibration of defect-related sp^3-bonded carbon atoms and sp^2 carbon atoms, respectively. The intensity ratio of D and G band peaks in Raman spectra can be used directly to determine the abundance of the graphitic structure (sp^2 carbon) or the non-graphitic structure (sp^3 carbon) in a carbonaceous material. For this research project, the Raman spectroscopy measurements were performed with a Renishaw inVia® Raman system equipped with a 17mW helium laser source (633 nm wavelength).

3.3.6 Gas adsorption surface area analysis

Gas adsorption measurements are based on the tendency of gases to lightly adhere (adsorb) on the surface of solid materials. At low relative pressure and super low temperature, the gas molecule adsorption process on the surface of a sample (adsorbent) is kinetically reversible with increased relative pressure. Such physical adsorption has fixed equilibrium adsorption amounts corresponding to the environmental pressure, which can be used to calculate the surface area of samples, which includes the bulk surface area of sample and the surface area of gas-accessible internal open pores of sample. Nitrogen is the most common adsorbate used for gas adsorption measurement owing to its availability and good adsorbate characteristics for both adsorption and desorption processes.

Surface area analysis by gas adsorption can be classified into two classes: one is based on a sample's adsorbed gas amount, and analysis methods can be divided into dynamic chromatography methods, static volumetric methods and gravimetric methods. The second class uses the basis of a different theoretical model, such as the contrast reference method, the Langmuir method, the BET (Brunauer, Emmett and Teller) method etc. The contrast reference method has limits in dynamic chromatography to measure adsorbate amounts, and the Langmuir method is limited to monolayer sample analysis. However, the BET method is suitable for both dynamic chromatography and static volumetric method to measure adsorbate amounts. Assuming no interactions between the adsorption layers in the sample, BET correlations on multilayer adsorption can therefore be expressed as:

$$\frac{P}{V\cdot(P_0-P)}=\frac{1}{C\cdot V_m}+(\frac{P}{P_0})\cdot\frac{C-1}{C\cdot V_m} \qquad 3\text{-}4$$

Where V is the sample adsorption amount, V_m is the monolayer saturation adsorption amount, C is the adsorption ability constant, P is the adsorbate equilibrium pressure, and P_0 is the adsorbent saturation vapor pressure. From above equation, it can be clearly seen that BET method sets up quantity relations between monolayer saturation adsorption amount V_m and multilayer adsorption amount. BET equation established in multilayer adsorption theory which is very close to many material's real adsorption processes, thus the analysis data are reliable.

During multipoint BET analysis procedures, multilayer adsorption amount V with 3 ~ 5 groups of relative pressures are collected. By plotting $P/V\cdot(P_0\text{-}P)$ versus P/P_0 (i.e. taking P/P_0 as the X-axis, and $P/V\cdot(P_0\text{-}P)$ as the Y-axis), the monolayer saturation adsorption amount V_m and the adsorption ability constant C can be calculated by linear fitting of $P/V\cdot(P_0\text{-}P)$ against relative pressure. It is generally accepted that BET equation fits more closely to real adsorption processes and the best line fitting can be obtained by picking P/P_0 points located within the range 0.05 to 0.35. In case the analyzed sample shows strong adsorption ability (a relatively high value of C), the single point BET method can be adopted. The intercept of the straight line is nearly close to zero, thereby can be roughly deemed as connected to the origin point. Therefore, only one group P/P_0 value is necessary in the analysis and it can be linked with the origin coordinates to calculate the specific surface area of the sample. However, the surface area data obtained with such a method has bigger errors when compared with multilayer BET. The correlation coefficient and the adsorption ability constant are two key indexes to check the validity of BET analysis results. The correlation coefficient should be greater than 0.9975, typically coefficients obtained from successful measurement should be more than 0.9997. The adsorption ability constant ***C*** indicates whether the BET analysis is valid for the sample of interest, any BET analysis reports with a ***C*** number less than 2 should be rejected. If employing dynamic chromatography for the BET method, a highly accurate apparatus with the capability of measuring different $\boldsymbol{P/P_0}$ adsorption amounts is required. Once the $\boldsymbol{V_m}$ is determined, then the specific surface area of measured sample (***S***) can be calculated according to equation 3-5.

$$\boldsymbol{S} = \frac{\boldsymbol{N}\cdot\boldsymbol{V_m}\cdot\boldsymbol{i}}{22400\times\boldsymbol{m}}\times 10^{-18}(\mathrm{m}^2/\mathrm{g}) \qquad 3\text{-}5$$

Where ***N*** refers to the Avogadro constant, ***i*** is the cross section of adsorbate molecule (16.8 Å in the case of nitrogen gas adsorption), ***m*** is the mass of sample, and the definition of $\boldsymbol{V_m}$ is the same as in equation 3-4. The specific surface area calculated based on the BET method is represented by the amount of nitrogen molecules covering the surface area of the sample as well as the maximum cross-sectional area inside the sample which is accessible to nitrogen molecule.

For this research project, the nitrogen adsorption/desorption experiments and relevant data processing were carried out with a Micromeritics 3Flex® surface analyzer. Samples are pre-treated by a degas process at the highest temperature possible (without damaging the structure of sample) to ensure the complete removal of superficial impurities before the gas adsorption measurement. The general guideline for degassing time is recommended to be at least 16 hours. The surface characteristics of samples including the specific surface area, surface pore size distribution and surface porosity are calculated automatically with associated computer software by inputting the re-weighed, degassed sample mass value after each measurement. The desorption branch of the isotherm, for the same volume of gas, exhibits a lower relative pressure, resulting in a lower free energy state which is closer to real thermodynamic stability compared with the adsorption isotherm. Thus the desorption isotherm is used for evaluating the pore size distribution of an adsorbent. The calculated pore size dictates the category of sample in the porous materials family. There are three major groups of porous materials, i.e. microporous, mesoporous and macroporous materials. Microporous refers to pore size smaller than 2 nm, mesoporous refers to pore size between 2 to 50 nm, and macroporous refers to pore size larger than 50 nm, respectively.

3.4 Electrochemical Characterizations

The evaluation of electrodes in electrochemical cells allowing prolonged cycling of batteries can provide sufficient information to determine whether they are suitable for further development towards high energy batteries. Conventional methods include cycling lithium half-cells and full cells at constant voltage, current, and capacity limits, as well as electrochemical impedance spectroscopy (EIS) and dilatometry. The latest developed electrochemical characterization techniques also include in situ high precision calorimetry and acoustic emission.

3.4.1 Electrode preparation and cell configurations

In general, the electrode materials of interest for lithium or sodium secondary batteries are powder samples and need to be diluted in a solvent together with adhesives (binder) and conductive agents, thus mixed materials form a slurry which is subsequently coated on copper or aluminum electrode substrates with a method often referred as the doctor blade technique. The composition of electrodes is determined by the weight ratio of active material, binder, and conductive agent, which is usually set to fixed weight ratio of 8:1:1 by default. The ratio of active material in test electrodes is relatively lower than that of commercial lithium-ion battery electrode coatings due to the high surface area characteristic of investigated material, which requires more conductive carbon and binder to cover the surfaces of active material particles. After coating electrode slurry on the substrate, the wet electrode is dried at elevated temperature under vacuum to remove solvent content. In addition to drying, the electrode is further densified with high pressure in order to improve the contact of particles inside the electrode. A roll press process may also be used for electrode densification, so that the porosity in the electrode film can also be adjusted to control the electrolyte loading in the porous structure electrode. After the series of pre-treatments mentioned above, the electrode is cut into proper shape to fit into the desired cell configurations. Electrochemical evaluation of electrodes and battery systems can be performed with different cell configurations including half-cells, symmetric cells and full cells. Each of these cell configuration has its own advantages and limitations and one should be careful to choose the proper configuration and interprets the results obtained from electrochemical tests.

Lithium and sodium half-cell configurations are adopted in this project due to their convenience in cell assembly. The half-cells are prepared by assembling type 2032 type coin cells (20 mm in diameter, 3.2 mm in height) in argon atmosphere inside a glove-box with both moisture and oxygen levels below 1ppm. Metallic lithium and sodium are used as counter electrodes. Porous polypropylene membranes and glass fiber membranes in circular shape with 18 mm diameters are used as separators for lithium and sodium half-cells, respectively. The default electrolyte for lithium half-cells is 1M $LiPF_6$ in 1:1 (v/v) ethylene carbonate (EC) and diethyl carbonate (DEC) without electrolyte additive, while the default electrolyte for sodium half-cells is 1M $NaClO_4$ in 1:1 (v/v) ethylene carbonate (EC) and dimethyl carbonate (DMC) with 2%(w/v) fluoroethylene carbonate (FEC) additive. The assembled cells are left to rest for at least 12 hours before performing any electrochemical characterization work. This process allows the separators soaked in electrolyte to fully cover the surfaces of both negative and positive electrodes which ensures optimized electronic/ionic conductivity between two electrodes in the cell. Half-cells are the most frequently used cell models for cycling tests due to convenience in preparation. Lithium half-cells consist of metallic lithium and electrolyte at levels excess to the electrode materials being evaluated, this also applies to sodium half-cells. The assembled half-cells are normally cycled in constant current mode, in which the cells are charged and discharged at the same current within a fixed voltage window of upper and lower cut-off limits. One advantage of the half-cell evaluation is that with excessive lithium and electrolyte supply, the cycle life of half-cells used for laboratory experiments can be extended to a few hundreds of cycles with minimum risk of encountering electrolyte consumption related failure. Therefore, capacity fading in half-cells during cycling can be directly attributed to the failure of electrodes and SEI related causes. However, the long term cycling of lithium or sodium half-cells also has potential risks of dendrite growth from metallic anodes and subsequent internal shorts. The products from continuous SEI formation over long cycles can also result in a critical point in the capacity versus cycle number plot where impedance growth can cause the voltage plateau to drop close to the cutoff potential of electrode, thereby accelerating capacity deterioration. Constant capacity cycling has also been used to evaluate the cycling performance of electrode materials, and this method is more frequently used for dealing with electrode materials whose voltage limits are difficult to define.[53] It can be effectively used to compare the effects of different lithiation stages as well as alloy volume expansion during cycling.

For those electrode materials showed little or zero fading during cycling with half-cell configurations. Further cycling evaluation with symmetric cells can be used. Symmetric cell configurations use identical electrodes by replacing the lithium foil in half-cell configuration with one electrode in the lithiated state. Similar to half-cell configuration, the symmetric cells still contain excess electrolyte, thereby eliminating the possibility of impedance growth on a Li foil electrode or possible electrode interactions. In addition to any fading mechanisms recognized in half-cells, symmetric cells may have fade originated from lithium-consuming reactions within the electrolyte. Symmetric cells are therefore most useful when assembled for further screening electrolytes and electrolyte additives.

The full-cell configuration is indispensable in order to make a thorough evaluation of cycling performance of negative/positive electrodes towards practical battery applications. Considering the realities of the state-of-art in commercial lithium-ion batteries, the benchmark for the areal capacity of the electrode coating should be no less than 2 mAh/cm^2. In full-cell configurations the negative electrode is required to slightly overlap the positive electrode, giving a ratio of the areal capacity of the negative electrode to the positive electrode (N/P) between 1 and 1.2. As a safety precaution, the higher areal capacity at the negative end can prevent metal plating on the edge area of the electrode. The amount of electrolyte needs to be sufficient to wet the separator and fill the porous structure inside electrodes while without flooding the cell. In addition, the minimum requirement for the Coulombic efficiency of electrodes in a full cell in each cycle should be at least 99.9% as this is the minimum CE value that allows 80% capacity retention after 200 cycles of charge-discharge process.

3.4.2 Cyclic voltammetry

Cyclic voltammetry (CV) is a specialized technique that can be used to acquire the information on electrochemical reactions in almost all electrochemical systems. CV measures the response current of the working electrode at a predetermined constant voltage/time sweeping rate in a cyclic manner, thus the plot of electrode current versus electrode voltage, also known as the voltammogram, forms a loop with peaks. The current peaks in a CV plot indicate oxidation and reduction reaction potentials as well as the rate of reactions during ion insertion and extraction processes, respectively. In a half-cell configuration battery, the synthesized materials are used as the working electrode and the lithium or sodium metal are used as both counter electrode and reference electrode. The CV measurements is usually starting from the cathodic scan for the reductive reactions of the working electrode, and then moves to the anodic scan for the oxidative reactions of the working electrode. All CV measurements of lithium and sodium half-cells in this research project are performed with CHI 660 series electrochemical workstations with a fixed scanning speed at 0.1 mV/s. The typical potential region selected for negative electrodes and positive electrodes are 0.01V ~ 2.5 V, and 1.0 V ~ 3.0 V, respectively.

3.4.3 Charge-discharge cycling test

Charge-discharge cycling tests are basic tests frequently used to generate the charge-discharge profiles of batteries for further analysis of battery performance including specific capacities, capacity retention rates and rate capabilities. A typical cycling test is performed by applying a constant current to or from the cell being tested within a fixed voltage window. The voltage window is subject to the type of electrode materials used, but in general, the voltage range for negative electrode materials is from 0.01 V to 2.0 V, while the voltage range for positive electrode materials is from 2.0 V to 4.0 V. The current density in galvanostatic cycling mode is often expressed as the ***C***-rate in literature, which is calculated based on the ratio of the applied current and the charge/discharge capacity of batteries; a typical 1/2 ***C***-rate means the applied current is enough for the battery to charge or discharge completely in two hours. The charge stored in the electrode, also referred to as the specific capacity ($\boldsymbol{q}$), can be calculated by multiplying of the applied current ($\boldsymbol{i}$) and the charge or discharge time ($\boldsymbol{t}$), and then divided by the mass of active materials in the electrode ($\boldsymbol{m}$), as shown in equation 3-6.

$$\boldsymbol{q} = \boldsymbol{i} \times \boldsymbol{t} / \boldsymbol{m} \tag{3-6}$$

Voltage plateaus in the form of sharp peaks can be easily identified in the differential capacity (d$\boldsymbol{Q}$/d$\boldsymbol{V}$ versus $\boldsymbol{V}$) plots of charge-discharge cycling profiles. In differential capacity plots, the height and area size of voltage peaks represent the steadiness of the voltage plateau and the capacity of active material at the designated voltage, respectively. Therefore it is convenient to use differential capacity analysis (DCA) to monitor the voltage evolution of active materials during cycling and phase transitions and distinguish the independent behavior of specific active materials in multi-component composite electrodes.[227,228] The electrochemical behavior of the active phase in an electrode material is dependent on the domain size, with single phase reactions being kinetically favored to reduce domain size, giving differential capacity the ability to monitor microstructural change during cycling. DCA is therefore highly sensitive to the micro- or even nano-structure of active materials and provides data with considerable accuracy.[229]

The charge-discharge cycling tests are sometimes performed with various current densities to evaluate the rate capacity of electrode materials, and their potential impact on the power capability of proposed battery systems. In general, the electrode materials show a trend that the reversible capacities are always lower during fast charge or discharge compared with slow charge or discharge. This phenomenon is attributed to the slow kinetics of ion mobility in bulk electrode materials. Under high current rate, the movement of ions towards deep areas in electrodes becomes more and more difficult as the electrode is charged and ions eventually accumulate on the surface area of electrode. The rate capacity can be improved by nano downsizing of active materials' particles and increasing the mass ratio of conductive agent in the electrode, thus reduced ion diffusion length and enhanced electrical contact can be realized within electrode.

3.4.4 Cell impedance

For this research project, alternating current electrochemical impedance spectroscopy technique was employed to measure the impedance of lithium and sodium half-cells. Electrochemical impedance spectroscopy (EIS) is a widely used measurement in battery studies due to its convenience. Briefly, the impedance spectrum of an electrochemical cell is plotted based on the response of cell to an applied sinusoidal voltage of a given amplitude (5mV by default) within the frequency range from 100 kHz to 0.01 Hz. This impedance plot is also referred as the Nyquist plot. The typical Nyquist plot consists of a sloping line across the low frequency and middle frequency region, and a semicircle begins in the middle frequency region and ends in the high frequency region. The high frequency part of the Nyquist plot is related to electronic conductivity, while the middle frequency region corresponds to charge transfer resistance (R_{ct}, resistance against the transfer of lithium or sodium ions between the electrolyte and the electrode), and the low frequency region of the Nyquist plot is related to bulk diffusion resistance. The spike in the low frequency region of the Nyquist plot usually becomes shorter with increased cycle number of examined electrodes/cells. This phenomenon can be explained by the morphology change of porous electrodes. Since the penetration depth of AC signals is highly dependent on the pore size of electrode materials, less AC signals can penetrate through the surface of long cycled electrodes, due to the increased ratio of closed pores inside electrode materials and the accumulated passivation layer on the electrode/electrolyte interphase from electrolyte decomposition.

The equivalent circuit of cells that have both capacitance and resistance can be fitted to the EIS data by specialized software such as Z view®. In the case of a negative electrode, the middle frequency region is highly sensitive to the deterioration of SEI and the conductivity within the electrode, as a result, the width of the semicircle (the value of R_{ct}) normally increases with cycle number due to cell polarization. The ion diffusion coefficient (***D***) of an electrode can be calculated using the following formula：

$$\boldsymbol{D} = \frac{\boldsymbol{R}^2\boldsymbol{T}^2}{2\boldsymbol{A}^2\boldsymbol{n}^4\boldsymbol{F}^4\boldsymbol{C}^2\boldsymbol{\sigma}^2} \qquad 3\text{-}7$$

Where ***T*** is the absolute temperature, ***R*** is the gas constant, ***A*** is the surface area, ***n*** is the number of electrons involved in the electrochemical reaction, ***F*** is Faraday's constant, ***C*** is the concentration, and ***σ*** is the Warburg coefficient obtained from the intersection of the straight line on the real axis. However, it should be noted that the porous nature of electrode coatings poses difficulties in the determination of active surface area during electrochemical reactions, sometimes giving unreliable calculated. Another method for tracking the impedance of electrodes with cycling history is the addition of a rest step at the end of each lithiation and delithiation process, through which the time dependence of the voltage relaxation can be used as an impedance metric. This approach is a variant of the traditional areal impedance metric.[230]

Chapter 4 One dimensional carbon fiber synthesis by electrospinning

4.1 Introduction

One-dimensional (1D) microarchitecture offers structural features including high surface area (large surface-to-volume ratio) and short ion diffusion length. Compared with other synthesis approaches (e.g. self-assembly, template-assisted synthesis, chemical vapor deposition, solvothermal or hydrothermal synthesis), the electrospinning (also known as the electrostatic spinning) technique offers a more convenient and versatile synthesis route for the fabrication of materials with one-dimensional microarchitecture, and its simplicity in apparatus setup is extremely attractive for laboratory scale research.[231,232] The fibrous materials obtained from electrospinning process usually have a high porosity three-dimensional (3D) morphology owing to the stacks of electrospun polymer fibers. The polymer fibers can be further converted into carbon fibers which offer improved electron conductivity in a reducing or inert atmospheres at high temperatures. [233,234] The polymer molecules inside electrospun composite materials can also be completely removed by high temperature treatment in an oxygen-containing environment, which leaves desired nanostructure networks.[235,236] These features of electrospun polymer fibers allow easy synthesis of nanoscale materials without severe aggregation of particles, which is beneficial for the preparation of nanoscale electrode materials for rechargeable lithium and sodium batteries. However, the precisely control of electrospinning process from a variety of polymeric solutions remains a challenge because of the complex physical behavior of electrified jets and the other interdependent factors (e.g. solution properties, electrospinning apparatus design, process parameters, and ambient conditions) which greatly affect the properties of electrospun fibers.[237,238] In addition, there are also large numbers of materials being excluded from the candidate list for fiber material fabrication with electrospinning process due to their poor performance in viscoelastic behavior, solubility, or polymer molecule entanglement, etc.[239]

Similar to other fiber processing techniques, the final properties of carbon fibers are largely determined by the precursor materials and the processing conditions for forming the polymer fiber, while post-treatment techniques (e.g. stretching and carbonization) only offer limited refining to the morphology and properties of electrospun fibers. In order to obtain high performance carbon nanofibers, it is critical to determine the processing windows of key processing parameters for electrospun materials fabrication.[240–245] As a result, the determination of (i) the optimized polymeric solution systems and (ii) optimized process parameters of a specific electrospinning system is an indispensable step for the preparation of 1D functional materials with electrostatic spinning. In experiments for the determination of optimal electrospinning conditions, solution concentration and acceleration voltage are chosen as the main variables because both of them are unanimously accepted in the literature as factors that have a great influence over the morphology of electrospun fibers. More importantly, they can be adjusted with relatively high accuracy compared to other variables in the electrospinning process. After the optimal polymer solution formula and stable process parameters being confirmed, further investigation on the optimized thermal post treatment conditions of electrospun polymeric materials are conducted. The PAN-derived carbon fibers are examined as negative electrode materials for lithium-ion and sodium-ion batteries. The electrospinning technique is also applied in the synthesis of

1D structure composite electrode materials including antimony-carbon fibers, and antimony-carbon fibers with graphene as discussed in the following chapters.

4.2 Experimental

The polymeric solutions used for the electrospinning experiments are polyvinyl alcohol (PVA, M_w = 89,000 ~ 98,000 g/mol, 99+% hydrolyzed) aqueous solutions (with 1% v/v Triton X-100) and polyacrylonitrile (PAN, M_w = 150,000g/mol) in N,N-Dimethylformamide (DMF) solutions. Chemicals used were purchased from Sigma-Aldrich® and used as received. Both solutions were prepared with three concentrations: 6%, 8% and 10 wt% (w/v) by dissolving accurately weighed polymer powders in solvents. Solution viscosities of prepared solutions were measured with a Brookfield® controlled stress rheometer in a cone and plate geometry, and each measurement is performed at 25°C with a 4 cm and 2°cone. In a typical electrospinning fiber formation experiment, solutions are loaded in a 10 ml syringe. The applied accelerating voltage for electrospinning ranged from 5.0 ~ 25.0 kV. A grounded rotating drum covered with aluminum foil was used as fiber collector, and the gap between the needle tip and the surface of collector is about 15 cm. Since the NanoNC® electrospinning system does not offer any ambient condition (e.g. temperature, humidity) control functions, all electrospinning experiments were conducted in optimal ambient conditions with room relative humidity (R.H.) level below 55%, and room temperature between 20°C and 23°C.

The experimental procedures for the concentration/voltage dependence of electrospun fiber morphology is as follows. Firstly, 1 ml of a polymer solution was loaded in a 10 ml syringe, with the front end of the syringe sealed by a stainless steel spinneret connected to a bland tip 27 gauge needle with ca. 0.21 mm inner diameter. The syringe was then clamped to an electronic syringe pump, and the power supply wire was secured to the spinneret. An initial pressure was applied to the syringe plunger so that a small drop of solution is pushed from the syringe to form a suspended liquid on the tip of needle. Once this stable initial condition was achieved, the switch of the high voltage power supply was turned on to initiate the electrified jet. With a fixed solution feeding rate of 1 ml per hour, the time for sample collection is about 1 hour, during which a white color electrospun fiber mat is deposited on the surface of aluminum foil. The collected electrospun fiber mats were dried under vacuum at 60°C to remove the solvent residual, and then stripped from the aluminum foil. The morphology of obtained fibers were examined by scanning electron microscopy (SEM). For SEM sample preparation, the fiber mats are cut into small pieces, placed on carbon tapes, and flushed with nitrogen air flow. The SEM image of obtained polymer fibers are all at low resolution as the heat generated from the concentrated electron beam can melt the polymer instantly at high magnification, even with an acceleration voltage as low as 2kV.

The samples that showed minimum microstructure defects under SEM examination were selected as precursors for electrode material preparation. During a typical two-step thermal post treatment process, the pristine polymer fibers were first heated in ambient atmosphere at 250°C ~ 350°C which allowed reactions with oxygen to form more stable polymer structures (stabilization).Then, heating in high purity argon atmosphere at 700°C or 800 °C completed the polymer decomposition (carbonization). The electrospun PAN fibers were placed in an alumina boat and transferred into a tube furnace, the fibers were stabilized in air for 2 hours at 250 °C, then carbonized by heating the fibers for at least 5 hours in a constant argon flow of 0.100 sccm at 700°C and 800°C. The ramp rate was fixed at 5 °C/min and 2 °C/min during the stabilization and carbonization stages, respectively.

The resulting materials were further characterized with SEM, XRD and Raman spectroscopy to investigate their morphological features as well as chemical compositions. The structure of the thermal treated fibers was examined by powder X-ray diffraction technique using a Siemens® diffractometer with a wavelength at Cu-Kα = 1.5406 Å. The XRD patterns were obtained from pulverized fibers with a typical exposure time of 1 hour. Raman spectra of the carbon fibers were taken with a Renishaw® Raman spectrometer under 514.5 nm wavelength laser excitation. The nitrogen adsorption-desorption isotherms obtained by a Micromeritics 3Flex® surface analyzer at 77 K are used to determine the Brunauer, Emmet and Teller (BET) surface area of obtained carbon fibers. The samples were degassed at 373 K under nitrogen atmosphere for 20 hours prior to the measurement.

For electrochemical tests, the electrospun carbon fiber mat obtained after 700°C treatment was cut into circular disks (16 mm in diameter) and served as working electrodes in 2032 coin cells. Na or Li metal foil are used as the counter-electrodes in corresponding cells. The details of cell assembly procedure are described in Chapter 3, section 3.4.1. Galvanostatic charge-discharge cycling tests were performed with assembled lithium and sodium cells under 100 mA/g constant current, between 0.01 V and 3.0 V voltage window, at room temperature.

4.3 Results and discussion

4.3.1 Solution concentration

The viscosity and surface tension of solutions are two key concentration-dependent factors that affect the continuous fiber formation during electrospinning. In general, low viscosity - high surface tension solutions intend to form liquid drops instead of fibers in electrostatic field, while high viscosity solutions will prohibit the stable solution flow being extruded from the syringe needle. As a result, the combination of solution viscosity and surface tension dictates the boundaries of the electrospinning processing window, with other factors remaining unchanged. Within the fiber processing window, the morphology of electrospun polymer fibers varies with altered solution concentrations.

Figure 4.1 shows the SEM images of electrospun PVA and PAN fibers produced with 20 kV applied voltage, 15 cm working distance, from solutions with 6%, 8% and 10 % concentrations. At the low concentration (6%), both PVA and PAN fibers show an irregular morphology with junctions and bundles of fibers, the fiber diameters also show large variations due to severe bead formation. The presence of fiber junctions and bundles of fibers from the 6 wt% solutions is evidence of coexistence of polymer and solvents in the sample. At higher concentration (10%), the PVA and PAN fibers show regular morphology and the diameters of cylindrical fibers appears to be more uniform on average. The disappearing of fiber bundles and junctions indicates that the solvent is removed before electrospun fibers reach the sample collector. The differences in sample morphology can be seen as a reflection of the lower level surface tension and solvent residual in the electrospun sample from high concentration solutions. This can be corroborated by the variation of mass deposition rates with different concentration solutions, as weighed mass depositions at fixed time (1 hour) are found to be higher with low concentration solutions but lower with high concentration solutions. The general trend of concentration dependence of electrospun fibers shown by SEM leads to a preliminary conclusion that the average diameter of electrospun polymer fibers increases with increased precursor solution concentration.

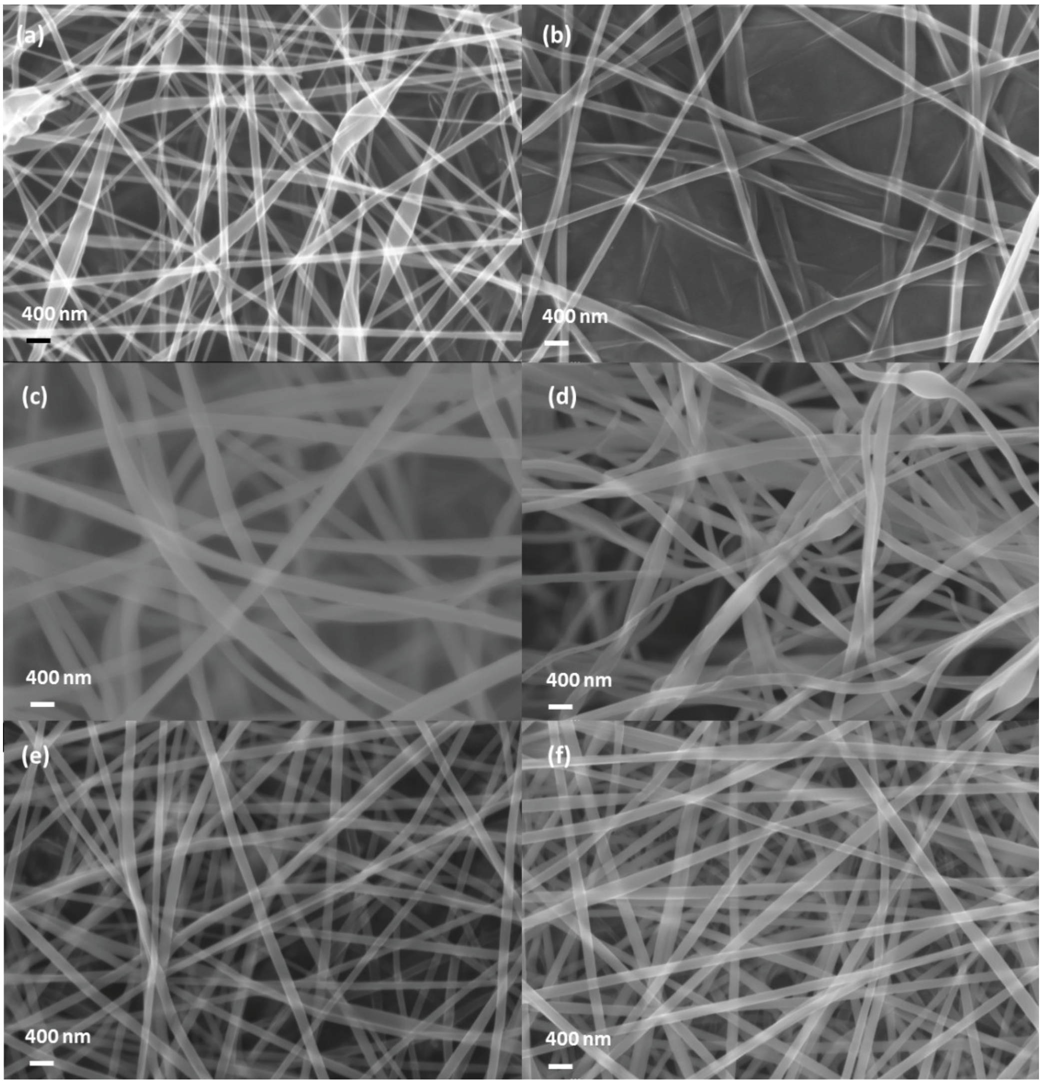

Figure 4.1 SEM images of electrospun polyvinyl alcohol and polyacrylonitrile fibers. Fibers were from PVA aqueous solutions with (a) 6%, (b) 8% and (c) 10 % concentrations, and polyacrylonitrile fibers produced from PAN/DMF solutions with (d) 6%, (e) 8% and (f) 10 % concentrations.

In addition, it has been noted in the experiments of electrospinning with PVA aqueous solutions that those aqueous solutions containing highly hydrolyzed PVA molecules have difficulty to form cylindrical fibers regardless of other process variables (e.g. voltage, solution concentration, and solution feeding rate). Based on a previous study[246], the poor fiber formation kinetics originate from the high surface tension of fully hydrolyzed PVA aqueous solutions, therefore additional surfactant is necessary for the PVA aqueous solutions preparation in order to reduce the surface tension to an acceptable level for the electrospinning process. With 1% (volume ratio) Triton™ X-100 (t-oct-C_6H_4-$(OCH_2CH_2)_xOH$, x = 9~10) surfactant, the electrospinning PVA fibers can obtain a near perfect fiber morphology without droplet defects within the electrospinning process window.

4.3.2 Applied voltage

During the electrospinning process, the stretched fibers that carry electrostatic charges naturally form a closed circuit between the spinneret and the grounded fiber collector, and the associated electric current along fibers is constantly monitored with an integrated amp meter. Compared with the electrostatic charges, the electrical current formed by ionic conduction within the polymer fiber is negligible, therefore the changes in the strength of electrospinning current can be considered as the reflection of the fiber generation rate, which is mainly determined by the initiating voltage with other variables fixed. The SEM images of electrospun fiber generated at different voltages can be used to predict the domain of voltages where targeted polymer fiber diameter can be achieved.

The morphology of electrospun PVA and PAN fibers (both from 10% concentration solutions) changes from droplet-fiber coexistence at an initiating voltage below 12.5 kV, to defect-free fibers at an initiating voltage ranging from 15 kV to 20kV, and further evolves to bead-fiber coexistence at an initiating voltage above 25 kV. For both PVA and PAN solution system studied, the density of bead structure becomes higher with increased voltage above 25 kV, coincident with the significant increase of electrospinning current from below 0.001 mA at 15 ~ 20kV, to 0.006 ~ 0.009 mA at 25~30 kV.

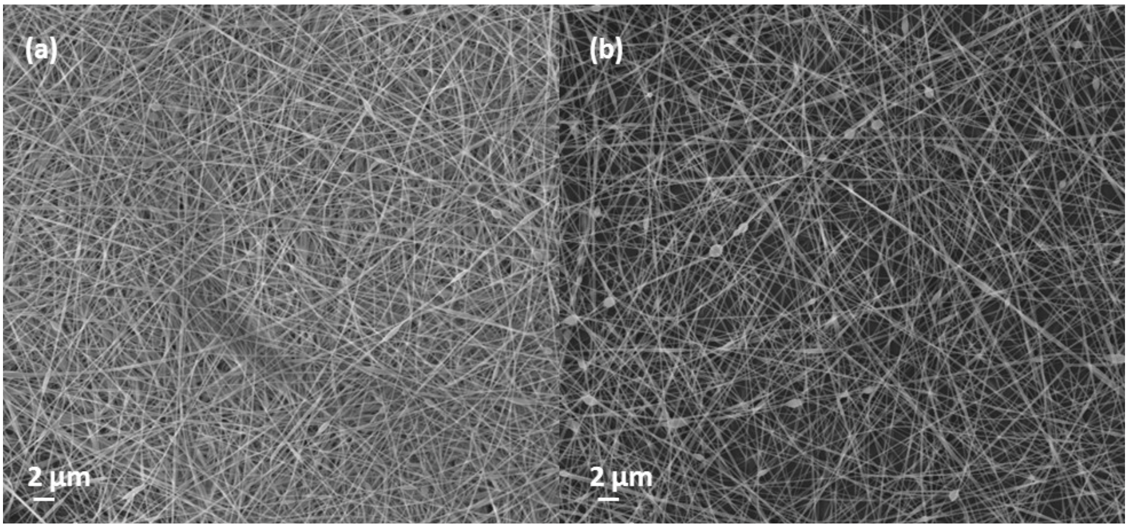

Figure 4.2 SEM images of polyacrylonitrile fibers at different voltages. Fibers from 8% concentration PAN/DMF solutions under (a) 20 kV, and (b) 25 kV applied voltages at 15 cm working distance.

The change in fiber morphology with voltage correlates to changes in the shape of initiating droplet at the syringe needle tip. At lower voltages, a droplet of solution remains suspended at the end of the syringe needle, with the joint between electrospun fiber jet and the droplet forming a cone shape, which is in agreement with Taylor's theory.[247] For a viscous fluid, the jet originates from the bottom of a drop whose diameter is larger than the capillary diameter. The polymer fibers produced under these conditions have a smooth cylindrical morphology with minimal structure defects presented under SEM (as shown in Figure 4.2a). However, it is also observed that the volume of the suspended droplet at the end of the needle tip decreases following an increased voltage. At voltages above 25 kV, the droplet on the needle tip completely disappears and the fiber jet is directly initiated from solution inside the needle tip. The electrospun fibers under this condition essentially have a cylindrical morphology, but there is a dramatic increase in bead defects present in the electrospun fiber sample (as shown in Figure. 4.2b). The results on varying applied voltage for the electrospinning process demonstrated that, above a critical voltage, there are significant changes in the shape of the originating droplet and the voltage dependence of the electrospinning current. The reflection of these changes on the electrospun material morphology is an increase in the number of bead defects observed in the electrospun fiber mats.

The change in the shape of the liquid surface corresponds to a change of the solution throughput at the capillary tip. Increasing the voltage causes the rate (I) at which solution is removed from the capillary tip to exceed the rate (II) at which the solution is being pushed through the needle tip by the plunger. Therefore the conical shape droplet on the syringe needle tip is impossible to maintain under such circumstances, and it further results in a less stable yet sustained polymer jet.[248] The experimental results on varying voltages with fixed solution feeding rates suggest that fiber bead density increases with the increased instability of the electrified jet, hence the bead formation during electrospinning can be minimized by monitoring the electrospinning current and adjusting applied voltages accordingly.

In summary, within the processing window of electrospinning, higher applied voltages can increase the fiber deposition rate and reduce the average diameter of obtained fibers. The fiber generation rate and the process stability of electrospinning can be monitored through the change of electrical current, which is mainly determined by the initiating voltage.

4.3.3 Change of PAN fibers after thermal treatment

Thermal decomposition post treatment is a common approach to convert electrospun polymer fibers to carbon fibers. The more rigid carbon fibers offers more appealing characteristics for electrode material applications compared with their parent polymer precursors. The key in the conversion process of electrospun polymer fibers is to maintain the integrity of 1D microarchitectures and therefore the rate of oxidizing reactions during the thermal treatment need to be carefully controlled. In industrial applications, PAN fibers are commonly used as the precursor for carbon fiber production. This thermoplastic polymer naturally transfers into an intermediate with more stable structure under heat and therefore retains the original fiber morphology upon high temperature carbonization. The principle mechanism behind this phenomenon is the cyclization and dehydrogenation of PAN molecules within the temperature range from 280°C to 350°C, and these reactions take place regardless of the surrounding atmosphere being vacuum, air, or inert gases such as nitrogen or argon. Compared with PAN, the PVA polymers are less favored as the precursors for carbon material conversion due to their poor thermal stability (low boiling point 228°C). Therefore, electrospun PAN fibers were used as samples for determination of optimal post thermal treatment conditions.

Figure 4.3 shows SEM images of electrospun polymer fibers after stabilization, and carbonization processes at different magnifications. After a typical 1 hour time of electrospinning, the as-spun polymer fibers formed a low density mat on the collector surface. The resulting PAN fibers had a uniform cross section with an average diameter of 220 ± 50 nm, with minimal beads or joints. After a 4 hour stabilization process, part of PVA fibers despaired, while the average diameter of treated PAN fibers changes to 170 ± 50 nm, with the fibrous mat turning into dark brown color and appearing to be more fragile compared with raw PAN fiber sheet. After the carbonization process, the shape of mat was maintained but the size shrinks, and the average diameter of carbonized fibers also dropped to 160 ± 40 nm. To investigate the transverse structure of carbonized PAN fibers, the pulverized fiber samples were dispersed in ethanol with an ultrasonic bath. The as-prepared suspensions were dropped onto carbon tapes and dried at 110°C under vacuum, then transferred to SEM for further characterization.

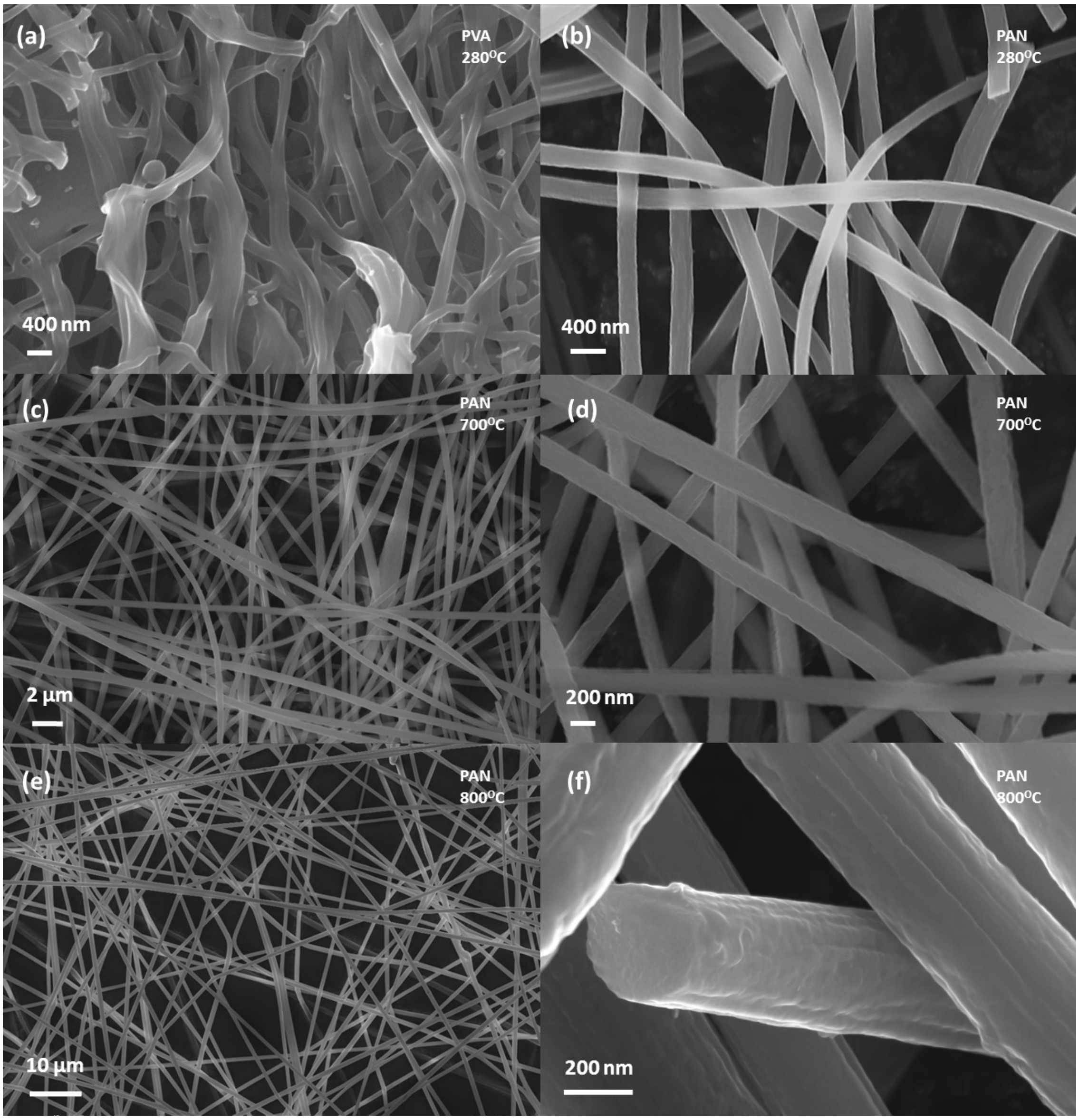

Figure 4.3 SEM images of polyvinyl alcohol and polyacrylonitrile fibers after thermal treatments. (a) polyvinyl alcohol fibers heated in air at 280°C for 4 hours, (b) polyacrylonitrile fibers heated in air at 280°C for 4 hours, (c) and (d) polyacrylonitrile fibers after heated in argon at 700°C for 2 hours, (e) and (f)polyacrylonitrile fibers after heated in argon at 800°C for 2 hours.

As shown in Figure 4.3f, the high resolution SEM image reveals the heterogeneity of carbon fibers in the transverse direction, with a few nanometer thick tubular sheet structure oriented along the surface of fibers and granular structure in the core area of carbon fibers.

Heating rate, in conjunction with the inert gas flow rate, plays an important role that determines the carbonization degree and mass loss of polymer fibers during the high temperature carbonization process. The optimized temperature ramp rate to gas flow ratio is beneficial for the structural integrity of PAN derived carbon fibers as the released oxygen-containing groups from decomposed polymer can be readily removed by inert gas flow thereby avoiding further reactions between the converted carbon and oxygen. A high ramp rate with low level gas flow generally increases the consumption of carbon on the fiber surface by oxygen gas, leaving surface defects and fractures in resultant carbonized fibers. By SEM observations on PAN derived carbon fibers obtained from thermal decomposition in oxygen-containing atmosphere, inert gas atmospheres and reducing gas atmosphere under varied ramp rate and gas flow rate, the optimal process parameters for thermal post treatment of PAN fibers were determined by comparing the morphology of carbon fibers.

Figure 4.4a shows the X-ray diffraction pattern of pulverized carbon fibers converted from electrospun PAN fibers at 700°C and 800°C. Both samples exhibit a broad diffraction peak centered at the 2Θ angle of ca. 24°, and a weak reflection centered at the 2Θ angle of ca. 43°, corresponding to the carbon orientation along the (002) *hkl* and (100) *hkl* direction, respectively. Figure 4.4b shows Raman spectra of two carbon fiber samples within the wavelength range between 500 cm^{-1} and 2500 cm^{-1}. Both samples show two broad overlapping peaks centered around 1360 cm^{-1} and 1589 cm^{-1}. The ratio of the integrated intensity of the D and G peaks, $\boldsymbol{R} = \boldsymbol{I}_D/\boldsymbol{I}_G$, characterizes the disorder in the carbon fiber and is an index of the ratio of disordered carbon structure and ordered carbon structure.

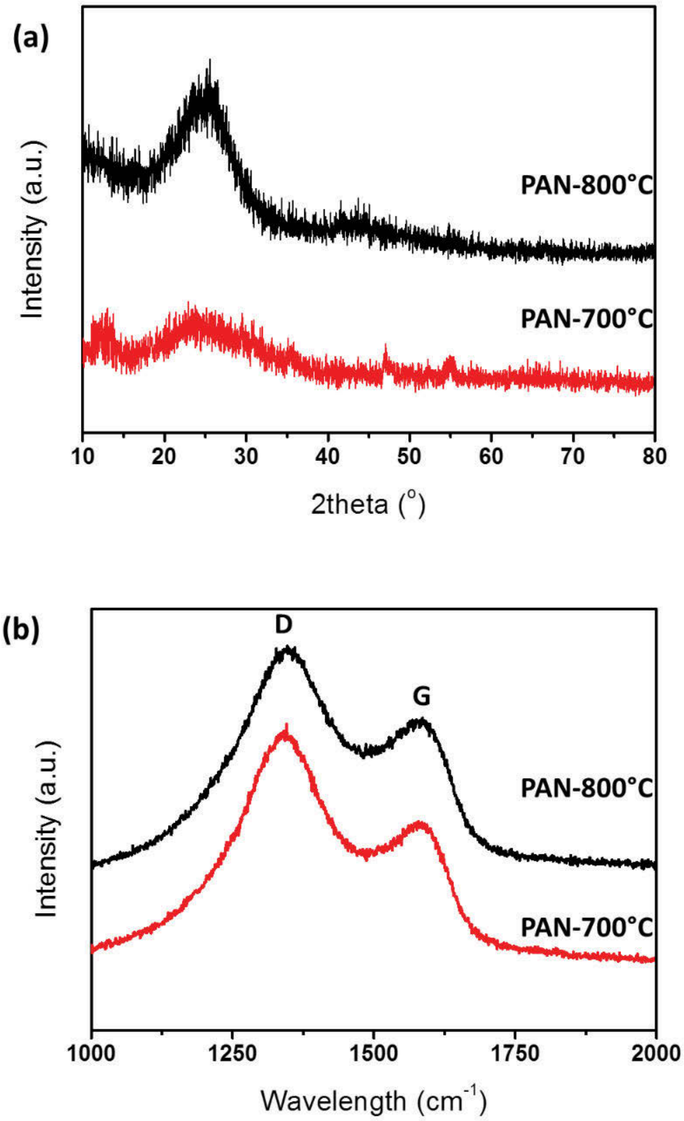

Figure 4.4 XRD patterns (a) and Raman spectra (b) of PAN-derived carbon fibers. Samples were collected with different carbonization temperature at 700°C and 800°C.

The Raman spectra of two carbon fiber samples showed a decrease in the value of intensity ratio $\boldsymbol{R}$ with increased carbonization temperature. The lower $\boldsymbol{R}$ values of Raman spectra is apparently indicative of a more ordered carbon structure in the carbonized fibers. However, due to the relatively larger size of the laser focus spot diameter of the Raman spectrometer used for the spectrum measurement compared with the average diameters of the carbonized fiber, it is impossible to distinguish between the skin and the core of obtained carbon fiber. Hence changes of disorder degree of carbon fibers from surface to center were not investigated.

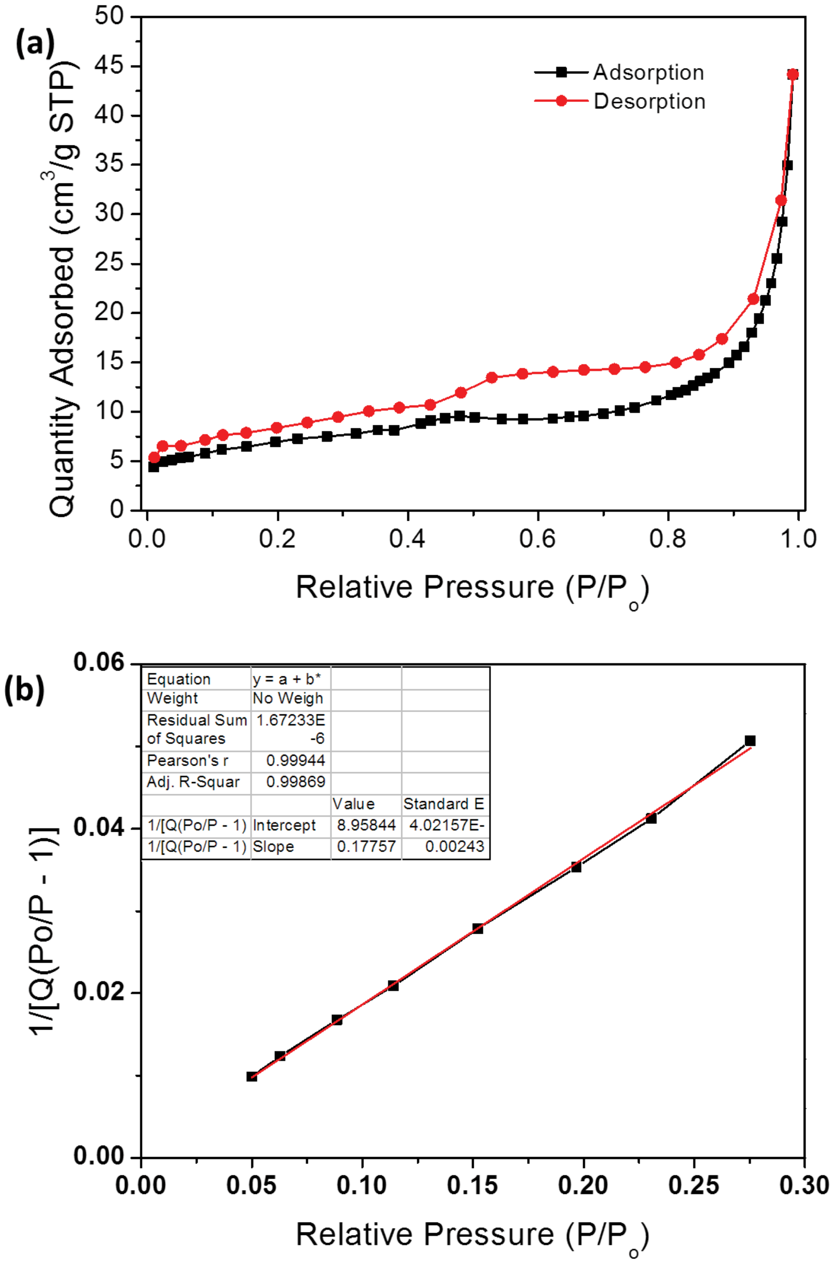

Equation	y = a + b*		
Weight	No Weigh		
Residual Sum of Squares	1.67233E -6		
Pearson's r	0.99944		
Adj. R-Squar	0.99869		
		Value	Standard E
1/[Q(Po/P - 1)	Intercept	8.95844	4.02157E-
1/[Q(Po/P - 1)	Slope	0.17757	0.00243

Figure 4.5 Nitrogen adsorption-desorption isotherms (a) and the BET plot (b) from PAN-derived carbon fibers after 700°C carbonization.

Figure 4.5a shows the nitrogen adsorption-desorption isotherms of carbon fibers converted from electrospun PAN fibers at 700°C. The specific surface area of carbon fiber sample is calculated to be 24.39 m^2/g according to the linear regression results of the Brunauer, Emmet and Teller (BET) plot as shown in Figure 4.5b.

4.3.4 Galvanostatic cycle tests carbon fiber electrode

The typical galvanostatic curves of the carbon fiber electrodes in lithium and sodium half-cells are shown in Figure 4.6 a and b, respectively. The galvanostatic voltage curves in both lithium and sodium cells show a sloping voltage region without low-potential plateau in their charge and discharge steps, suggesting the lithium or sodium insertion and removal are between parallel or nearly parallel carbon layers. The potential decreases with increasing lithium or sodium content inside carbon electrode mainly because the lithium or sodium atoms between carbon layers changes the potential for further insertion or removal of metal ions.[224]

The reversible capacities and coulombic efficiencies of carbon fiber electrodes versus lithium and sodium are presented in Figure 4.6c and d, respectively. For lithium cells, the carbon fiber electrode shows 120 mAh/g reversible capacity, and 66.2% initial coulombic efficiency at 100 mA/g current density. The low initial coulombic efficiency is attributed to rapid decomposition of electrolyte and the formation of a solid electrolyte interphase (SEI) film on the surface of carbon fiber electrode, as explained in section 2.2. During the subsequent cycles, the carbon fiber electrode maintains reversible capacities at levels above 118 mAh/g, the coulombic efficiency rapidly increases to 95.5% at the second cycle and remains at levels above 98% after the ninth cycle, implying a stable SEI film on the surface of electrode.

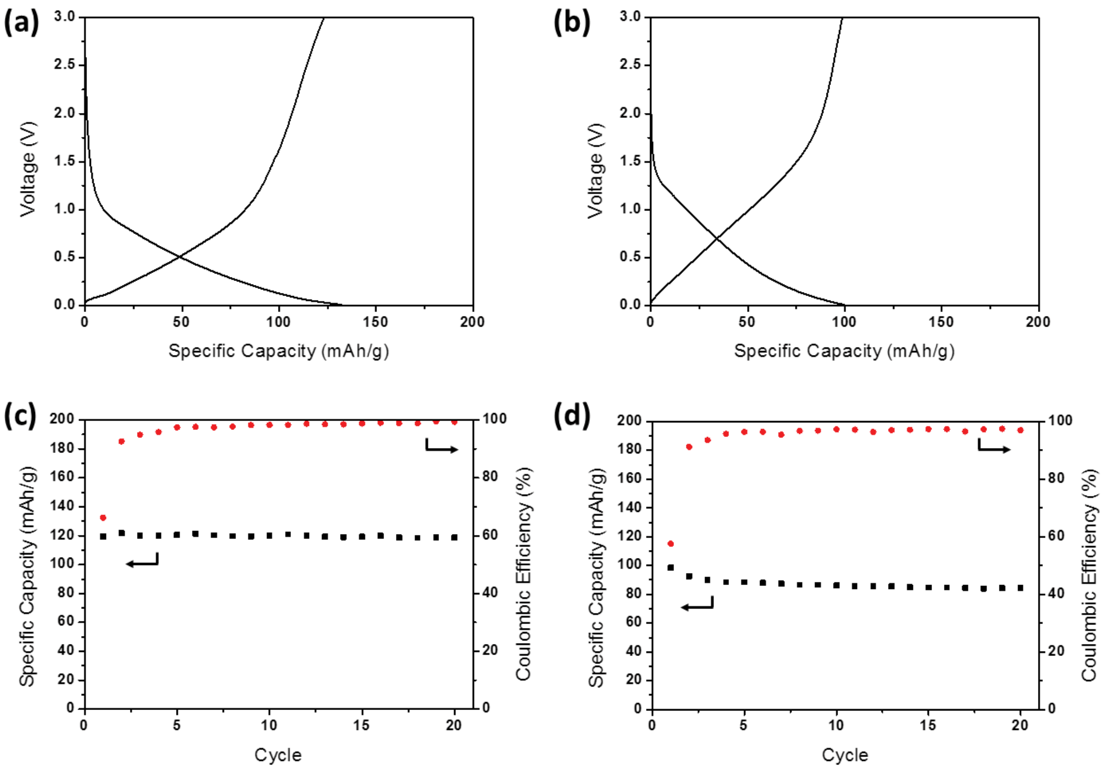

Figure 4.6 Galvanostatic profiles of PAN-derived carbon fibers electrode in lithium (a) and sodium (b) cells. The reversible capacities and coulombic efficiencies of carbon fiber electrodes in lithium (c) and sodium (d) cells under 100 mA/g current.

The carbon fiber electrode demonstrate a 98 mAh/g reversible capacity during the initial charge process in the sodium cell. The reversible capacity of carbon fiber electrode faded moderately in the sodium cell at the first few cycles, which can be attributed to structural breakdown of the nanostructure within carbon fibers due to the insertion and extraction of large sodium ions. The capacity loss eventually decreases with the cycle number increases. After the initial four cycles for decreasing capacities, the overall charge and discharge capacities remain stable at 84 mAh/g. During the initial cycle, the sodium cell also showed a low coulombic efficiency at 57%. The large irreversible capacity loss during the first cycle is mainly caused by SEI formation on the large surface area electrode, which is the same as that in lithium cell. As shown in Figure 4.6

c and d, the overall coulombic efficiencies of the sodium cell are slightly lower compared to that of the lithium cell, which suggesting a less stable SEI layer on the surface of carbon in sodium cell. Nevertheless, the electrochemical tests results of obtained carbon fibers have already revealed that this material can be used to synthesize alloy or conversion type binder-free composite electrode materials for lithium and sodium secondary batteries. The synthesis of composite electrode based on electrospun carbon fibers will be discussed in the following chapters.

4.4 Conclusion

In this work, the one dimensional material preparation route with an electrospinning technique was demonstrated. The concentration of polymer solution and applied voltage are found to be the critical process parameters that affect the quality of resultant electrospun fibers. With high temperature pyrolysis, electrospun PAN fibers can be converted to carbon fibers, while the PVA fibers failed to maintain morphology under similar conditions. After pyrolysis in inert gas atmosphere, freestanding carbon fiber sheet with a typical specific surface area 24.39 m^2/g is obtained. The PAN-derived carbon fiber shows stable reversible capacities of 118 mAh/g and 84 mAh/g as electrode materials in lithium and sodium cells, respectively. Together with its conductive nature, this material poses considerable technological potential for electrochemical devices or catalyst substrates. However, the materials synthesized with the electrospinning process still exhibit poor reproducibility due to the lack of control over the fiber morphology.

Chapter 5 Antimony - carbon alloy type negative electrodes

5.1 Introduction

Antimony is among those low voltage alloy type anode materials for rechargeable lithium batteries and the reversible lithiation/delithiation process of antimony has been well known to the lithium battery research community for a long time.[133] Despite its high theoretical specific capacity for lithium storage owing to its alloy reaction mechanisms with lithium, antimony based anodes have never been implemented in practical lithium secondary batteries. This status is partially attributed to the relatively high average potentials of lithium-antimony alloy reactions (0.85 V for lithiation and 1.05 V for delithiation), the narrowed voltage gaps between the antimony anode and the common 4 V cathode materials leads to decreased theoretically achievable energy density compared to lithium-ion batteries with graphite/lithium cobalt oxide electrode couples. In addition, the alloy based antimony anodes also experience the universal problem of alloy type anode materials i.e. the large volume change during cell operation, which eventually causes the failure of batteries upon repeated charge/discharge processes. Despite many difficult technical challenges for its implementation in practical batteries, antimony based composite materials remain an interesting subject as an alloy type anode in the emerging research of rechargeable sodium batteries. Both bulk and nanostructured antimony have shown high and stable specific capacities from the reversible alloy/de-alloy reaction as well as excellent rate performance in sodium cells, which is just slightly lower than its analogues in lithium batteries.[249,250] The alloy/de-alloy processes between lithium and antimony form intermediate phases (LiSb, Li_2Sb and Li_3Sb) as predicted in the Li-Sb phase diagram, while the alloy/de-alloy process between sodium and antimony forms amorphous Na_xSb intermediate phases.

The differences in the phase transition behavior of M_xSb (M = Li, Na) originate from the crystal form of cubic Li_3Sb and hexagonal Na_3Sb. The longer strain propagation length in Na_3Sb favors the formation of amorphous Na_xSb phases during the alloying process.[251] Alloy type antimony anodes can deliver a good cycling performance in rechargeable sodium batteries comparable to that in rechargeable lithium batteries, and this unique electrochemical property of antimony has inspired some research efforts that focused on the innovative design of electrode materials based on antimony/carbon composites.[252–255] The implications of Na/Sb alloy reactions are that conversion type intermetallic compounds once investigated as potential electrode materials for rechargeable lithium batteries may still be applicable for rechargeable sodium batteries, and certain improvements in terms of electrochemical properties can be expected.

Both reduced graphene oxide (RGO) nanosheets and carbon fibers offers good conductivity and structure flexibility, which make them ideal host structure for the synthesis of composite electrode materials. Chemically reduced graphene oxide (RGO) usually has a high level of non-stoichiometric defects which are preferable features as they enhance the storage capability for cations such as lithium and sodium ions. The high purity pristine graphene nanosheets, on the contrary, have only minimal morphology defects. The defects in RGO consist of hydroxyl, epoxide, and other carboxyl functional groups which are formed during the oxidation process of graphite. RGO with disordered graphene layers remains a material with high conductivity as well as structure flexibility. These features make RGO an ideal host material for composite electrode material synthesis. In addition, they also provide intermediate level sodium storage capacity as anode materials in sodium batteries. Taking these factors into account, an antimony/carbon composite material was developed with the hope of utilizing a conductive network comprised of PAN-derived carbon fibers and RGO nanosheets, to serve as a binder-free negative electrode material for rechargeable sodium batteries. The analysis of testing results confirmed that it is an effective strategy to achieve good cycling performance of alloy based antimony anode, owing to the favorable physical and chemical properties of PAN-derived carbon fibers and graphene.

5.2 Experimental

5.2.1 Material synthesis

The first step of material synthesis is to obtain the graphene oxide with a modified Hummers' method. In a typical synthesis process of graphene oxide, graphite powder (0.2g) is first washed with acetone in an ultrasonic bath then filtered and dried under ambient conditions. The washed graphite powder is then soaked in concentrated sulfuric acid (5ml) together with sodium nitrate ($NaNO_3$, 0.05g) and left under mild stirring for at least one hour. Potassium permanganate ($KMnO_4$, 0.6g) is then added in several small batches at 2 minutes intervals into the mixture with the reaction apparatus being placed in an ice-water bath to prevent rapid temperature increase caused by the exothermal reactions. After the addition of $KMnO_4$, the mixture is left under vigorous stirring for 12 hours or until the thickened solution shows a dark brown color. The as-prepared thickened solution is further diluted with distilled water (500ml) in an ice-water bath. Hydrogen peroxide solution (H_2O_2, 2ml, 30% wt.) is then added in the diluted solution drop-wise whereupon the solution turns a light yellow color. The resultant GO suspension is mixed with hydrochloric acid (10%v/v, 50ml) to neutralize the excessive hydrogen peroxide. The obtained GO solution is then transferred into an ion semipermeable membrane tube. The sealed tube with GO solution inside is immersed under deionized water for 4 rounds with each round last for 24 hours, during which the deionized water is replaced to remove as many ion impurities as possible. The obtained high purity GO solution is then washed with distilled water via centrifuge until its PH value reaches 7, then dispersed in 200 ml distilled water with an ultrasound bath.

The Sb-CF/RGO composite is prepared by stacking of electrospun antimony-PAN fibers and electrosprayed GO/PVP layer by layer followed by thermal decomposition and reduction. During a typical material preparation process, the GO is first dispersed in ethanol solution (volume ratio of ethanol/water = 1:1) to form a 1g/L concentration GO/ethanol solution. The solution is then immersed in an ultrasound bath for 10 hours to achieve homogeneous dispersion of GO flakes. Polyvinylpyrrolidone (PVP, 0.05 g, Sigma-Aldrich) is then added to 5 mL GO/ethanol solution (0.5 mg GO) to form GO/PVP in ethanol solution as the precursor for the electrospray process. For electrospinning precursor solution, antimony trichloride ($SbCl_3$, 0.46g, Sigma-Aldrich) is first dissolved in N, N-dimethylformamide (DMF, 10 mL, Sigma-Aldrich) to form a $SbCl_3$ in DMF solution. Polyacrylonitrile (PAN, 0.8 g, Sigma-Aldrich) is added in the solution under vigorous stirring. The stirring is kept at 60°C for 12 hours to ensure the complete dissolution of PAN. The obtained transparent polymeric solution is used as the precursor solution for electrospun Sb-PAN fibers. In a typical composite material fabrication process, 1.5ml $SbCl_3$/PAN in DMF solution is loaded into a 10 mL plastic syringe with a stainless steel voltage receiver, and the syringe is secured to the syringe pump. A piece of aluminum foil attached to a rotating stainless steel drum (grounded) is used as collector. The distance between the needle tip and the collector is kept at 15 cm. The applied voltage is set to 18 kV for the optimal electrospinning condition. During the electrospinning process, the $SbCl_3$/PAN in DMF solution is injected through a blunt-tip syringe needle (22 gauge) at a fixed flow rate of 0.75 mL/hour. After the first electrospinning process, the $SbCl_3$/PAN fibers forms white fibrous mats on the surface of the collector. Then, a thin layer of GO/PVP mixture is deposited on top of the $SbCl_3$/PAN fibrous mat using an electrospray method. GO/PVP ethanol solution (1.0 mL) is injected through a blunt-tip syringe needle (gauge 25) at a flow rate of 0.5 mL/hour. The applied voltage and working distance were 8 kV and 15 cm, respectively. After the deposition of the GO/PVP layer, another layer of $SbCl_3$/PAN fibers is further covered on top of the fibrous mats with a repeated electrospinning process. The final fibrous mat is composed of multi-layered polymer fibers after five rounds of the electrospinning process with four rounds of electrospray process in-between. The obtained fibrous mat is vacuum dried at 80°C for 12 hours and then kept under 2 MPa pressure for 1 minute to ensure the compact stacking of the $SbCl_3$/PAN fibers and the GO/PVP layer. The final fibrous Sb-CF/RGO composite is obtained by heating the material in air at 280°C for 2 hours, and then heated at 600°C for 3 hours in argon balanced hydrogen gas (volume ratio of H_2/Ar = 1:19). The temperature increasing rate was limited to 2°C/min for both processes to ensure the integrity of the carbonized polymer fibers.

5.2.2 Material characterization

The synthesized Sb-CF/RGO composite materials were first characterized with a powder X-ray diffraction technique to confirm the embedding of metallic antimony inside the composites. The tests were performed in an X-ray diffractometer (Siemens D5000) equipped with a Cu-Kα radiation source at a scan rate of 1° per minute. The morphology and microstructure of the carbon fibers, graphene oxide and two composites were characterized using scanning electron microscopy (Zeiss Supra) and transmission electron microscopy (JEOL JEM-2011). Raman spectra of Sb-CF and Sb-

CF/RGO composites were recorded using a Nishaw Raman system equipped with a 633 nm He–Ne laser in backscattering geometry. Thermal gravimetric (TG) analysis was performed to determine the weight ratios of antimony in the synthesized composites through the analysis of their thermal decomposition behavior. The parameters of TG were from 30°C to 650°C with a heating rate of 5°C per minute in an ambient atmosphere.

5.2.4 Electrochemical characterization

The as prepared Sb-CF/RGO composites were tested versus lithium and sodium by assembling half-cells. Type 2032 coin cells were assembled with Sb-CF/RGO composites as working electrodes and lithium (sodium) foil as counter electrodes. The Sb-CF/RGO composite after calcination were cut into 16 cm diameter disks and used directly as working electrodes. The use of binder or conductive additives is unnecessary owing to the free-standing structural characteristics of carbon fiber electrode. The Celgard polypropylene membranes and 1M $LiPF_6$ in 1:1 (v/v) ethylene carbonate (EC) and diethyl carbonate (DEC) without electrolyte additive are selected as the separator and electrolyte for lithium cells, respectively. For sodium cells, round shape glass fiber membranes with a typical diameter of 18 mm were used as the separator. The electrolyte injected into sodium half-cells was 1M $NaClO_4$ dissolved in EC/DMC (1:1 in volume ratio) mixed solvent with addition of 2 % FEC. $NaClO_4$ and $NaPF_6$ are both mainstream salts in the research on sodium-ion battery chemistry, but the $NaClO_4$ was selected for this experiment due to the poor stability of Na_xC_6 towards $NaPF_6$.[256] Considering the main phase of PAN-derived carbon fiber is amorphous carbon, extra SEI formation additive is also needed in order to achieve good coulombic efficiency as well as the cycleability in sodium half-cells. By far, FEC is the most efficient electrolyte additive for stabilizing the SEI in sodium cells, even though it may trigger the formation of a more resistive SEI on carbonaceous anode.[257,258]

The cyclic voltammetry with assembled lithium and sodium cells were conducted between 0.01 V and 2.0 V (or 2.5 V) at a scanning speed of 1mV/s. The charge-discharge cycling performance in lithium and sodium cells was examined with Galvanostatic cycling tests in the potential range between 0.01 V and 2.0 V. Electrochemical impedance spectroscopy (EIS) measurements were performed after the cells have been charged and discharged for desired cycles. The Nyquist plots were recorded by applying an AC voltage of 5 mV amplitude in the frequency range from 0.01 Hz to 100 kHz with cells at their charged states.

5.3 Results and discussion

5.3.1 X-ray diffraction

The XRD patterns of the Sb-CF/RGO composites after thermal reduction and high temperature calcination are shown in Figure 5.1. The Sb-CF/RGO composites were examined with powder XRD to investigate their crystal nature. The XRD tests were conducted within 2theta range between 20° and 70°. The diffraction peaks of the Sb-CF/RGO sample after thermal reduction in hydrogen atmosphere can be indexed to crystalline antimony (JCPDS card No. 05-0562) with minimal impurities, suggesting a complete reduction of antimony salt during high temperature reducing process. For the sample after thermal pyrolysis in air, the peaks are in good agreement with orthorhombic antimony dioxide (SbO_2, JCPDS card no. 11-0694), the confirmation of fully oxidized product of Sb-CF/RGO composite is critical to calculate the weight ratio of antimony content. The results of XRD analysis were used as the reference to calculate the weight ratio of antimony in the composite after thermogravimetric analysis.

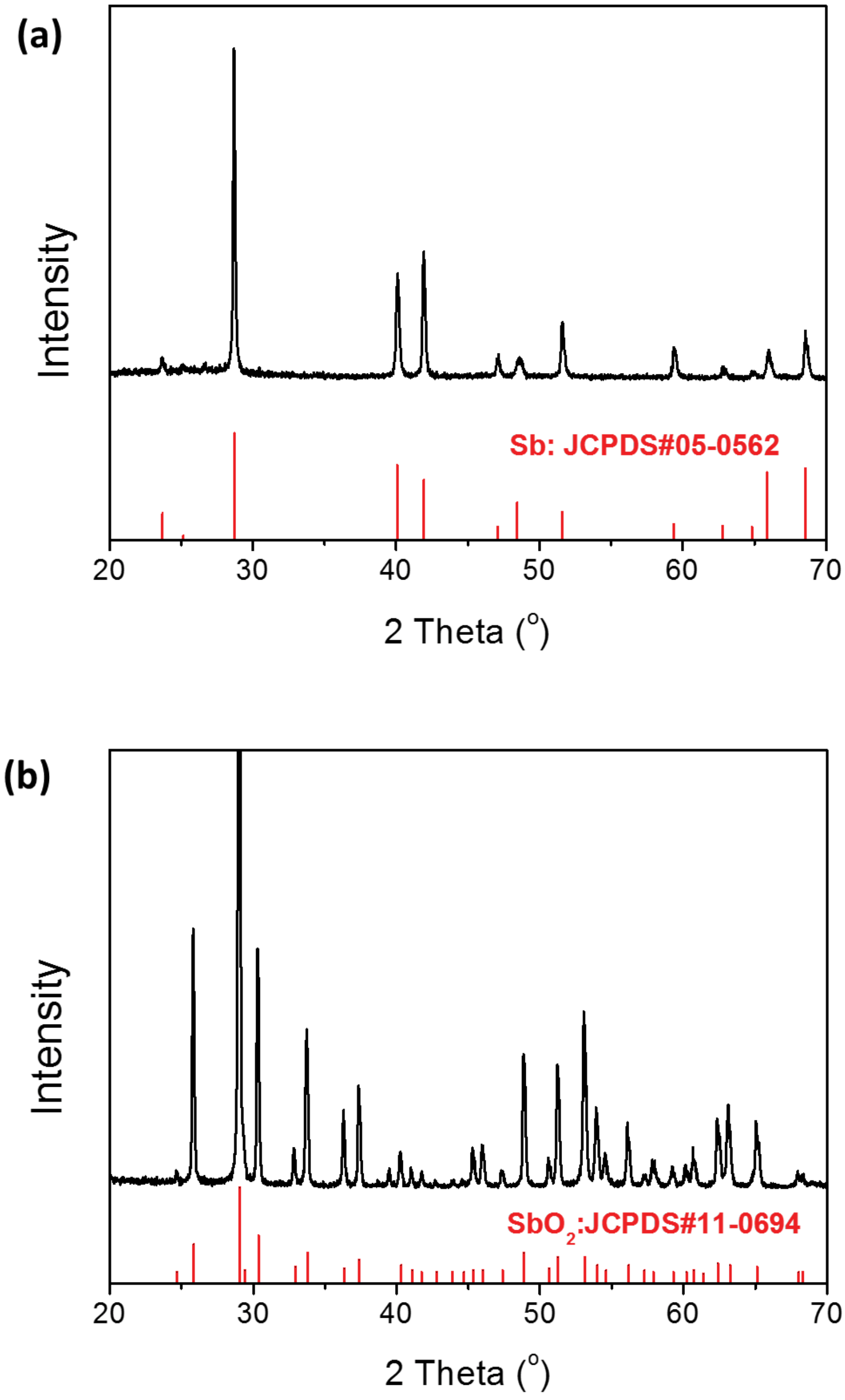

Figure 5.1 XRD patterns of Sb-CF/RGO composite after hydrogen reduction at 600°C and pyrolysis in air at 600°C.

5.3.2 Thermogravimetric analysis

Figure 5.2a shows the thermogravimetric curve along with the DTA curve of Sb-CF/RGO composite between 20°C and 620°C in air atmosphere. The weight loss curve can be divided into three regions, approximately 7.63% weight loss firstly occurs from 20°C to 110°C, which corresponds to the loss of surface water molecules. The weight loss in the second region between 100°C and 550°C is due to the burn off of carbon content in the composite sample, which is partially evidenced by the exothermic peak observed in the DTA curve. The second region corresponds to about 73.3% weight loss of the sample. In the third region, the TG curve becomes flattened, indicating the complete of oxidation and removal of all organic content in the composite. Thereafter, the weight of sample remains unchanged with temperature increase.

The weight loss of sample during heating process was 80.97% with no obvious weight increase at the final stage, indicating that the oxidation of antimony particles occurred simultaneously while the carbon content was burned out. The weight of Sb residual (SbO_2) is used to calculate the weight ratio of antimony in the composite as implied in equation 5-1, and the calculated weight ratio of antimony in Sb-CF/RGO composite is ca. 15.07%.

$$\mathrm{Sb(wt\%)} = \left(\frac{Sb_{\,molecular\ weight}}{Sb_2O_{4\,molecular\ weight}}\right) \times \left(\frac{weight\ of Sb_2O_4\ at\ 600°C}{weight\ of\ sample\ at\ 20°C}\right) \times 100\% \qquad 5\text{-}1$$

5.3.3 Raman spectroscopy

In general, the increase in relative intensity of the D band of a Raman spectrum of carbonaceous material indicates more non-stoichiometric defects in the sample, while an increase in the G band relative intensity implies the increase of conductivity due to more ordered carbon links composed of sp^2 carbon. In the Raman spectra of bare Sb-CF and Sb-CF/RGO composite (Figure 5.2b). The D and G bands are observed for the Sb-C

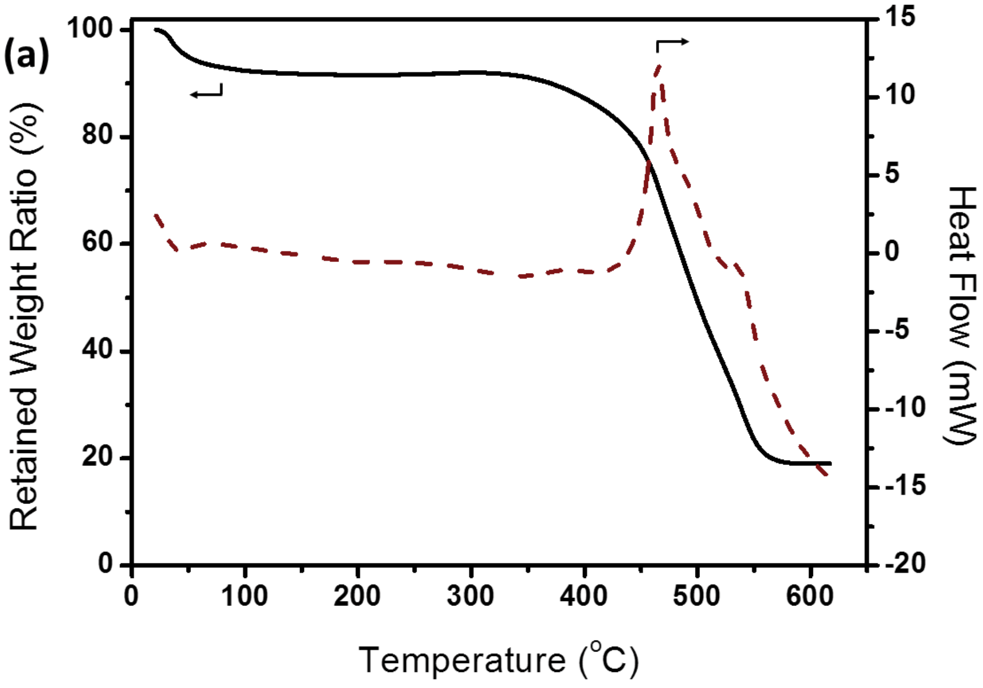

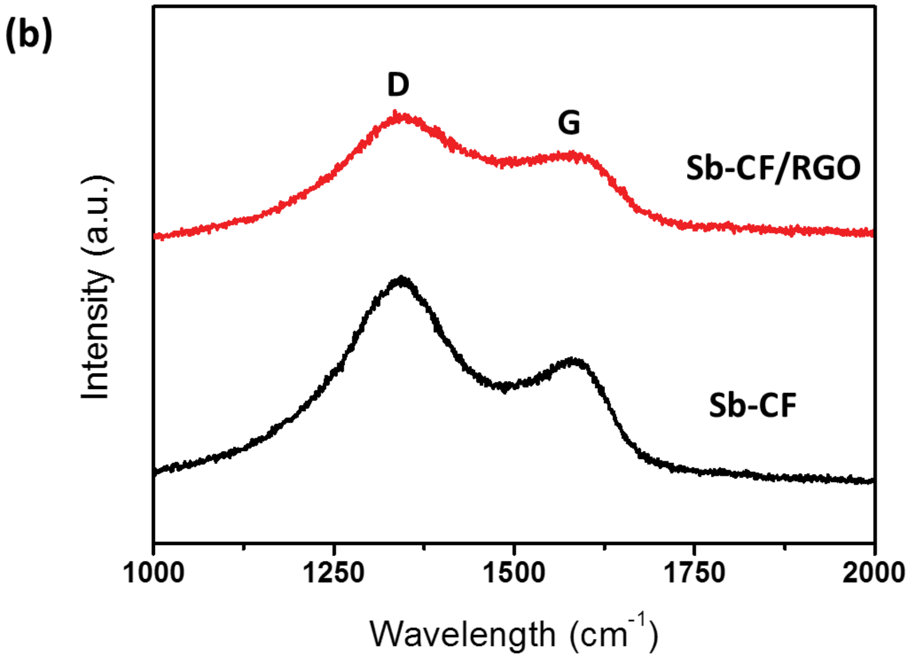

Figure 5.2 Thermogravimetric curve and Raman spectra of Sb-CF/RGO composite. (a) Thermogravimetric curve of Sb-CF/RGO composite between 20°C and 620°C with a ramp rate at 5°C/min in 25 μL/min air flow, and (b) Raman spectra of antimony-carbon fiber (Sb-CF) and Sb-CF/RGO composites.

F and Sb-CF/RGO sample at 1328 cm^{-1}, 1596 cm^{-1} and 1334 cm^{-1}, 1594 cm^{-1}, respectively. The I_D/I_G ratio of Sb-CF and Sb-CF/RGO are 1.2 and 1.07, respectively. The higher intensity of D band in Raman spectra of bare Sb-CF samples suggests that there are more non-stoichiometric defects in the sample, which are formed during the pyrolysis process of PAN. The slight decrease in I_D/I_G ratio of Sb-CF/RGO samples indicates more sp^2 carbon in the Sb-CF/RGO composite compared with the sample prior to thermal reduction, which can be seen as an improvement in terms of electrical conductivity.

5.3.4 Morphological features of Sb-CF/RGO composite

Figure 5.3 a, b show the SEM image of carbonized Sb-PAN nanofibers after 600°C calcination in hydrogen atmosphere, which reveals that the electrospun fiber has a uniform structure with a typical diameter of ca. 250 nm. After the addition of graphene oxide, the obtained antimony-carbon-graphene (Sb-CF/RGO) composite under SEM exhibit a fiber-flake entanglement layout in which the graphene flakes is trapped among carbon fibers, as shown in Figure 5.3c. The GO/PVP layer structure is not shown in the SEM image. It is believed that the disappearance of PVP molecules is due to its relatively low melting point. In the first thermal pyrolysis/stabilization process at 280°C, the GO/PVP layer decomposed while the graphene-oxide flakes were left inside the composite. Figure 5.3 d, e show the TEM image of a single fiber after thermal reduction that contains nanosized antimony particles along the axial direction of carbon fiber, with the size of nanoparticles ranging from 30 nm to 50 nm. Figure 5.3 f shows the morphology of Sb-CF/RGO sample after the thermogravimetric analysis from room temperature to 620°C in air, the residual is mainly composed of antimony oxide particles.

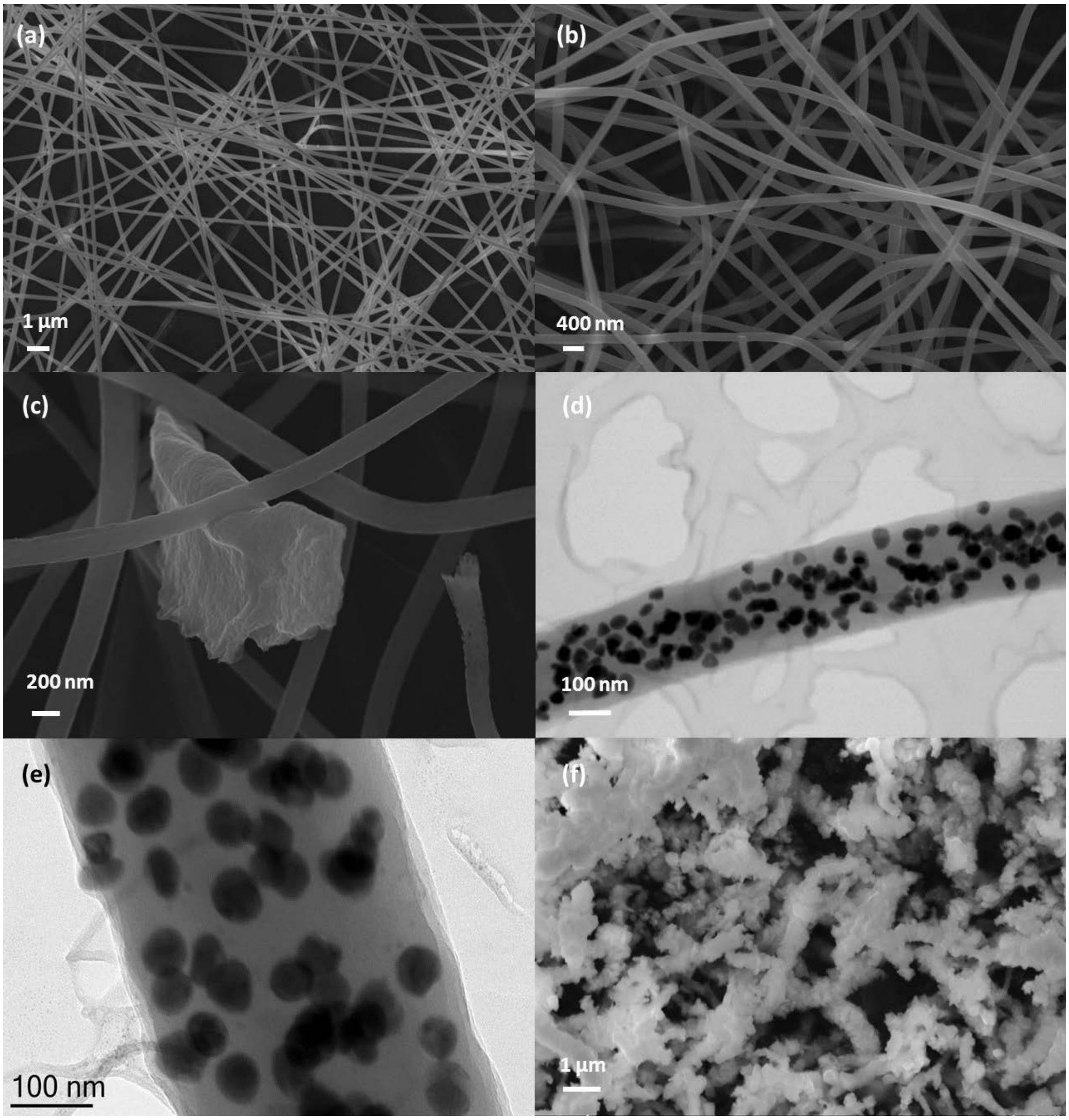

Figure 5.3 SEM and TEM images of Sb-CF/RGO composite. (a) , (b) antimony-carbon fibers at low and high magnifications under SEM, (c) a graphene flake entangled with antimony-carbon fibers under SEM, (d) , (e) TEM images of antimony particles embedded in PAN-derived carbon fibers, and (f) SEM images of Sb-CF/RGO sample after thermogravimetric analysis.

5.3.5 Electrochemical characteristics in lithium half-cells

Figure 5.4a shows the cyclic voltammograms (CV) of the lithium cell with Sb-CF/RGO composite electrode. During the first negative scan, a strong irreversible peak occurred at 0.20 V. This peak is attributed to irreversible decomposition of the electrolyte, forming a solid-electrolyte interphase (SEI) film on the surface of the Sb particles, carbon fibers and graphene flakes. The small peak near 0.01 V is attributed the lithium insertion into carbon. During the reverse positive scan, one overlapped oxidative peak is observed at 0.78 V. In the subsequent negative scans, two reductive peaks positioned at 0.65 and 0.30 V are observed, which can be assigned to the Li–Sb alloying reactions (as shown in equation 5-2, 5-3)[251]. In the subsequent positive scans, the overlapped oxidative peaks slightly shift from 0.78 V to higher potentials, corresponding to Sb–Li dealloying reactions. The CV results show that the alloying and dealloying reactions between lithium and antimony can occur in a reversible manner inside the composite electrode.

$$2Li^{+} + Sb \xrightarrow[alloy\rightarrow]{\leftarrow dealloy} Li_2Sb \tag{5-2}$$

$$Li^{+} + Li_2Sb \xrightarrow[alloy\rightarrow]{\leftarrow dealloy} Li_3Sb \tag{5-3}$$

Figure 5.4b shows the typical charge-discharge voltage profiles Sb-CF/RGO electrode versus lithium between 0.01 v and 2.0 V at a constant current density of 100 mA/g. The voltage curves show mainly two plateaus during charge and discharge process. The plateaus in the higher potential region (around 0.65 V at discharge and 0.82 V at charge) are attributed to the Li alloying–dealloying reactions to produce Li_2Sb and Sb phases. The plateaus in the lower potential range (0.5V at discharge and 0.78 V at charge) are attributed to the Li alloying–dealloying reactions to produce Li_3Sb and Li_2Sb phases. Therefore, most of the capacities come from the alloy and de-alloy reactions. The initial discharge exhibited an overall capacity of 533 mAh/g, and a reversible capacity of 498 mAh/g was recovered during the first charge process, leaving an initial coulombic efficiency of 67.2% (as shown in Figure 5.4c). However, the coulombic efficiency quickly increased to 91.08 in the second charge-discharge cycle, suggesting a good passivation on the electrode surface during the initial cycle. When the lithium cell was cycled at a lower current density of 50 mA/g, the initial reversible capacity and coulombic efficiency of Sb-CF/RGO electrode were 562 mAh/g and 64.9%.

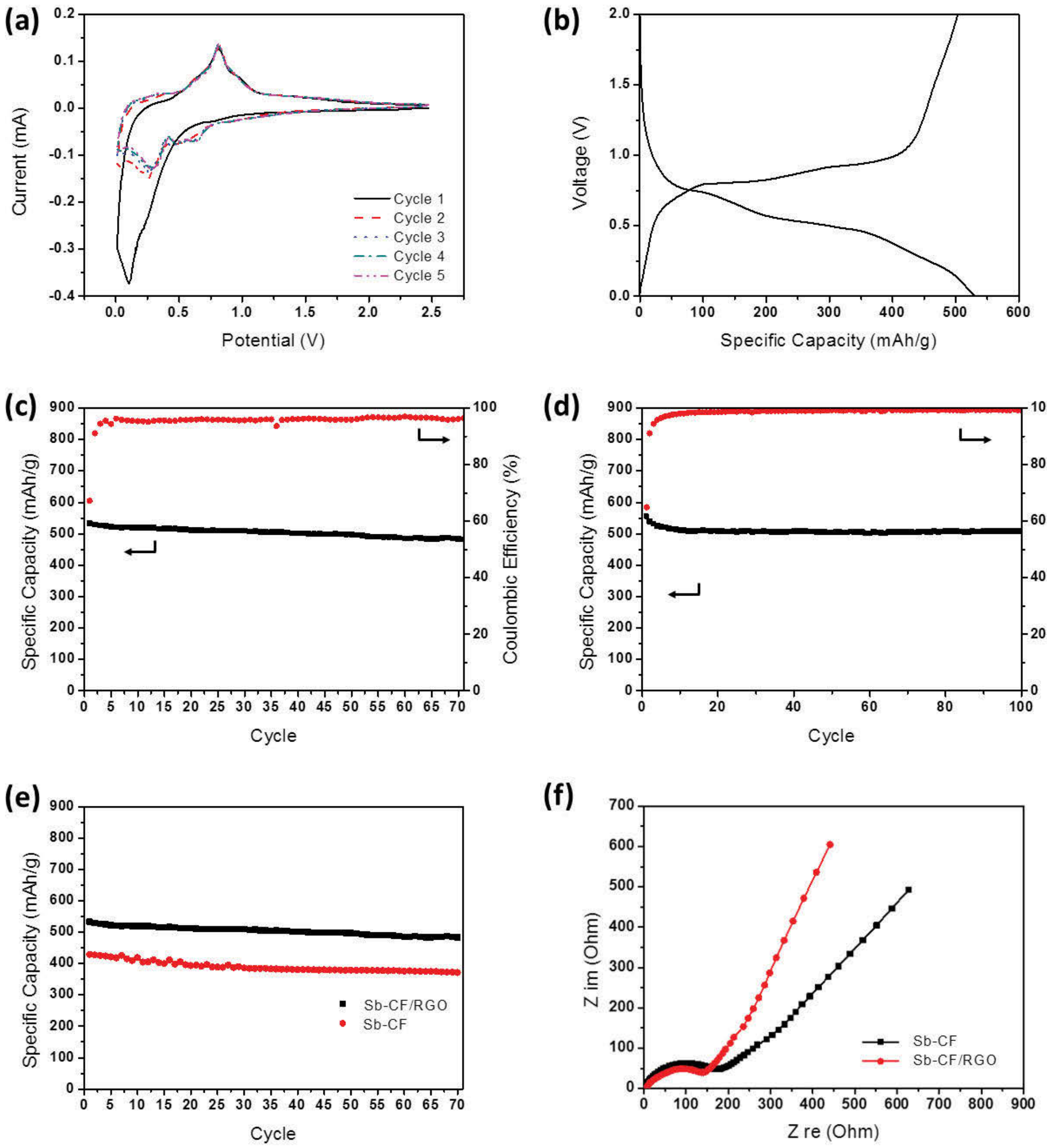

Figure 5.4 Electrochemical characterization results for lithium cells. (a) Cyclic voltammograms of a lithium half-cell with a Sb-CF/RGO electrode at 1 mV/s scan rate between 0.01 V and 2.5 V, (b) voltage profiles of a lithium cell with Sb-CF/RGO electrode at a current density of 100 mA/g, (c), (d) cycling performance of a lithium cell with Sb-CF/RGO electrode at a current density of 100 mA/g and 50 mA/g, respectively, (e) reversible capacities of lithium cells with Sb-CF/RGO electrode and Sb-CF electrode at the current density of 100 mA/g, respectively, (f) Nyquist plots obtained from electrochemical impedance measurements lithium cells Sb-CF/RGO and Sb-CF electrode after 20 charge-discharge cycles.

As shown in Figure 5.4d, the reversible capacity and coulombic efficiency both increased with reduced charge-discharge currents. In addition, the Sb-CF/RGO electrode clearly showed better performance in terms of reversible capacities and impedance compared with Sb-CF electrode (Figure 5.4 e and f). The Nyquist plots from EIS measurements after 10 complete cycles are displayed in Figure 5.4f. Both Nyquist plots present a compressed semicircle in through the high-moderate frequency region and a straight line in low frequency region, which can be attributed to charge transfer process and diffusion process, respectively. The lower charge transfer resistance of Sb-CF/RGO electrode compared with that of Sb-CF electrode indicates the improvement in conductivity after the addition of graphene.

5.3.6 Electrochemical characteristics in sodium half-cells

Figure 5.5a shows the cyclic voltammograms of a Sb-CF/RGO composite electrode at a scan rate of 0.1 mV/s in the potential window between 0.01 V and 2.0 V versus sodium. During the initial scan, a major reductive peak at around 0.2 V is observed in the first sodiation process, the disappearance of this peak in the following scans suggests that it is mainly attributed to electrolyte passivation and solid-electrolyte interphase formation on Sb-CF/RGO composite electrode surface in the initial sodiation process. The small peak near 0.01 V implies the sodium ion insertion into carbonaceous materials. In the second cathodic scan, the broad current peak from 0.62 V to 0.26 V is attributed to the formation of Na_3Sb through a series amorphous Na_xSb phase (as shown in equation 5-4).[251] The anodic scans show broad current peaks at around 0.8 V without obvious intensity change or current peak shifting during the initial cycles, indicating a highly reversible alloy/de-alloy reaction between of antimony and sodium. The negligible shape changes of redox current peaks from the second to subsequent cycles indicate a stable electrochemical reactivity of the as-prepared antimony-carbon-graphene composite anode.

$$\boldsymbol{x}\mathrm{Na} + \mathrm{Sb}\ \frac{\leftarrow dealloy}{alloy\rightarrow}\ \mathrm{Na}_{\boldsymbol{x}}\mathrm{Sb}\ (0 < \boldsymbol{x} \leq 3), \tag{5-4}$$

As shown in Figure 5.5b, the galvanostatic profile of the Sb-CF/RGO composite electrodes was obtained at a current density of 100 mA/g within a voltage window between 0.01 V and 2.00 V. The long sloping plateau starting from 0.8 V can be observed during the initial discharge process, which is suspected to be related to the formation of SEI films on the electrode surface. However, the voltage plateaus corresponds to the multi-step alloy reactions between Sb and Na into hexagonal Na_3Sb through amorphous Na_xSb can hardly be identified during the initial discharge voltage curve. The following charge curve has reverse sloping plateaus from 0.30 V to 0.75 V. The very narrow plateau at about 0.75 V during the charge process is mainly associated with the phase transition from the Na_xSb alloy back to Sb. This observation is in good agreement with the cyclic voltammetry results. The initial discharge process delivered a specific capacity of 892 mAh/g, but the specific capacity extracted from the electrode in the following charge process was only 346 mAh/g, giving a coulombic efficiency as low as 38.78% for the initial cycle. The irreversible capacity loss in the first cycle is a common phenomenon for negative electrode materials containing large portions of non-graphitic carbon due to the irreversible insertion of metal ions into pores and vacancies. The Sb-CF/RGO composite materials with large volume expansion during the alloy reactions also have the tendency to consume more electrolyte species during the SEI formation process at more exposed sites, therefore exhibiting severe irreversible capacity loss and even lower coulombic efficiencies compared to pristine carbon fiber electrode (see Chapter 4) during the initial cycle.

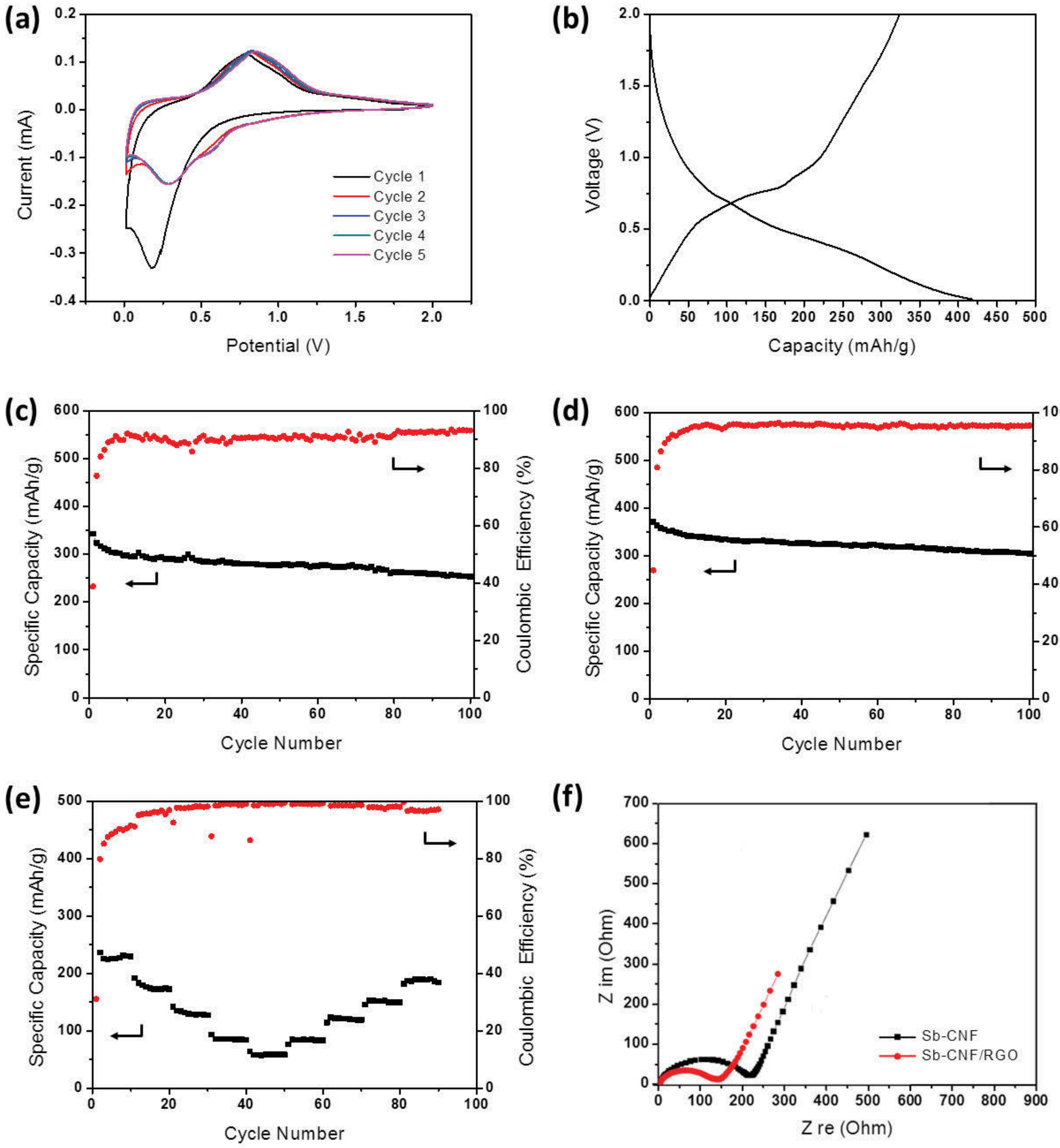

Figure 5.5 Electrochemical characterization results for sodium cells. (a) Cyclic voltammograms of a sodium half-cell with a Sb-CF/RGO electrode at 1 mV/s scan rate between 0.01 V and 2.0 V, (b) voltage profiles of a sodium cell with Sb-CF/RGO electrode at a current density of 100 mA/g, (c), (d) cycling performance of a sodium cell with Sb-CF/RGO electrode at a current density of 100 mA/g and 50 mA/g, respectively, (e) cycling performance of a sodium cell with Sb-CF/RGO electrode at current varied densities of 200 mA/g, 400 mA/g, 600 mA/g, 800 mA/g and 1000 mA/g. (f) Nyquist plots obtained from electrochemical impedance measurements on sodium cells with Sb-CF/RGO and Sb-CF electrodes after 20 charge-discharge cycles.

After 100 cycle, the reversible capacity of the Sb-CF/RGO composite dropped to 274 mAh/g after 100 cycles, corresponding to ca. 20% capacity loss. As previously demonstrated, the galvanostatic cycle performance can be improved by reducing the charge-discharge current rates. As shown in Figure 5.5d, under a current rate of 50 mA/g, the Sb-CF/RGO electrode in the sodium cell present a higher reversible capacity of 371 mAh/g during the first cycle, and the reversible capacity after 100 cycles is 303 mAh/g, corresponding to ca. 18% capacity loss after 100 cycle. In addition, a slight improvement in coulombic efficiency can also be confirmed at a reduced current rate of 50 mA/g. The rate capability of Sb-CF/RGO electrode was examined by cycle tests ar various currents at 200 ~ 1000 mA/g, and results are as shown in Figure 5.5e. When the sodium cells are cycled at much higher current densities, the charge/discharge specific capacities of Sb-CF/RGO composite electrodes decrease dramatically compared to that under 100 mA/g current or 50 mA/g current. However, the sodium cell showed good tolerance to large current charge-discharge as the capacity can be restored after the current rate decreases. The EIS measurement results of Sb-CF and Sb-CF/RGO composite electrodes in sodium cells after 10 charge-discharge cycles are as shown in Figure 5.5f. Both Nyquist plots present a semicircle (high to medium frequency region) and a straight line (low frequency region). As shown in the figure, the Nyquist plot of Sb-CF/RGO composite electrode shows smaller semicircle across the Z_{re} axis, corresponding to a lower charge transfer resistance than Sb-C electrode, which is in good accordance with the EIS results from lithium cells.

The galvanostatic charge/discharge cycling test results of the Sb-CF/RGO composite are consistent with the obtained CV redox peaks. In addition, both CV and charge-discharge cycling tests confirm that the electrochemical reactions between antimony and sodium are the main reactions that dominating the charge storage capability of the Sb-CF/RGO composite electrode. Despite the Sb-CF/RGO electrode exhibiting a relatively high specific capacity over graphite anode as well as good tolerance of high rate charge-discharge, it should be emphasized that the coulombic efficiency of tested electrodes all remain below 98% during the galvanostatic cycling tests, which is far from satisfactory for secondary batteries. This inadequate coulombic efficiency implies an unstable passivation layer on electrode surfaces and continuous breakdown and regrowth of electrode/electrolyte interphases accompanied by the irreversible reactions of electrolyte species upon charge/discharge processes. The common measure to address this problem is using a suitable electrolyte which contains a component that can effectively perform a stable passivation in the initial charge process.

The cycling performance and abuse tolerance of Sb-CF/RGO composite electrode is a reflection of its structural characteristics. The nanosized antimony particles are located inside the carbon fibers along the axial directions via the utilization of the electrospinning technique. This unique structure offers good electronic conductivity with carbon fibers and extra RGO flakes as conducting additives, while the short diffusion lengths from the surface of carbon fibers to embedded antimony particles also ensure good ion conductivity. In addition, the carbon fibers act as stress buffers to accommodate the volume change of embedded metal particles during the alloy/de-alloy reactions of the Na-Sb couple. All of these structural features in Sb-CF/RGO composite electrodes form the fundamental advancement as negative electrode which results in the good electrochemical performance in sodium half-cells. Nevertheless, the drawbacks of Sb-CF/RGO composite electrode are also obvious and difficult to deal with. The large surface area of Sb-CF/RGO composites causes severe irreversible capacities associated with sodium ion consumption during the initial discharge process and subsequential cycles. As a result, its average coulombic efficiency is far from satisfactory for the implementation in practical sodium secondary batteries.

5.4 Conclusion

The work presented in this chapter is an investigation of the electrochemical performance of antimony-embedded carbon fiber/reduced graphene oxide (Sb-CF/RGO) composites as an alloy type negative electrode material for lithium and sodium secondary batteries. This composite is capable of delivering high reversible capacities of 562 mAh/g and 371 mAh/g at 50 mA/g current versus lithium and sodium, respectively. The electrode also good capacity retention in a mild charge/discharge regime (50 ~ 100 mA/g) in both lithium and sodium half-cells. The utilization of a small quantity of RGO in the composite offers a few advantages including enhanced structural stability as well as good electrical contact of the antimony upon repeated alloy/de-alloy processes of antimony with lithium and sodium ions. Due to the conductive network consist of carbon fibers and graphene nanosheets, the Sb-CF/RGO electrodes displayed good rate capability at various current rates up to 1000 mA/g in sodium cells. Therefore, this electrode materials may be used in rechargeable lithium and sodium batteries for high power applications. However, the high initial irreversible capacities and low coulombic efficiencies during charge-discharge cycling of this composite electrode material also imply difficult technical challenges remain before its implementation in practical lithium-ion or sodium-ion batteries.

Chapter 6 Application of porous carbon sheet in lithium-sulfur battery

6.1 Introduction

Lithium-sulfur (Li-S) battery technology is considered as one possible route towards next generation lithium based battery systems, which has potential to deliver a much higher specific (gravimetric) energy at a relatively lower cost.[259,260] Although the Li-S battery has attracted many research efforts during the last few decades, its development still suffers from practical issues such as low attainable energy, poor cycle stability, etc. all of which leads to the performance of demonstrated Li-S batteries inferior to that of state of art Li-ion batteries.[261]

The conceptual Li-S battery is a liquid phase energy storage system since the dissolution of sulfur and formation of polysulfide in organic electrolyte solvents are essential for the operation of Li-S cells, with the soluble polysulfide species as the major phases that react with lithium ions. On the other hand, the dissolution of polysulfide also leads to the shuttle mechanism of polysulfide anions between anode and cathode, which further causes self-discharge behavior and the poor cycling efficiency of Li-S batteries.[260] The Li-S batteries often suffer from rapid capacity fading, which is originated from cell compartmentalization including the lithium anode, sulfur cathode and liquid electrolyte. The lithium has been known for long time as an anode material with limited cycling efficiency, and the electrical insulating nature of sulfur and the tendency of sulfur to dissolve in organic electrolyte have been recognized as the main reason for low sulfur utilization. The reaction of electrolyte components with lithium anode and polysulfide species results in electrolyte depletion, which further reduces the capacity upon repeated cycling. These issues are not new to the battery research community as the concept has been pursued for decades.[262] To constrain the solubility of polysulfides, confinement aiming to trap sulfur within the cathode have been pursued, but so far little success has been achieved. The poor performance of Li-S cells is mainly attributed to the dissolution of polysulfide species (Li_2S_n, $3 \leq n \leq 8$), which is also essential for the successful operation of Li/S redox reactions. The reduction reaction of non-conductive sulfur in contact with lithium ions can only proceed with the help of conductive agent such as conductive carbon, and conductive polymer.[172] The sustainability of the reactions between polysulfide and lithium ions is highly dependent on the absorption/adsorption ability of conductive architecture in the cathode. However, the physical absorption and chemical adsorption of most known porous compound is not very strong, therefore a large quantity of conductive media is required in sulfur composite cathodes in order to maintain a good cyclability of Li-S cells. As a result, the weight ratio of sulfur and area sulfur loading in cathodes are usually very low which leads to limited capacity and power capability from Li-S cells.[263,264] Further increase of sulfur content in cathodes inevitably results in lower sulfur utilization rates, a high concentration of polysulfide species and subsequential formation of insulating Li_2S_2 and Li_2S phases on cathode surface, which causes fast performance deterioration of Li-S cells.[265,266] The optimized high electrolyte volume to sulfur in cathode ratio is effective to reduce the concentration of polysulfide in electrolyte and promote the cycleability of Li-S cells. Therefore high loads of electrolyte must be coupled with high sulfur loading cathodes to maintain the cycle life of Li-S cells, but the excess electrolyte also has drawbacks as it reduces the volumetric energy density of batteries considerably.[137] Most of the studies have been devoted to the optimization in sulfur cathode architectures with well-designed porous host structures to retain the sulfur and subsequently, the polysulfide species. Different synthesis approaches has been demonstrated with carbonaceous materials, metal oxide, MOFs and intermetallic oxides.[267,268] Although these strategies have suppressed the undesirable side reactions of Li-S chemistry, they have not yet revealed any viable approach to a highly reversible reaction route utilizing the Li/S redox couple from the fundamental chemistry level.[269–271] No matter how much efforts was put into this field, the migration of polysulfide is still the critical issue that cannot be overruled with present cell configurations. In this study, a different approach differing from the common confinement strategy is investigated: using chemically synthesized polysulfide solution directly as a liquid state sulfur cathode. The implication from previous reports is that the improvement of Li-S battery performance can be expected by adopting this new design of cell configuration.[178,272]

Mixed ether type solvents are commonly used in electrolyte for Li/S cells due to their good solubility of polysulfides hence and better utilization of sulfur compared with conventional carbonate type solvents used for Li-ion cells. The carbonate solvents are ruled out from potential electrolyte components because of their tendency to react with polysulfide species.[273] $LiSO_3CF_3$ and $LiN(SO_2CF_3)_2$ are lithium salts of choice for the electrolyte of Li-S cells, as they offer good ionic conductivity in conjunction with 1, 3-dioxolane/dimethoxyethane (DOX/DME) or 1, 3-dioxolane/tetraethylene glycol dimethyl ether (DOX/TEGDME) mixed solvents. However, both salts are also known for causing the corrosion of aluminum, the commonly used cathode substrate for lithium batteries.[140]

The semi-liquid Li-S cell configuration uses a metallic lithium anode and dissolved polysulfide solutions as cathode, which is different from common Li-S cells configuration with two solid electrodes. The sulfur cathode in such configurations is in the form of soluble polysulfides trapped in a porous carbon structure. In this way the Li-S cell can avoid the problem of aluminum corrosion from $LiSO_3CF_3$ or $LiN(SO_2CF_3)_2$ salts, thereby achieving enhanced cycleability compared with conventional Li-S cells. The concept of coupling lithium anodes with dissolved sulfur was previously investigated for Li-S primary cells,[259] and now the accumulated knowledge and know-how regarding rechargeable Li-S cells can greatly improve the performance of Li-dissolved polysulfide semi-liquid cells by introducing $LiNO_3$ salts into the electrolyte. Using $LiNO_3$ as electrolyte additive is an effective approach to improve the cycleability of Li-S cells for certain periods, but the small amount of $LiNO_3$ in electrolyte will be eventually consumed. In addition, the semi-liquid cell configuration offers a solvent-rich environment at the cathode end, which is helpful to diminish the negative effects from electrolyte depletion due to the reactions between solvent molecules and polysulfide species. The previous research works, the free standing carbon fiber sheet derived from electrospun PAN fibers has been demonstrated as a binder-free negative electrode in both lithium and sodium secondary batteries (see Chapter 4). The PAN-derived carbon fiber sheets offers good conductivity for electrical reactions, and its light weight, structure flexibility and high porosity characteristics are ideal as the polysulfide solution reservoir in the lithium/dissolved sulfide cell configuration, thereby further investigation on novel Li-S semi-liquid cell configuration is conducted. This research took an alternative path by using liquid phase sulfur cathodes from dissolving stoichiometric amounts of sulfur and Li_2S salt in electrolyte solvents. This approach is shown to result in relatively good performance compared to the common confinement approach. Such a strategy eliminates the detrimental Li_2S deposition on cathode surfaces, which seems beneficial to cell cycling performance.

6.2 Experimental

6.2.1 Material synthesis

All chemicals used in our experiments were purchased from Sigma-Aldrich. Sulfur was vacuum dried at 100°C before transferring into glove-boxes and other chemicals were used as received. The polysulfide solution was prepared by dissolving stoichiometric amount of lithium sulfide (Li_2S) and octasulfur (S_8) (in this specific order) in 1,2-dimethoxyethane ($CH_3SCH_2CH(OCH_3)_2$, DME) and 1,3-dioxolane ($C_3H_6O_2$, DOL) mixed solvents under mechanical stirring for 24 hours at around 50°C, the operation was carried in an argon filled glove-box with both moisture and oxygen level below 1 ppm (part per million). After the complete reaction, the homogeneous polysulfide solution with a dark brown color was obtained (as shown in Figure 6.1). The as-prepared polysulfide solution was keep still for at least 3 days for precipitation check before the cell assembly, and the stable polysulfide solutions will be referred as "catholyte" below. The formula of electrolyte for Li-S cells is 1.0 M lithium triflate (CF_3SO_3Li, LiTf) and 0.1 M concentration lithium nitrate ($LiNO_3$) in DME: DOL mixed solutions as electrolyte additive.

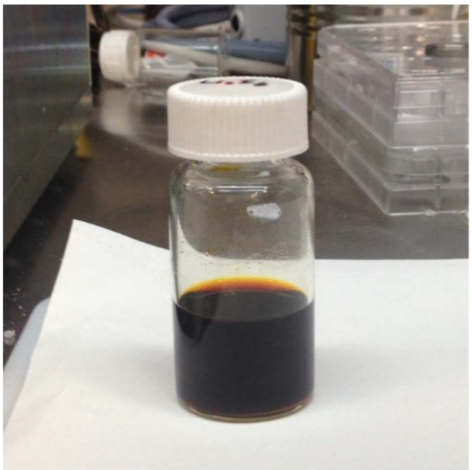

Figure 6.1 The image of catholyte solution. The solution is 0.5 M/L concentration polysulfide (Li_2S_6) in mixed DME/DOL (1:1 by volume) solvents.

The porous carbon sheet was obtained from carbonized electrospun PAN fibrous mat. The precursor for electrospinning was prepared by dissolving polyacrylonitrile (PAN, average molecular weight of 15,000 g/mole) in N, N-dimethylformamide (DMF) with constant stirring at 50 °C to form a homogeneous solution in 10 %wt./v concentration. Before the electrospinning process, the polymer solution was loaded into a 10 mL polycarbonate syringe, a stainless spinneret connected to the high-voltage DC power supply (with the power switched off at this stage) is secured to the syringe. The distance between the tip of spinneret and the grounded sample collector was set at 15 cm. An aluminum foil was used to cover the collector for easy transfer of PAN fibers after the electrospinning process. During electrospinning, the high-voltage DC power supply was switched on to generate a stable 15 kV voltage output, then the PAN in DMF solution was extruded from the spinneret tip at a fixed flow rate of 16.8 µL/min. The long-chain polymer molecules were stretched into one-dimensional fibers and accumulated on the collector surface. After the electrospinning process, the collected PAN fibrous mat was removed from the aluminum foil and dried in vacuum oven at 80°C for 12 hours. The thermal pyrolysis of electrospun PAN fibers was divided into two stages. In the first stage, the dried PAN fibrous mats was place in a tube furnace and stabilized at 280°C in air for 5 hours. In the second stage, the dried PAN fibrous mats underwent a carbonization process via heating to a temperature of 900°C in argon atmosphere for 10 hours. The heating rate was fixed at 2°C/min in order to retain the original structural characteristics of electrospun PAN fibers.

6.2.2 Material characterization

The morphological features of PAN fibers and carbonized PAN fibers were characterized by a scanning electron microscopy (SEM) operating at an acceleration voltage of 5 kV. Raman spectroscopy was used to determine the carbon phases in PAN-derived carbon fibers, with the spectrum collected in backscattering mode under a 532 nm wavelength laser beam. The crystalline structure in the PAN-derived carbon fibers after pyrolysis was further examined with X-ray diffraction (XRD).

6.2.3 Electrochemical characterization

Electrochemical measurements were performed with type CR2032 coin cells comprised of porous carbon fiber sheets and polysulfide solutions as the cathode, lithium metal anode as active materials. Cell assembly was carried out inside an argon-filled glove box, and an accurate amount of liquid electrolyte and catholyte were added using a 100μL Pipette. In general, higher polysulfide concentration in electrolytes is beneficial for improving the cycleability of Li-S cells but it brings in the penalty of the sulfur utilization rate of cathodes during the initial cycles. This study aims for enhanced cycleability of Li-S cells other than high initial capacities of sulfur cathode, therefore low electrolyte to catholyte volume ratio was used.

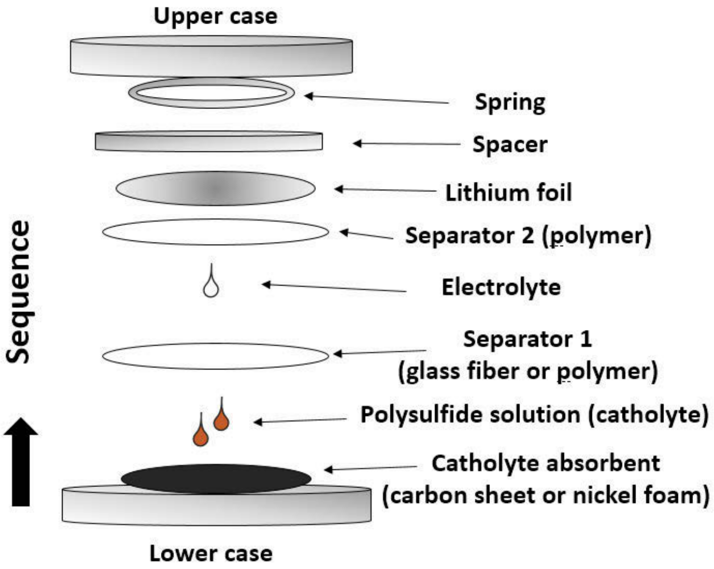

Figure 6.2 Schematic illustration of components in the assembled Li-S coin cells.

The typical cell assembly procedure is described as follows. First, a piece of porous carbon sheet is placed in the lower case of a coin cell, the porous carbon sheet used as the cathode substrate is cut by a round disc punch tool from a flattened carbonized PAN sheet. The carbon sheet cut has a typical diameter of 14 mm and a typical weight of 0.65±0.10mg. 20 μL of catholyte is added on the carbon sheet afterwards. After the addition of catholyte, the carbon sheet is covered by a piece of separator, then the electrolyte is added. The amount of electrolyte is set to 8 μL in cells with a Celgard porous polymer membrane as the primary separator, but increased to 20 μL in cells in the case of glass fiber membranes used as the primary separators. After the addition of electrolyte, another piece of Celgard porous polymer membrane (the secondary separator) is covered on top the first separator. The lithium metal foil is placed on top of the secondary separator and serves as the anode. A stainless steel spacer and a spring is placed on top of the lithium foil to ensure good contact between both electrode and separators in the cell. After all components are placed in the lower cell case, the upper case of the coin cell is added and the cell is manually sealed with a capping machine. The layout of cell components is shown in Figure 6.2.

Cyclic voltammetry (CV) was conducted to collect the information on Li/S redox reactions. The CV scans were carried out in the potential range between 1.75 and 3.0 V, with a scanning rate at 0.1 mV/s. Galvanostatic charge/discharge cycling tests were performed with assembled Li-S coin cells at various current densities in a fixed voltage range from 1.7 V to 2.6 V, which is different from commonly used voltage range between 1.0 V and 3.0 V. The narrowed voltage window was adopted for cycling tests in order to avoid the undesirable side reactions with $LiNO_3$ decomposition and improve the charge efficiency. All current densities and specific capacities are calculated based on the nominal value of Li_2S_6 in assembled cells. The electrochemical impedance spectra of assemble Li-S cells are collected at open circuit voltage (OCV) before and after 10 cycles of charge/discharge cycling tests. The parameters of impedance measurements are frequency range from 0.01 Hz to 100 kHz, at 5 mV voltage amplitude.

6.3 Results and Discussion

6.3.1 Morphology and composition of synthesized material

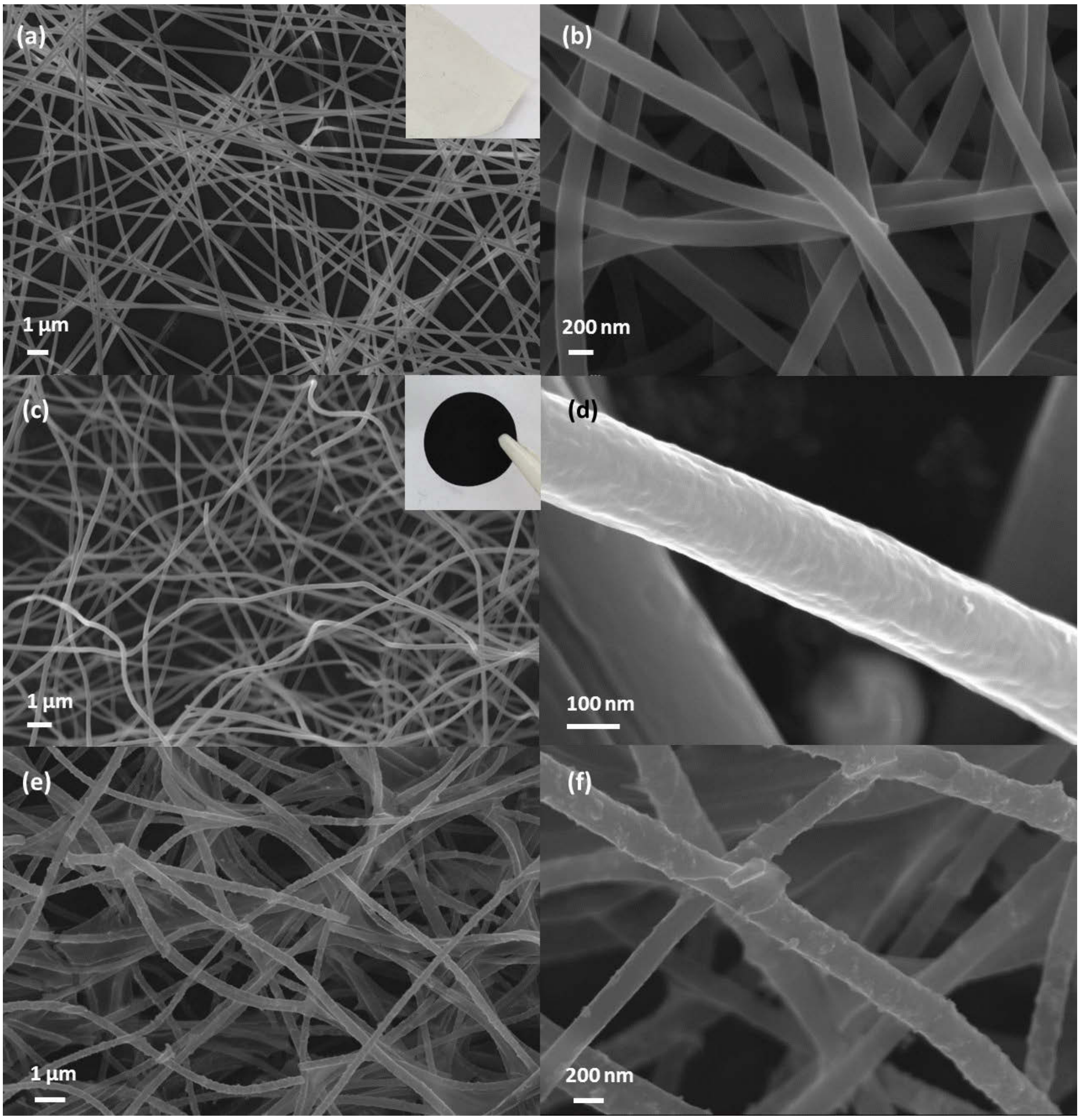

Figure 6.3 SEM images of PAN fibers and carbon fiber electrodes. (a), (b) electrospun PAN fibers and (c), (d) PAN derived carbon fibers after calcination, (e), (f) the carbon fiber electrode retrieved from cycled lithium-sulfur cells after 20 charge-discharge cycles.

Figures 6.3 a, b and 6.3 c, d are SEM images of the electrospun PAN fibers and PAN-derived carbon fibers at 800°C, respectively. The insets in Figures 6.3 a and c are optical images of PAN fibrous membrane and a piece of circular shape carbonized PAN-fiber electrode, respectively. The electrospun PAN fibers have a wide diameter ranging from 220nm to 350 nm, and PAN derived carbon fibers after pyrolysis at 800°C showed smaller diameter values from 200nm to 330nm. The slightly decreased fiber diameter after carbonization is attributed to the decomposition process of PAN and vaporization of nitrogen, oxygen and hydrogen elements during long time pyrolysis. The layout of carbon fibers forms a porous conductive network as the substrate to trap polysulfide solutions.

Figure 6.4a shows the XRD patterns of CFs with a broad peaks around 25 degree (2theta), corresponding to a graphitic crystalline structure. The ratio of sulfur in the cathode needs to be addressed before the evaluation of its effect on the combined performance of Li-S cells. A high load of carbon at the cathode end is beneficial to the electronic percolation in the electrode but it also leads to reduced attainable energy from sulfur redox reactions. Therefore, four polysulfide solutions with different concentration of Li_2S_6, including 0.5 M Li_2S_6, 1.0 M Li_2S_6, 1.5 M Li_2S_6, and 2.0 M Li_2S_6 were prepared in order to determine the optimized sulfur loading rate while minimize the amount of carbon fiber in Li-S cells. However, only the 0.5 M Li_2S_6 in DOX/DME (1:1, v/v) passed the precipitation check after resting for 72 hours, it is suspected that the high solution viscosity associated with high concentration polysulfide hinders the further chemical reaction between sulfur and Li_2S salt, and subsequently, the formation of soluble polysulfide species. Nevertheless, the lower concentration 0.5 M polysulfide solution with lower viscosity is still in favor for further experimental design due to its easy percolation into porous carbon fiber sheets.

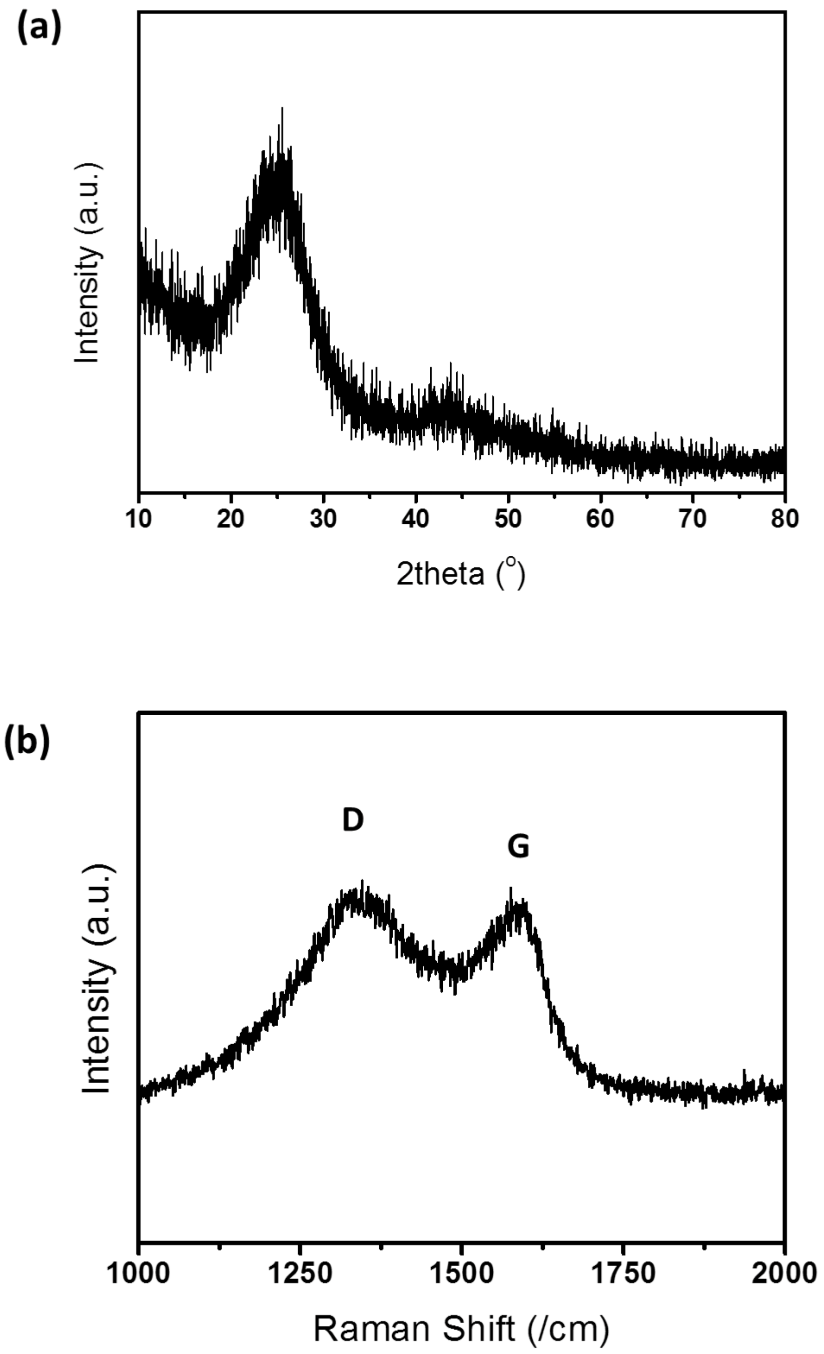

Figure 6.4 (a) XRD pattern and (b) Raman spectrum of PAN derived carbon fibers. The carbon fiber sample was converted at 800°C in argon.

6.3.2 Electrochemical characteristics in lithium sulfur cells

Figure 6.5a shows the cyclic voltammograms collected from a lithium sulfur semi-liquid battery. The initial scan is from the open circuit voltage (OCV) to 1.75 V. During the initial cathodic scan, only one cathodic peak at 1.95 V corresponding to polysulfide reduction, was observed. From the second cycle, two cathodic peaks showed in the CV plot at 2.35 and 1.95 V, corresponding to the reduction process of high order polysulfides (e.g. Li_2S_8, Li_2S_6), respectively. In anodic scan, two overlapping anodic peaks were observed. These two peaks at 2.30 and 2.45 V correspond to the oxidation of Li_2S and low-order polysulfides (e.g. Li_2S_4). The tested battery maintained a stable peak intensity during CV scans, indicating highly reversible cathodic and anodic reactions in the modified battery configuration. As no redox peaks was observed in the voltage range above 2.6 V in CV scans, the voltage windows of following galvanostatic charge-discharge cycling tests were set between 1.75 V and 2.6 V. Figure 6.5b shows the 1st, 21th, 41th, and 61th charge and discharge voltage-capacity profiles, corresponding to current densities of 200mA/g, 500mA/g, 1000mA/g and 200mA/g. The steady voltage plateaus are consistent with redox current peaks in the cyclic voltammograms. The charge voltage plateau following the varied current densities implies an increased level of cell polarization. The semi-liquid cathode exhibited good reversible reactivity with lithium anodes under variable current loads. Figure 6.5c shows the reversible capacity of assembled cells with a constant current of 1A/g. The reversible capacity and coulombic efficiency of the first cycle are 691 mAh/g and 74.9 %, respectively. The capacity and coulombic efficiency gradually increased during the first few cycles. After about 40 cycles, the slight decreases in both capacity and coulombic efficiency with increasing cycle number were observed. The Li-S cell exhibited a high reversible capacity of 1010 mAh/g for more than 120 cycles under 1A/g current density.

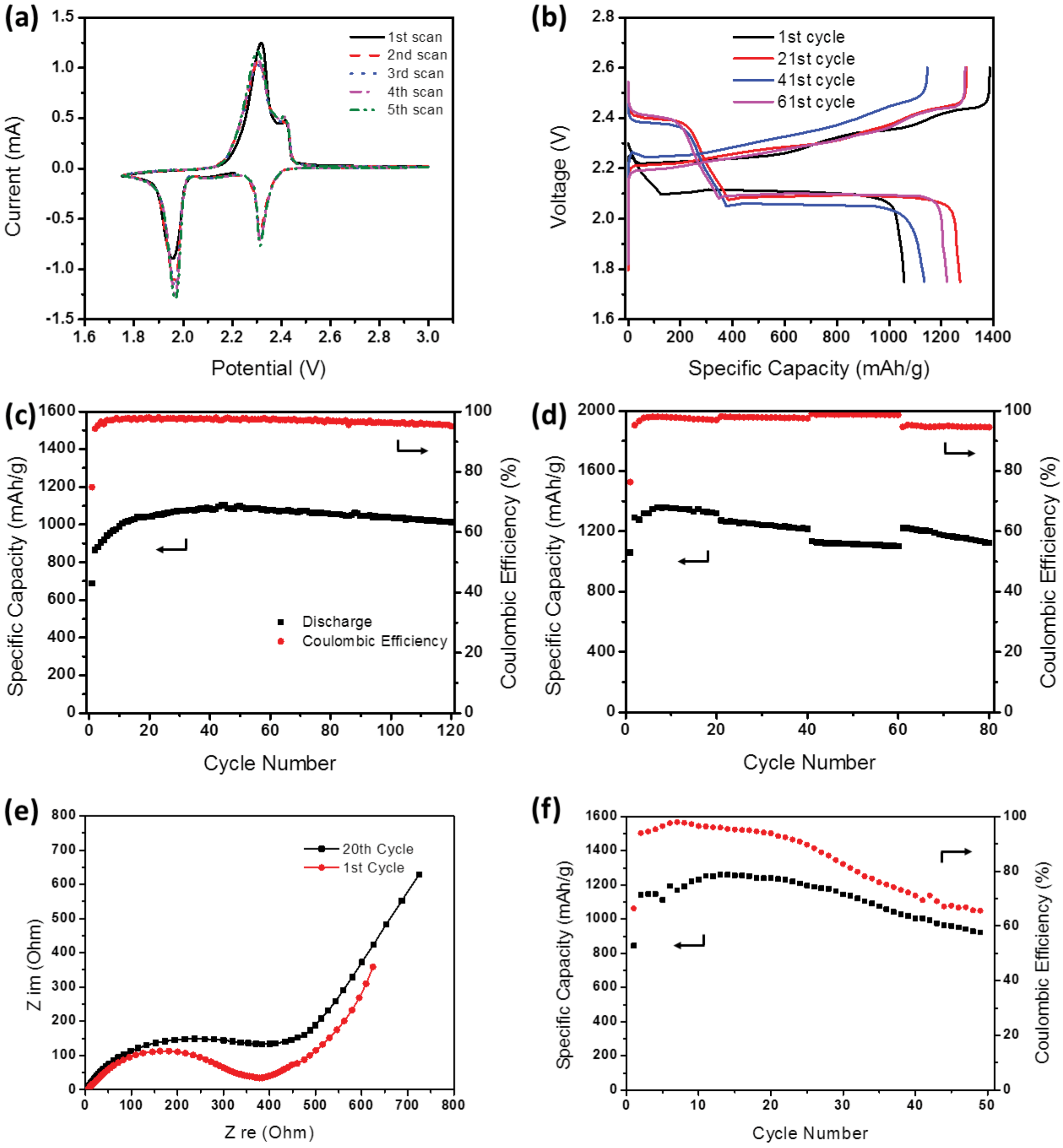

Figure 6.5 Electrochemical characterization results for lithium-sulfur cells. (a) cyclic voltammograms of lithium/lithium polysulfide couples between 1.75V and 3.0V, (b) voltage-capacity profiles of lithium/lithium polysulfide couples at different current densities, (c) reversible capacity and coulombic efficiency of a Li-S battery at 1000 mA/g current in galvanostatic cycle tests, (d) reversible capacity and coulombic efficiency of a Li-S battery at various current densities of 200 mA/g, 500 mA/g and 1000 mA/g, (e) Nyquist plots of a Li-S battery from EIS measurements after the 1st cycle and the 20th cycle, (f) reversible capacity and coulombic efficiency of a Li-S battery without $LiNO_3$ additive at a current density of 200 mA/g.

Figure 6.5d displays the reversible capacity and coulombic efficiency of the Li-S cell at various current densities. The sample cell shows a high initial reversible capacity of 1057mAh/g under a current of 200mA/g and gradually increase to 1340 mAh/g. Under 500 mA/g, 1A/g and back to 200mA/g, the batteries achieved high capacities of 1216 mAh/g, 1101 mAh/g and 1023 mAh/g, respectively. The increased specific capacity is expected as the volume ratio of electrolyte to cathode in the Li-S cell was intentionally set at a low level. A slight decrease in the capacity with increased cycle number was also observed, which may be attributed to the passivation of insoluble polysulfides on both negative and positive electrodes. The implication of gradually increased specific capacity and change of voltage profiles with proceeding charge/discharge processes is the sluggish reaction kinetics of precipitation and dissolution of polysulfide species in catholyte and electrolyte. The highest level coulombic efficiency was obtained at the 1A/g density, this is expected if the shuttle mechanism induced charge inefficiency has less impact upon large charge currents. Therefore further constant current charge/discharge tests were carried out with a specific current of 1A/g. The reduction reactions of elemental sulfur in a typical Li-S cell can be divided into a four stages stepwise process: (i) conversion of solid state sulfur into high order polysulfides which can be dissolved in aprotic solvents, (ii) high order polysulfides reduced to low order liquid polysulfides, (iii) low order liquid polysulfides reduced to solid lithium sulfides, and (iv) the complete reduction to lithium disulfide. The chemical equilibrium of polysulfide species in electrolyte is highly dependent on their concentration in electrolyte and temperature. Excessive electrolyte solvent with low polysulfide concentration is favorable for sulfur utilization at the initial cycling of Li-S cell, while low electrolyte volume to sulfur electrode ratio often causes a pattern of gradual increase in the specific capacity during the charge/discharge cycling tests. This phenomenon can be attributed to the high polysulfide concentration in electrolyte, which increases the overall viscosity of electrolyte, and polysulfide migration in electrolyte is subsequently hindered.[160] The decreasing trend in coulombic efficiency of cycling Li-S cells is associated with the continuous decomposition of $LiNO_3$ electrolyte additive. With the disappearance of active $LiNO_3$ from electrolyte, the surface of lithium anodes gradually become rough and leads to increased side reactions between lithium anodes and electrolyte. As a result, the impedance of cells also increases with the increase of cycle number (Figure 6.5e).

The use of PAN-derived carbon fibers instead of sulfur cathodes with engineered nanostructure reduced the difficulties of sulfur cathode material preparation. With flexible carbon fiber sheets as conducting agents, the semi-liquid lithium polysulfide cathodes exhibited good capacity retention rate at both low and high current densities. This feature can be attributed to the nature of soluble polysulfide species which avoid the stress to conductive matrix from repeat volume expansion of solid state sulfur. In addition, the contribution of lithium nitrate additive in stabilizing the reversible capacities of batteries was also examined. $LiNO_3$ is one of the most widely used electrolyte additives in lithium-sulfur batteries, which helps stabilize the surface of lithium anodes. As shown in Figure 6.5f, both the reversible capacity and the coulombic efficiencies of lithium sulfur cells cycled under 200 mA/g current dropped quickly when using the 1.0 M LiTf in DME: DOL electrolyte without $LiNO_3$ additive, the discharge capacities already fell below 1000 mAh/g within 50 cycles.

The insulating Li_2S precipitation on both anode and cathode sides is a direct result from polysulfide migration. The deposition of Li_2S has a detrimental effect to the structural stability as the volume difference between Li_2S and S phases is huge. The use of liquid phase polysulfides as a cathode for Li-S cells can suppress the detrimental reactions in which the insulating Li_2S is accumulated on the surface of cathode. Cells with polysulfide acts as the cathode material can thereby deliver an enhanced cycling performance when compared with conventional Li-S cell configurations.

The investigation of polysulfide phase evolution at the cathode end of Li-S cells during battery operation was conducted by ex-situ X-ray diffraction measurements in conjunction with scanning electron microscopy on carbon fiber substrates extracted from Li-S cells after 5 complete charge/discharge cycles. However, these attempts to confirm the interpretation of Li-S redox reactions were unsuccessful. In general, X-ray diffraction tests of the cycled carbon fiber sheets, extracted from Li-S cells at various stages of discharge or charge, did not give any indication of intermediate phases, only peak-free patterns were obtained. The deposition of Li_xS layer on the surface of carbon fibers was confirmed by SEM (as shown in Figure 6.3 e and f). It is generally accepted that the growth of insulating Li_2S layers on the surface of sulfur cathode is associated with the increasing cycle number of Li-S cells. As a result, the failure of sulfur cathodes attributed to the deformation of cathode structure is often observed in Li-S cells equipped with a solid state sulfur cathode. By switching to semi-liquid cell configuration with catholyte as the active material, the detrimental effects from Li_2S deposition can be suppressed. Sulfur and the low order reduced polysulfide species, i.e. Li_2S_2, Li_2S, are electronically non-conductive, and conductive agent must be incorporated in sulfur containing cathode materials to improve the overall conductivity of electrode. The Li-S cell loaded with Li_2S_6 catholyte shows a voltage-capacity curve similar to that of Li-S cell with solid state carbon-sulfur cathode, except for minor polarization upon the charging process. The slight difference in voltage profiles of two types of Li-S cell configuration imply the improved reaction kinetics from the utilization of catholyte. Therefore the investigation on solid state sulfur cathode was excluded from further investigation.

6.4 Conclusions

The polysulfide catholyte percolated porous carbon sheet demonstrated good performance as semi-liquid positive electrode for Li-S cells. The assembled Li-S cells showed a high reversible capacity over 1010 mAh/g for 120 cycles, at the current rate of 1000 mA/g. The Li-S cells also exhibited excellent rate capabilities under various current rates at 200 mA/g, 500 mA/g and 1000 mA/g, the best results for coulombic efficiency was obtained at the highest current rate. The stacks of carbon fibers forms a highly porous structure that offers both high free volume and high surface area to absorb/adsorb the sulfur catholyte, and the conductive carbon fibers provide large number of electrochemically active sites for Li/S redox reactions. . In addition, the cycle life of Li anode in Li-S cells being greatly extended with $LiNO_3$ electrolyte additive. Nevertheless, this Li-S cell configuration still suffered from the low level coulombic efficiencies due to the shuttle mechanisms of polysulfide species which requires further research works.

Chapter 7 Antimony sulfide – graphene composite anode materials

7.1 Introduction

Nanostructured transition metal oxides or sulfides that can react with lithium via a conversion process are also considered as ‘advanced’ anode materials for future lithium secondary batteries owing to their higher gravimetric charge capacity compared with that of graphite anodes. However, the application of conversion type negative electrode materials in lithium-ion batteries experienced fatal issues including: (i) poor electrode stability due to high level structural deformation accompanied by large volume changes, (ii) side reactions with the electrolyte during the electrochemical reduction process, which are attributed to large surface areas of their nanoarchitectures, (iii) low level energy efficiency caused by the high level voltage hysteresis between the discharge and charge steps, (iv) low initial coulombic inefficiency. These pose inherent restrictions on the maximum attainable energy in any potential lithium battery system utilizing these materials as anode. Understanding the fundamental principles of the inefficiencies followed with carefully designed electrode materials can certainly improve the reversibility of conversion type transition metal oxide compounds, but some obstacles originate from the nature of non-aqueous battery chemistries e.g. interfacial reactions remain challenging. Therefore, despite the conversion type electrode materials remaining an active topic in academic research with large number of publications emerging from time to time, very limited progress has been shown towards practical battery applications. In this case study, the orthorhombic Sb_2S_3 (stibnite) – reduced graphene oxide composite is selected as an anode materials for lithium and sodium secondary batteries, with the hope of exploring a facile synthesis approach to effectively improve the electrochemical performance of Sb_2S_3 based conversion type electrode materials at a relatively low cost.

$$12\ Li^+ + Sb_2S_3 \underset{\text{discharge}\rightarrow}{\overset{\leftarrow\text{charge}}{\rule{2cm}{0.4pt}}} 3\ Li_2S + 2\ Li_3Sb, \tag{7-1}$$

$$12\ Na^+ + Sb_2S_3 \underset{\text{discharge}\rightarrow}{\overset{\leftarrow\text{charge}}{\rule{2cm}{0.4pt}}} 3\ Na_2S + 2\ Na_3Sb, \tag{7-2}$$

Assuming a complete conversion reaction between lithium (or sodium) ions and Sb_2S_3 during battery operation according to equations 7-1 and 7-2, the bulk Sb_2S_3 with a typical density of 4.63 g/cm^3 offers a high theoretical specific capacity of ca. 850 mAh/g as anode material for both lithium and sodium cells. However, high expectations on the increase of battery energy from Sb_2S_3 based anode alone is unrealistic because the electrical resistance for bulk stibnite crystal is rather high (about 10^8 Ohms for a centimeter rod measured near room temperature), therefore nano downsizing process is necessary in order to turn Sb_2S_3 into electrode material by reducing the electronic/ionic diffusion length at the expense of volumetric capacity. In this study, conductive reduced-graphene oxide sheets with high surface area as well as certain charge storage capabilities are selected as the backbone structure to synthesize the Sb_2S_3/graphene composite. The oxygen containing groups on graphene can act as binding sites, thus ensures the sufficient connection between semiconductor and graphene as well as avoid the aggregation of nanoparticles during material synthesis. This composite design is expected to compensate the reduced capacity of Sb_2S_3 and accommodate the volume change of Sb_2S_3 phase upon the conversion reaction with lithium and sodium ions. The time-saving synthesis process adopted for Sb_2S_3/graphene composite preparation is a facile approach utilizing the microwave-assisted solvothermal reaction which offers great convenience in the formation of Sb_2S_3 nanoparticles on supporting graphene sheets.

7.2 Experimental

7.2.1 Material synthesis

Chemicals used in this study include antimony chloride ($SbCl_3$), super P carbon, ethylene carbonate (EC), dimethyl carbonate (DMC), fluorinated ethylene carbonate (FEC), graphite powder (C), hydrogen peroxide (H_2O_2), isopropyl alcohol (IA, C_3H_7OH), polyvinyl pyrrolidone (PVP, M_w=40,000g /mole), potassium permanganate ($KMnO_4$), sodium nitrate ($NaNO_3$), sodium perchlorate ($NaClO_4$), sodium carboxymethyl cellulose (CMCNa), sulfuric acid (H_2SO_4), and thiourea (CH_4N_2S). All chemicals were purchased from Sigma-Aldrich and used as received without further treatment.

The graphene oxide (GO) precursor was prepared from fine graphite powder via a modified Hummers' method, after which the obtained dry GO powder was dispersed in isopropyl alcohol (IA) with ultrasonication to form a homogeneous suspension containing ca. 0.10 g/L concentration exfoliated graphene oxide nanosheets. Antimony chloride was then added into GO/IA suspension to a concentration of $100g_{Sb}$/L and heated at 30ºC for 5 minutes in a microwave reactor. After the complete dissolution of antimony chloride in GO/IA suspension, an IA solution containing thiourea and polyvinyl pyrrolidone was added into the Sb-GO/IA suspension. The concentrations of thiourea and polyvinyl pyrrolidone in the final suspension were 0.6mol/L and 5g/L, respectively. After adding in thiourea and polyvinyl pyrrolidone, the suspension was heated in microwave reactor at 100°C for 30 minutes. The solution was under vigorous stirring with a magnetic stirring bar during the microwave-assisted solvothermal reaction. Once the reaction was complete, the solid material in the suspension was separated by filtration and washed with ethanol and distilled water. The obtained black color powder was first vacuum dried under 50ºC for 6 hours before morphology determination under SEM. Once the desired particles-on-sheets morphology was confirmed, the sample was transferred into a tube furnace, and heated at 450ºC under argon atmosphere protection for 2 hours to complete the thermal reduction of graphene oxide. The sample after microwave-solvothermal reaction and the sample after thermal reduction are referred as the Sb_2S_3@GO and Sb_2S_3@RGO composites, respectively. The Sb_2S_3@RGO composite obtained after the thermal reduction had a greyish metallic luster under natural light, while the Sb_2S_3@GO sample only appeared as a dim dark color.

7.2.2 Material characterization

The structural characteristics of Sb_2S_3 and Sb_2S_3@RGO composite samples were characterized by X-ray diffraction (XRD), scanning electron microscopy (SEM), and transmission electron microscopy (TEM), Brunauer, Emmet and Teller (BET) measurements, Raman spectroscopy. Thermal gravimetric tests were also performed to determine the weight ratio of Sb_2S_3 inside the composite.

7.2.3 Electrochemical characterization

For an electrochemical evaluation of Sb_2S_3@RGO composite, the material was made into electrodes by coating copper foil substrates with a slurry containing the fine Sb_2S_3@RGO composite power (80 wt%), acetylene black (10 wt%), and sodium carboxymethyl cellulose (CMCNa, 10 wt%) binder with distilled water as the disperse media. The coated electrodes were dried under vacuum at 120 °C for 8 hours and pressed with 5 MPa force afterwards for material densification. The as prepared electrode were transferred into an argon-filled glove box for coin cell assembly. For lithium half-cells, Li foil was used as the counter and reference electrodes, and 1M $LiPF_6$ in ethylene carbonate (EC)/ diethyl carbonate (DEC) (1 : 1 by volume) as the electrolyte in conjunction with Celgard 2400 separator. For sodium half-cells, trimmed sodium metal pieces were used as the counter electrodes, and 1M $NaClO_4$ in ethylene carbonate (EC)/ dimethyl carbonate (DMC) (1 : 1 by volume) with 2% (wt./v) fluoroethylene carbonate (FEC) was used as the electrolyte, and glass fiber membranes were used as the separators due to the rough surface of manually trimmed metallic sodium. The assembled cells were examined with cyclic voltammetry and charge/discharge cycling tests. During cycling tests, all cells were tested in Galvanostatic mode in a fixed voltage window between 0.1 V and 2.0 V under various current densities. Li (Na) ion was inserted into the working electrode during the discharge process of cells, and extracted from the working electrodes during subsequent charge processes.

7.3 Results and discussion

7.3.1 Compositions and morphologies of synthesized materials

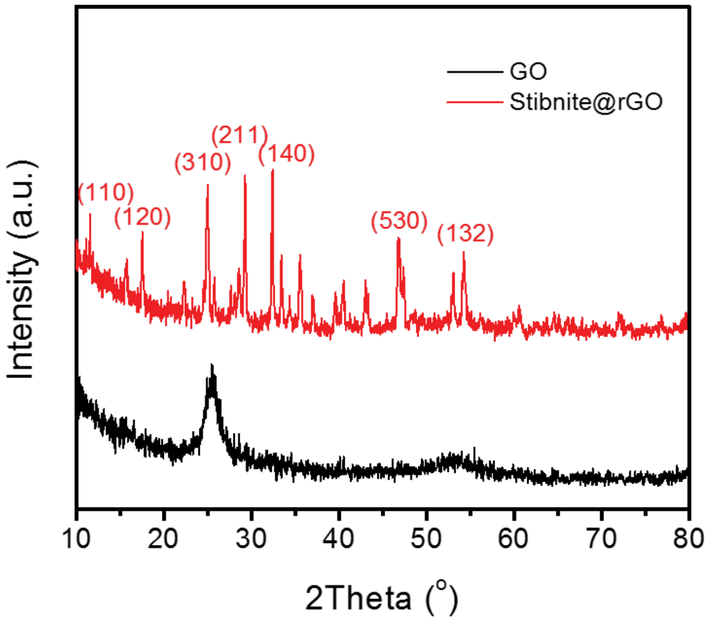

Figure 7.1 XRD patterns of synthesized GO and Sb_2S_3@RGO composite. (a) GO obtained from modified Hummers' method, (b) Sb_2S_3@RGO composite after thermal treatment.

Figure 7.1 shows the XRD patterns of the GO flakes obtained from the modified Hummers' method and Sb_2S_3@RGO composite obtained from the microwave-assisted solvothermal approach, both samples were collected after the thermal treatment at 300°C under vacuum. The major peaks GO center at $2\Theta = 26°$ are attributed to the (002) plane of graphite. All the peaks of Sb_2S_3@RGO correspond to the orthorhombic phase stibnite (JCPDS No. 42-1393, space group: Pbnm, a = 11.25 Å, b = 11.33 Å, c = 3.83 Å), indicating a high purity crystalline phase was obtained after the complete synthesis process.

Figure 7.2 a,b,c shows the scanning electron imaging of graphene oxide (GO) sheets, Sb_2S_3@GO and Sb_2S_3@RGO composite materials. The typical morphology of GO obtained from the modified Hummers' method was a corrugated sheet in scanning electron microscopy (Figure 7.2a), while the Sb_2S_3@GO and Sb_2S_3@RGO composites both show uniform particles with an average size below 100 nm spread on graphene layers. In addition, the SEM images (Figure. 7.2 b and c) clearly show the uniform distribution of Sb_2S_3 particles on the surface of graphene, which confirmed the microwave-assisted synthesis approach successfully promoted the homogeneous particle growth on graphene-oxide templates. The transmission electron microscopy (TEM) images of the Sb_2S_3@RGO composite are displayed in Figure 7.2 d,e,f. The morphological features of Sb_2S_3@RGO sample under TEM were in good agreement with SEM observation, where the Sb_2S_3 nanoparticles with the size of about 100 nm were densely coated on the graphene sheet owing to the low GO concentration in this composite, but area aggregated of nanoparticles were not observed. The high resolution TEM images (Figure 7.2 e,f) revealed the ordered diffraction planes of the stibnite crystallites with an interplanar distance of 0.28 nm, which corresponds to the (211) interplanar distance of stibnite.

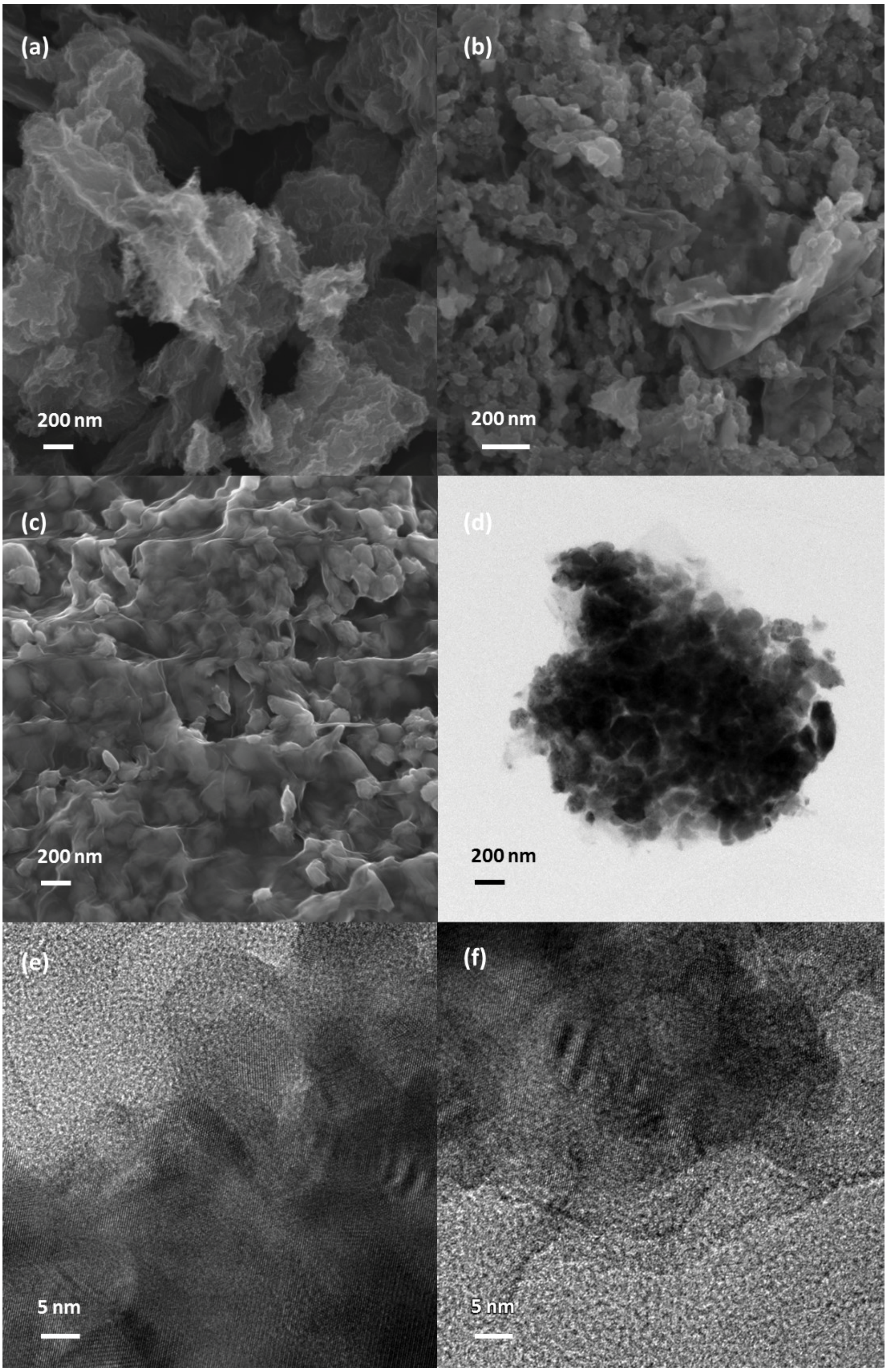

Figure 7.2 SEM images and TEM images of GO, Sb_2S_3@GO, Sb_2S_3@RGO composite. SEM images of (a) GO flakes, (b) Sb_2S_3@GO, (c) Sb_2S_3@RGO composite. TEM images of Sb_2S_3@RGO at low (d) and high (e,f) magnifications.

Table 7.1 Thermogravimetric analysis and Raman spectroscopy results. Weight ratio of Sb_2S_3 phase in Sb_2S_3@GO, Sb_2S_3@RGO composite are given in the 1st row, and intensity ratio between D band and G band (I_D/I_G) in Raman spectrum of bare GO, Sb_2S_3@GO before thermal reduction and Sb_2S_3@RGO composite are given in the 2nd row.

Sample	Graphene oxide (GO)	Sb_2S_3@GO	Sb_2S_3@RGO
Weight ratio of Sb_2S_3	**N/A**	**62.50**	**71.78**
I_D/I_G ratio	**1.29**	**1.26**	**1.12**

The weight ratio of stibnite in Sb_2S_3@GO and Sb_2S_3@RGO samples were determined by thermogravimetric analysis (TGA). The Raman spectra of three samples, i.e. bare GO, Sb_2S_3@GO before thermal reduction and Sb_2S_3@RGO after thermal reduction, were collected to determine the D/G ratios of carbon content in these materials. The TGA and Raman results are presented in Table 7.1 and Figure 7.3. The TGA results of Sb_2S_3@GO and Sb_2S_3@RGO clearly show increased weight ratio of Sb_2S_3 in the thermally-reduced Sb_2S_3@RGO sample compared with that in the Sb_2S_3@GO sample. The loading rates of Sb_2S_3 particles in the Sb_2S_3@RGO composite were calculated based on the TGA results and used as the references in further electrochemical characterizations. The Raman spectra of GO, Sb_2S_3@GO and Sb_2S_3@RGO composite, as shown in Figure 7.3b, revealed a clear decrease trend of the D/G band ratio from bare GO to Sb_2S_3@RGO composite, indicating an increased ratio of sp^2 carbon in Sb_2S_3@RGO sample, which corroborates the successful thermal reduction of the GO phase by heating the sample in argon atmosphere without additional reducing agents. The nitrogen adsorption-desorption isotherms and the Brunauer, Emmet and Teller (BET) plot of Sb_2S_3@RGO composite are as shown in Figure 7.4. The specific surface area of Sb_2S_3@RGO composite sample is 8.46 m^2/g according to linear regression results of the Brunauer, Emmet and Teller (BET) plot (Figure. 7.4b).

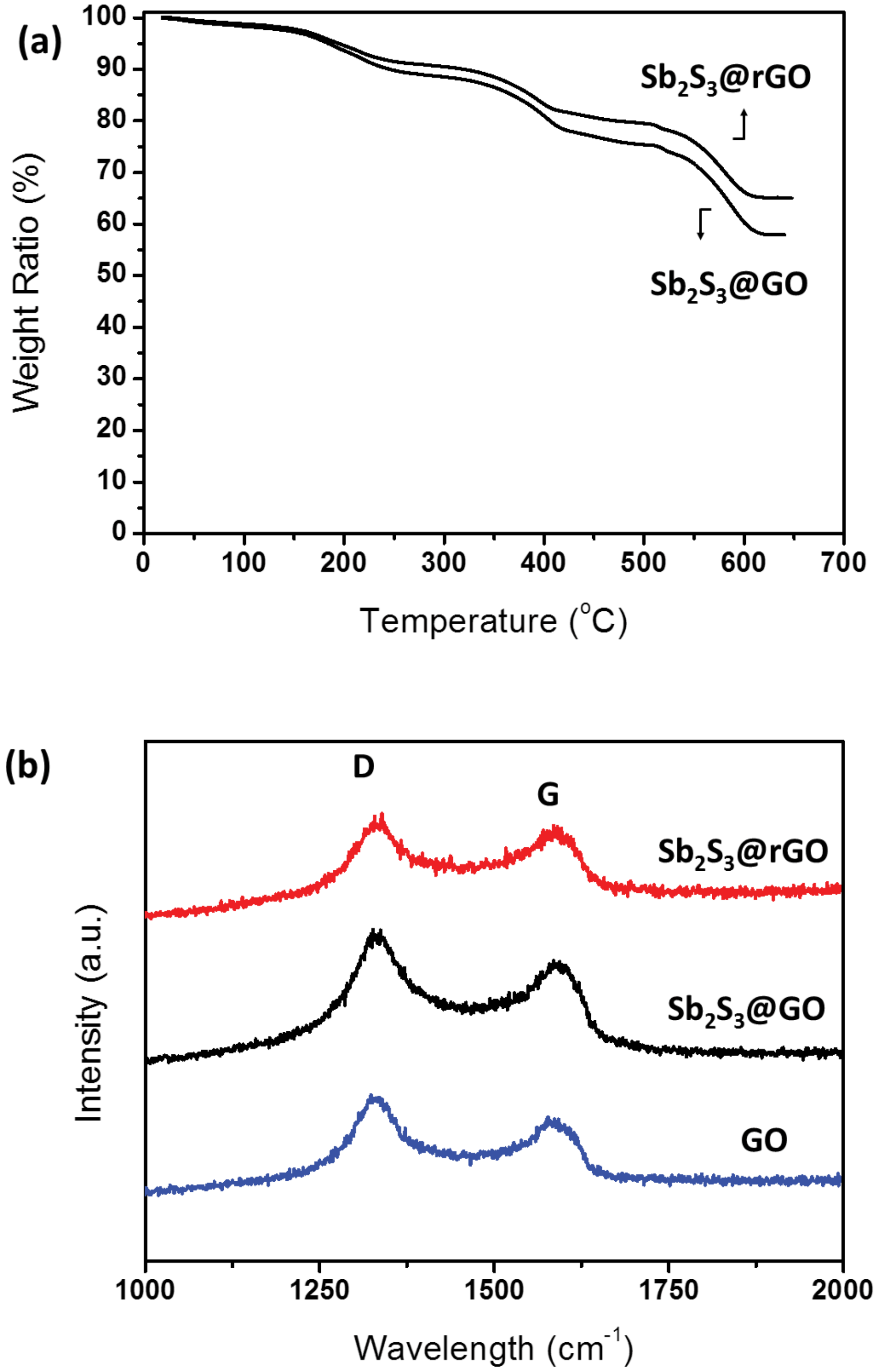

Figure 7.3 Thermogravimetric curves and Raman spectra of Sb_2S_3@GO and Sb_2S_3@RGO composites. (a) Weight-temperature curve from thermogravimetric analysis of Sb_2S_3@GO and Sb_2S_3@RGO samples, (b) the Raman spectra of GO, Sb_2S_3@GO and Sb_2S_3@RGO samples.

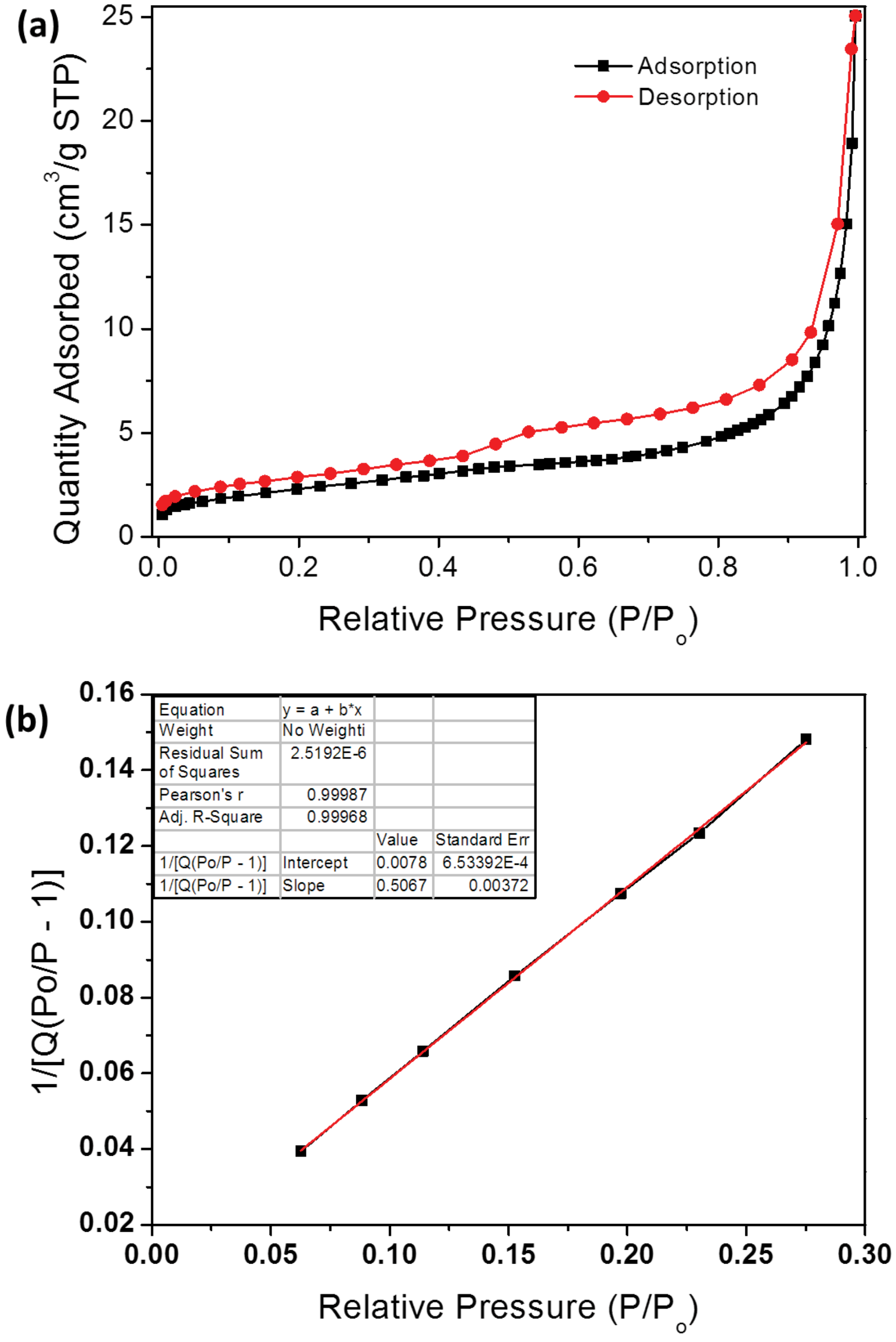

Figure 7.4 Nitrogen adsorption-desorption isotherms (a) and the BET plot (b) from Sb_2S_3@RGO composite.

7.3.2 Electrochemical characteristics in lithium half-cells

The current peaks associated with the electrochemical reactions between Sb_2S_3@RGO composite and lithium can be directly observed from the cyclic voltammetry (CV) profiles of the assembled lithium half cells. Fig. 7.5a shows the cyclic voltammetry plot of Sb_2S_3@RGO composite electrodes between 0.01 V and 2.5 V versus lithium electrodes. During the initial CV scan, the Sb_2S_3@RGO electrode shows three reduction peaks at 1.6 V, 1.4 V, and 0.8 V, and two oxidation peaks at 1.1 V and 2.1 V. The reduction peak at 1.6V corresponds to partial reduction of antimony (Sb) and formation of polysulfide species (Li_XS_n), while reduction peaks at 1.4 V and 0.8 V correspond to formation of lithium disulfide and complete reduction of antimony, and formation of lithiated antimony (Li_3Sb), respectively. The oxidation peak at 1.1 V corresponds to liberation of antimony from lithium-antimony alloy, and the oxidation peak at 2.1 V corresponds to reconstruction of stibnite phase (Sb_2S_3). In the subsequent four cycle CV scans, the Sb_2S_3@RGO electrode shows redox peaks identical to that of the initial CV scan, suggesting that reactions between Sb_2S_3@RGO composite and lithium are sustainable. In a previous study of amorphous Sb_2S_3 anode based on X-ray absorption near-edge structure (XANES) analysis, the detailed reaction mechanism of full conversion between Sb_2S_3 and lithium is suggested as follows[274]:

$$Sb_2S_3 \rightarrow Li_xS + Sb \rightarrow Li_2S + Sb \rightarrow Li_2S + Li_3Sb \text{ (Discharge)}, \qquad 7\text{-}3$$

$$Li_2S + Li_3Sb \rightarrow Li_2S + Sb \rightarrow Sb_2S_3 \text{ (Charge)}, \qquad 7\text{-}4$$

Fig. 7.5b shows the cyclic voltammetry plot of a different lithium half-cell with a Sb_2S_3@RGO composite working electrode between 0.05 V and 2.0 V. During the initial CV scan, the Sb_2S_3@RGO electrode shows three reduction peaks at 1.6 V, 1.4 V, and 0.8 V, and one oxidation peak at 1.1 V. From the second cycle on, the Sb_2S_3@RGO ele-

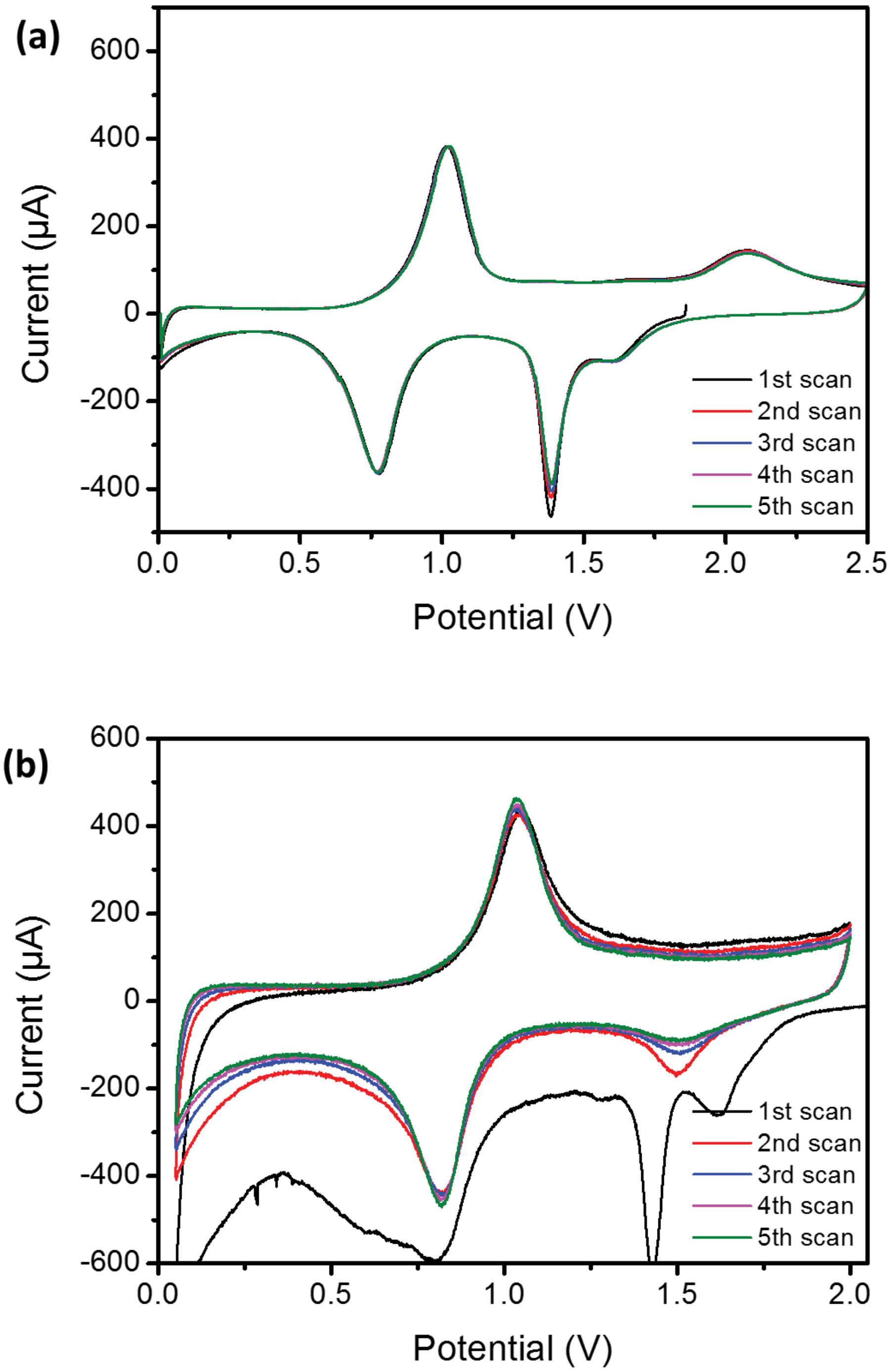

Figure 7.5 Cyclic voltammograms of Sb_2S_3@RGO composite in lithium cells between 0.01 V and 2.5 V (a), and between 0.05 V and 2.0 V (b).

ctrode shows three reduction peaks at 1.6 V, 1.4 V, and 0.8 V, and one oxidation peak at 1.1 V. The appearance of reduction peak at 1.5 V in the second cycle CV scan associated with the disappearance of reduction peaks at 1.6 V and 1.4 V suggesting that the reduction peak at 1.5 V is the merged reduction peaks of 1.6 V and 1.4 V in the initial cycle, corresponding to different conversion reaction steps. The slightly higher intensity of current peaks in Fig 7.5b compared with that of Fig 7.5a is suspect to be attributed to differences in area specific loading rate of electrode material.

In order to confirm phase transition of Sb_2S_3 particles, ex-situ XRD was performed on the Sb_2S_3@RGO composite electrodes extracted from cycled cells after one complete charge/discharge cycle with upper cut-off voltages at 2.0 and 3.0 V. However, no XRD peaks were identified from the extracted composite electrode, suggesting an amorphous phase of Sb_2S_3 is dominant inside the electrode after the recombination of liberated Sb and S phases during the initial charge-discharge process.

Figure 7.6 a and b shows the typical voltage profiles (voltage versus capacity plot) of the Sb_2S_3@RGO composite electrodes in lithium half cells during one complete charge-discharge cycle between 0.01 V and 2.5 V (a), and between 0.01 V and 3.0 V (b) at a fixed current density of 50 mA/g (the current density is calculated based on the weight ratio of Sb_2S_3@RGO composite in the electrode). These voltage profiles are in good agreement with cyclic voltammetry results. It is also worth noted that the Sb_2S_3@RGO composite exhibited relatively poor reaction kinetics with lithium as there was a clear voltage hysteresis between charge and discharge steps, especially when the cell was cycled between 0.01 V and 3.0 V. The voltage hysteresis is a common phenomenon overserved in conversion type electrodes, for which overpotential is necessary to overcome the reaction barrier during the extraction of lithium ions and reformation of metal oxide, metal sulfide, etc. Fig. 7.6 c and d shows the specific capacity of the Sb_2S_3@RGO composite electrode versus cycle number with different upper cut-off voltages. At the voltage range between 0.01 V and 2.0 V, the first discharge and charge capacities are 1095 mAh/g and 595 mAh/g, respectively, corresponding to an initial cycle coulombic efficiency of 54.34 %. Such a low initial coulombic efficiency of the Sb_2S_3@RGO composite electrode can be explained by the high surface area of the porous electrodes due to the nature of active materials, which causes irreversible decomposition of a large quantity electrolyte on the electrode/electrolyte interphase upon the initial lithium insertion process. The coulombic efficiency gradually increases to above 98% within 8 cycles and remains stable in subsequent cycles. As to the capacity retention rate, the Sb_2S_3@RGO composite electrode showed rather poor reversibility of electrochemical reaction with lithium as the reversible capacity dropped to 353 mAh/g after 100 cycles, corresponding to a capacity retention rate of 61.92%.

When the electrode was cycled between 0.01 V and 3.0 V, the Sb_2S_3@RGO electrode showed higher reversible capacity at 872 mAh/g in the first cycle, but the capacity decay is also faster between 0.01 V and 3.0 V compared to that between 0.01 V and 3.0 V. The capacity retention rate was only approximately 46% after 70 cycles of charge and discharge of the cells (as shown in Fig. 7.6 d). However, as shown in Fig. 7.6e, the Sb_2S_3@RGO composite electrode exhibits excellent rate capability under a wide range of currents from 50 mA/g to 1000 mA/g, with the reversible capacity only slightly dropping under doubled or quadrupled current densities of charge-or discharge cycling. The Nyquist plots from EIS measurements of cells at the charged state after the 1st and the 20th cycle are displayed in Figure 7.6f. The cell demonstrated a high charge transfer resistance. The impedance profile at the 20th cycle showed a slightly larger single semicircle similar to that of the 1st cycle, which indicates well-sustained electronic contact within the electrode after short-term cycling. These good electrochemical chara-

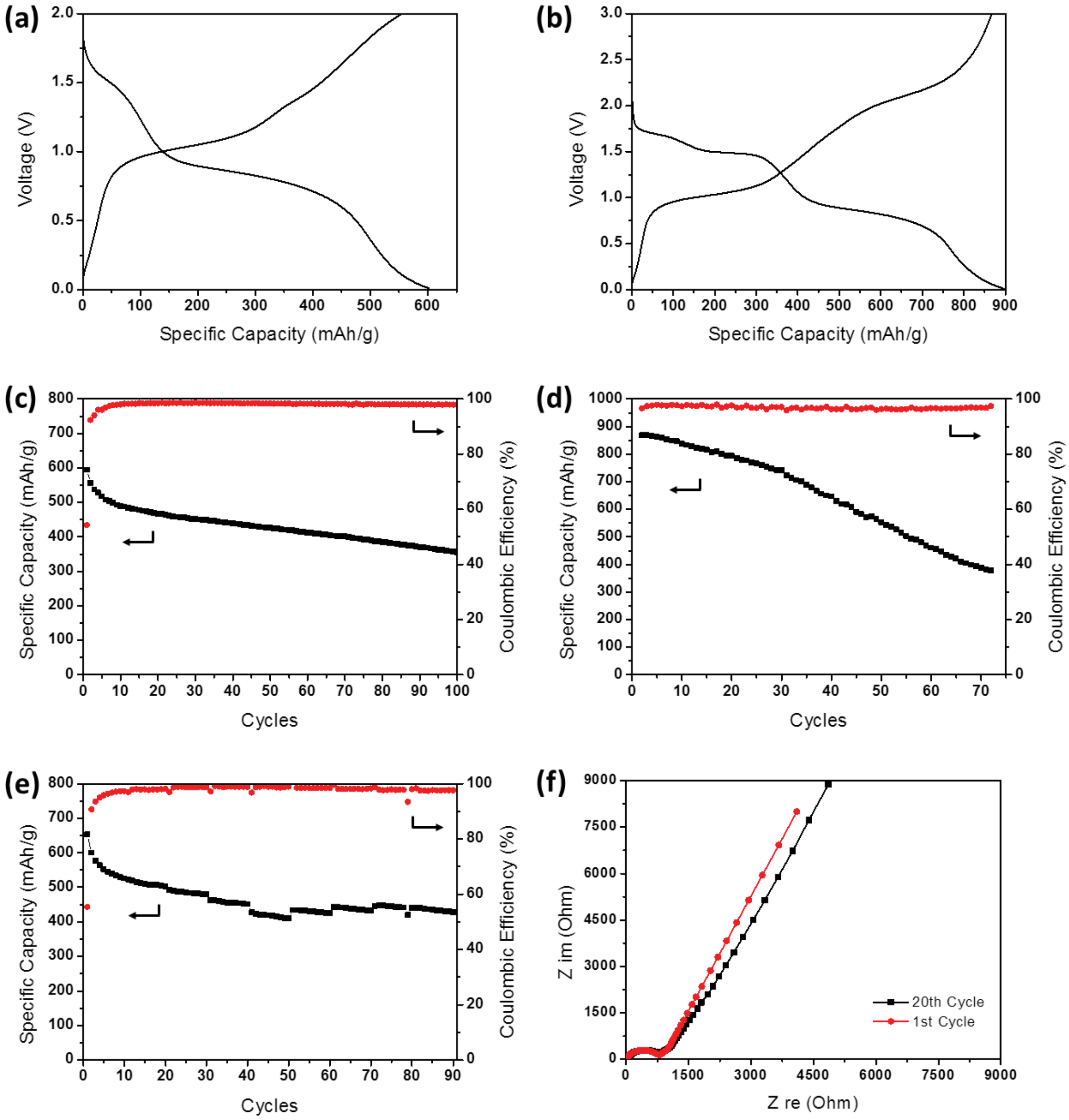

Figure 7.6 Electrochemical characterization results for lithium cells. Voltage profiles of Sb_2S_3@RGO composite electrode in lithium half-cells between 0.01 V and 2.0 V (a), and between 0.01 V and 3.0 V (b). Reversible capacities and coulombic efficiencies of Sb_2S_3@RGO composite electrode in lithium half cells between 0.01 V and 2.0 V (c), and between 0.01 V and 3.0 V (d) at 50 mA/g. Cycling performance of Sb_2S_3@RGO composite electrode at 50 mA/g, 100 mA/g, 200 mA/g, 500 mA/g, 1000 mA/g, and back to 50 mA/g between 0.01 V and 2.0 V (e), Nyquist plots of Sb_2S_3@RGO electrode in lithium half cells after the 1st and 20th cycles (f).

cteristics under high current rates are attributed to the structural feature of Sb_2S_3@RGO composite, namely, the uniform distribution of Sb_2S_3 on the two dimensional flexible, conductive and high strength graphene layers, which helps to accommodate a large volume change of Sb_2S_3 and maintain solid conductive networks within electrodes upon cycling versus lithium under low depth of charge and discharge conditions.

7.3.3 Electrochemical characteristics in sodium half-cells

To investigate the performance of Sb_2S_3@RGO composite electrodes as negative electrodes for sodium batteries, cyclic voltammetry tests were performed with sodium half cells equipped with Sb_2S_3@RGO composite electrode between 0.01 V and 2.5 V, and between 0.05 V and 2.0 V, and the corresponding cyclic voltammograms are as shown in Figure 7.7 a and b, respectively. In both CV plots the position of reduction peaks during the subsequent cycles showed large variation from that in the first cathodic scan, suggesting a formation step during the first discharge process these cells, which is believed to be the result of passivation of electrolyte species at the electrode/electrolyte interphase. In Figure 7.7a, the Sb_2S_3@RGO electrode shows three reduction peaks at 1.1 V, 0.7 V, and 0.2 V, and two oxidation peaks at 0.8 V and 1.25 V during the initial CV scan. From the second cycle on, the Sb_2S_3@RGO electrode shows multiple reduction peaks at 1.3 V, 1.2 V, 0.85 V, 0.4 V and 0.2 V, and two oxidation peaks at 0.8 V and 1.2 V. The changes of redox peaks from the initial cycle scan to subsequential scans suggests variation of detailed reaction mechanisms within the Sb_2S_3@RGO composite electrode. However, similar to the case of lithium cells, ex-situ XRD was performed on the Sb_2S_3@RGO composite electrodes extracted from cycled sodium cells. These also showed peak-free patterns of intermediate phases, therefore more specific examination measures (i.e. XPS, XANES) are still required for the determination of reaction mechanisms between the Sb_2S_3@RGO composite and sodium, which is not clear-cut at this stage. In Figure 7.7b, the Sb_2S_3@RGO composite electrode shows three reduction peaks at 1.2 V, 0.75 V, and 0.25 V, and two oxidation peaks at 0.75 V and 1.3 V during the initial CV scan between 0.05 V and 2.0 V. In the subsequent CV scans,

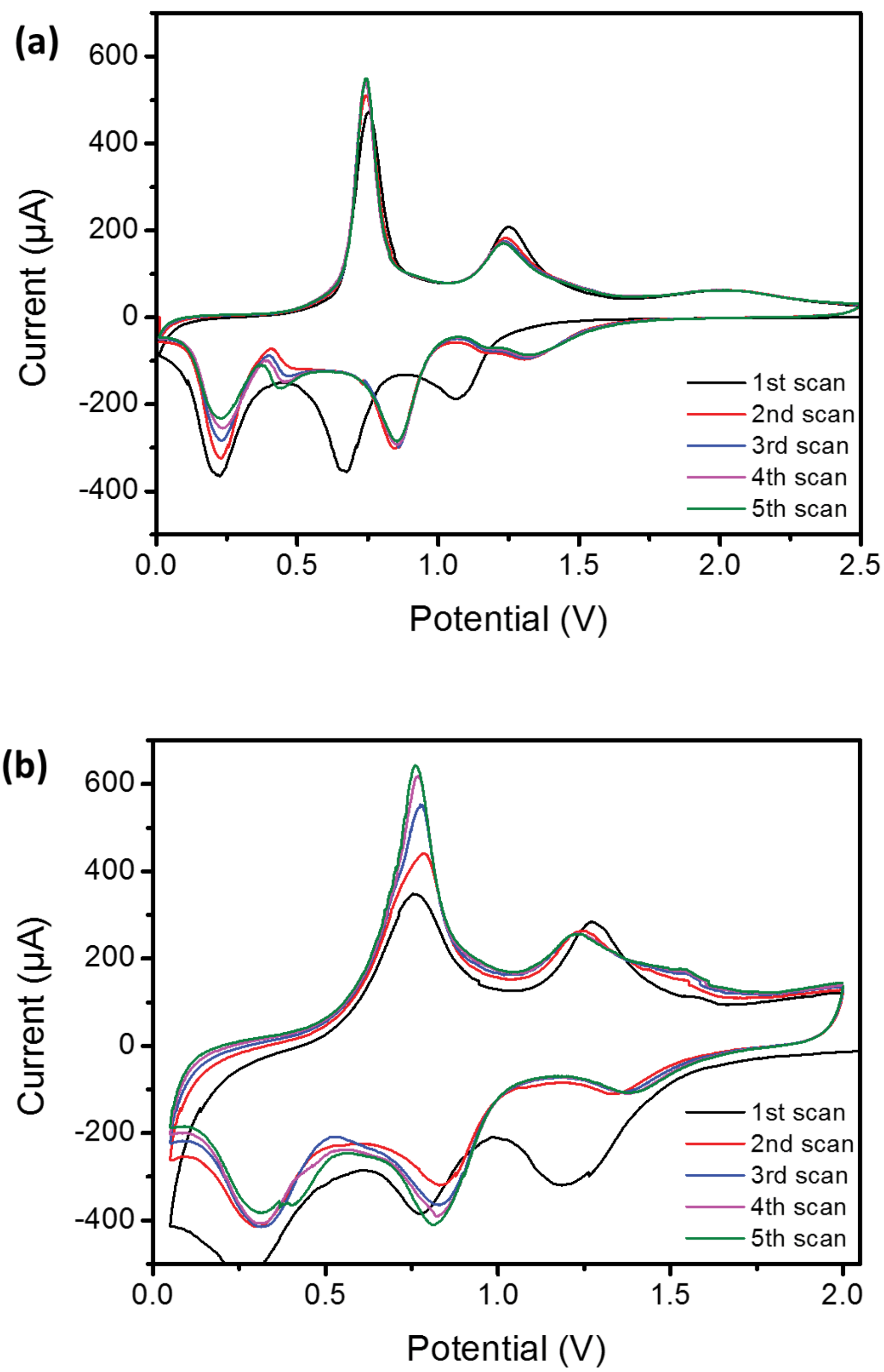

Figure 7.7 Cyclic voltammograms of Sb_2S_3@RGO composite in sodium cells between 0.01 V and 2.5 V (a), and between 0.05 V and 2.0 V (b).

the Sb_2S_3@RGO electrodes showed three reduction peaks at 1.4 V, 0.8 V, and 0.3 V, and three oxidation peaks at 0.8 V, 1.2 V and 1.55 V. The change of redox peak intensity from the initial cycle scan to subsequential scans implies much slower reaction kinetics and lower level active material utilization of Sb_2S_3@RGO composite electrode in the sodium cells compared to that in the lithium cells.

The voltage profiles of Sb_2S_3@RGO composite electrodes versus sodium under 50 mA/g charge/discharge current between 0.01 V and 2.0V, and between 0.01 V and 3.0 V are as shown in Figure 7.8 a and b, respectively. The voltage curves of Sb_2S_3@RGO electrodes in sodium cells also show large hysteresis between charge and discharge steps, but their plateaus are shorter compared with that in lithium cells. The reversible capacities and coulombic efficiency data under constant current are presented in Figure 7.8 c and d. The Sb_2S_3@RGO composite electrode achieved a high discharge specific capacity of 808 mAh/g and a reversible charge capacity of 570 mAh/g at the initial cycle under 50 mA/g current density between 0.01 V and 2.0 V, which gives a coulombic efficiency of 70.54 %. In the second cycle, the coulombic efficiency of Sb_2S_3@RGO composite electrode rapidly increased to above 95%, and the coulombic efficiency remained above 96% from the 4th cycle to the 100th cycle. The fast increase of coulombic efficiency in sodium cells is most likely the result of FEC electrolyte additive, whose decomposition products play a vital role in stabilizing electrode/electrolyte interphases. After 100 cycles of charge and discharge, the Sb_2S_3@RGO composite electrode was still able to deliver a reversible capacity of 440 mAh/g. However, when the Sb_2S_3@RGO composite electrode was cycled between 0.01 V and 3.0 V, the initial reversible capacity increased to 650 mAh/g. After 54 cycles both the capacities and coulombic efficiencies of electrodes showed an accelerating pattern of fading. As a result, the reversible capacity Sb_2S_3@RGO composite electrodes dropped to 350 mAh/g and the coulombic efficiency reduced to 90% at the 66th cycle, implying severe active material loss.

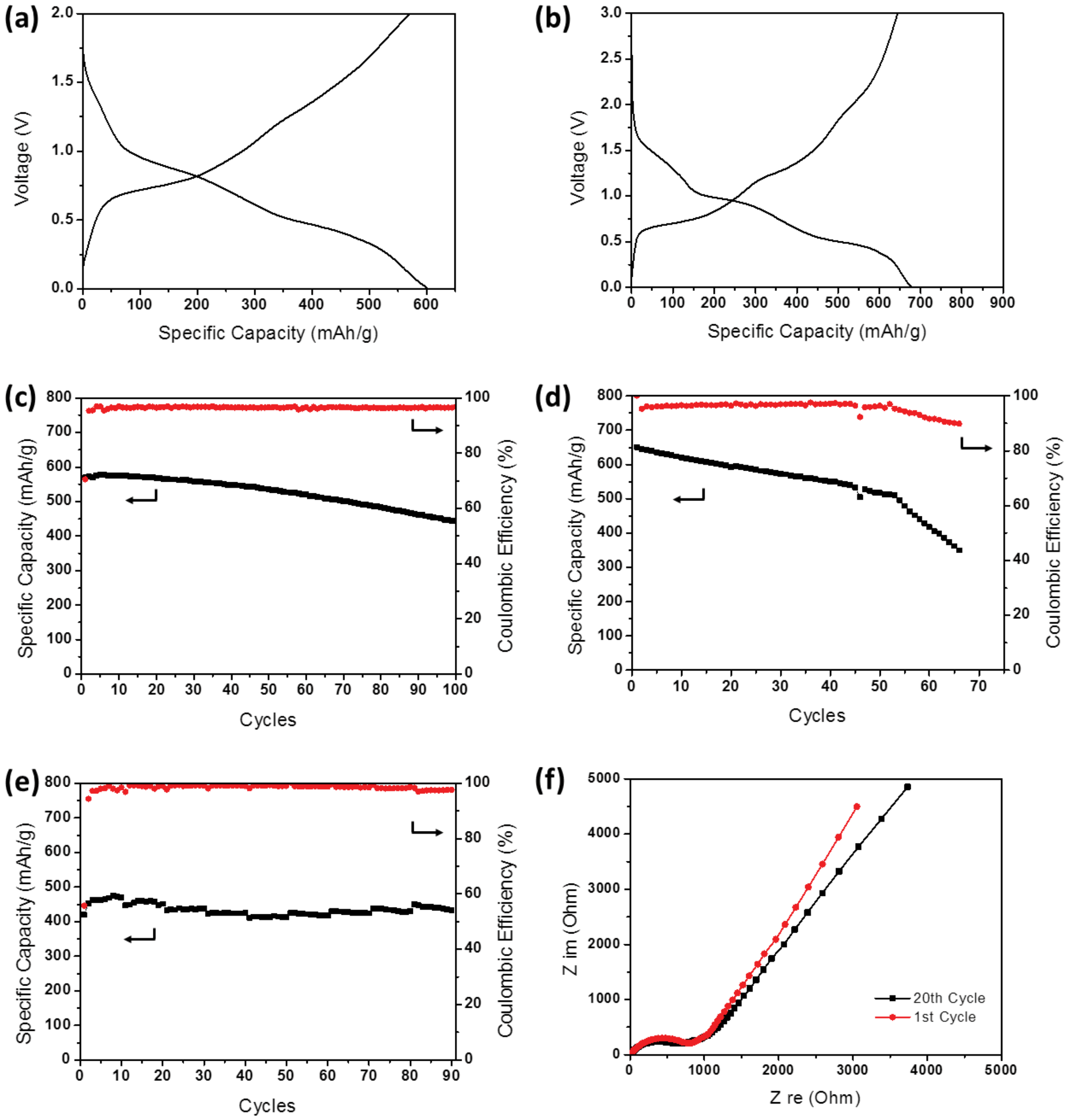

Figure 7.8 Electrochemical characterization results for sodium cells. Voltage profiles of Sb_2S_3@RGO composite in sodium half-cells between 0.01 V and 2.0 V (a), and between 0.01 V and 3.0 V (b). Reversible capacities and coulombic efficiencies of Sb_2S_3@RGO composite electrode in lithium half cells between 0.01 V and 2.0 V (c), and between 0.01 V and 3.0 V (d). Cycling performance of Sb_2S_3@RGO composite electrode at 50 mA/g, 100 mA/g, 200 mA/g, 500 mA/g, 1000 mA/g, and back to 50 mA/g between 0.01 V and 2.0 V (e), Nyquist plots from EIS of sodium cells after the 1st and the 20th cycles at the charged state (f).

The performance deterioration of Sb_2S_3@RGO composite electrodes can be attributed to electrode deformation after repeated liberation and recombination of antimony and sulfur, and the associated large volume change during the alloying reaction between antimony and sodium also leads to pulverization of the electrodes. Considering the larger volume of sodium ions and sodium alloys compared to their lithium analogues, it would be more challenging to maintain good electrical contact of conversion type electrodes in sodium cells than in lithium cells. Figure 7.7e shows the cycle performance of Sb_2S_3@RGO composite electrode at different current rates. Similar to its behavior in lithium cells, the Sb_2S_3@RGO composite electrode also exhibits capacity loss when the current density increased from 50 mA/g to 1A/g between 0.01 V and 2.0 V. The good rate capability of Sb_2S_3@RGO composites in sodium half cells can be attributed to the synergistic effect of both low depth of charge and discharge of cells and the structural features of Sb_2S_3@RGO composite design. The Nyquist plots in Figure 7.8f confirmed the electrode exhibited an enlarged semicircle from the 1st to the 20th cycle, suggesting a gradual increase of the SEI film resistance and the charge transfer resistance with increasing cycles, but the electronic contact within the electrode was well-sustained within the tested range. In general, the reversible capacity from the conversion type metal chalcogenide is higher with reduced particle size. The advantage in the architecture of Sb_2S_3@RGO composites is that it further enhance the reversibility of the conversion reactions of Sb_2S_3 phase by arching the particles on graphene sheet template. The role of graphene on the enhanced electrochemical performance of Sb_2S_3@RGO is positive from two aspects: (i) the conductive graphene layer offers better conductivity between Sb_2S_3 particles compared to the bare Sb_2S_3 electrode, (ii) the graphene template forms a physical barrier to prevent the aggregation of the liberated Sb phase during the sodium insertion process, which is beneficial for the reversibility of Sb_2S_3 conversion reactions.

7.4 Conclusion

In this study, a facile and time-saving synthesis route was developed to produce stibnite/graphene (Sb_2S_3@RGO) composite comprised of orthorhombic phase stibnite nanoparticles which are uniformly dispersed on graphene sheet based carbon matrices. The electrochemical characterization of this composite as an anode material in lithium and sodium half-cells demonstrates a reversible reaction with lithium (sodium) ions, delivering a reversible capacity of 595 mAh/g between 0.01 V and 2.0 V versus lithium, and a reversible capacity of 560 mAh/g between 0.01 V and 2.0 V versus sodium. When the upper cut-off potential increased to 3.0 V, the reversible capacities of this composite electrode can be further extended to 872 mAh/g versus lithium and 653 mAh/g versus sodium, respectively. The enhanced electrochemical behavior of stibnite/graphene composite is attributed to the well dispersed Sb_2S_3 nanoparticles on conductive graphene sheets, which helped maintaining the conductive networks in active phases as well as keeping the structure integrity of electrode. This material also showed low initial coulombic efficiency, high average voltage and large voltage hysteresis between charge and discharge process. All of which may prohibit its practical applications as the negative electrode for lithium and sodium batteries. Nevertheless, the excellent rate performance of Sb_2S_3@RGO electrode highlighted the advantages of composite design with graphene as the conductive substrate. The uniform distribution of nanoparticles on graphene can be obtained via the facile solvothermal method, which makes it a very attractive synthesis approach for a variety of functional materials.

Chapter 8 Conclusions

8.1 Conclusions

This research project aimed at materials synthesis approaches with electrospinning technique and microwave-assisted solvothermal routes for electrode materials preparation. The electrospinning technique is a dynamic synthesis process to generate cylindrical shape polymer fibers and subsequently, carbon based composite fibers with typical diameters of a few hundreds of nanometers. The quality of electrospun polymer fibers was highly dependent on a variety of factors including, but not limited to, the type of polymer and solvent chosen for the precursor solution, solution concentration, solution feeding speed, applied voltage, and ambient conditions, etc. and the optimal process window must be determined by intelligent experimental design for individual electrospinning systems. The microwave-assisted solvothermal synthesis route offered a facile material preparation approach for the metal chalcogenides deposition on graphene sheets, and the morphology of resultant composite material could be easily manipulated by adjusting precursor solution concentration, reaction temperature, reaction time, and the upper limit of reaction pressure. The polyacrylonitrile derived carbon fibers and antimony-carbon fiber/graphene composite obtained with electrospinning process and subsequent thermal pyrolysis process, and solvothermal synthesized antimony sulfide/graphene composite material were investigated as the electrode materials in lithium and sodium cells, respectively. The major research outcomes of this project are summarized below:

1. For electrospinning polymer fiber synthesis, the concentration of polymer solution and applied voltage were found to be critical process parameter that affect the quality of resultant electrospun fibers. With high temperature pyrolysis,

electrospun polyacrylonitrile fibers could be converted to carbon fibers, while the polyvinyl alcohol fibers failed to maintain their original structure under similar conditions. After pyrolysis in inert gas atmosphere, a free-standing sheet comprised of polyacrylonitrile derived carbon fibers was obtained. The carbon fiber electrode achieved stable reversible capacities of 118 mAh/g and 84 mAh/g versus lithium and sodium at a 50 mA/g current density, respectively. The conductive carbon fiber sheet is an attractive material for the synthesis of composite electrode materials due to its conductivity, high specific surface area and high porosity. However, the carbon fiber electrodes also exhibited poor initial coulombic efficiency (< 70%) due to its large surface area, which greatly impedes their applications in batteries.

2. The electrochemical performance of antimony-embedded carbon fibers/reduced graphene oxide (Sb-CF/RGO) composite was investigated as alloy type negative electrode materials for lithium and sodium secondary batteries. The free-standing composite electrodes delivered high reversible capacities (562 mAh/g versus Li and 371 mAh/g versus Na) as well as good capacity retention over 100 cycles under mild charge/discharge conditions (50~100 mA/g) versus both lithium and sodium counter electrodes. The Sb-CF/RGO composite contains 15.07% antimony nanoparticles in weight, but its reversible capacities versus lithium and sodium greatly increased compared with pristine carbon fibers electrode converted from polyacrylonitrile. The utilization of small amount flexible RGO in the composite offered advantages including enhanced structural stability as well as good electrical contact within the electrode. The nanoscale antimony particles inside carbon fibers also induce less stress upon repeated alloy/de-alloy process. As a result, the composite electrode can maintain a

stable charge-discharge behavior under high current density up to 1000 mA/g. However, the low initial coulombic efficiency and large irreversible capacities and during charge-discharge cycling of these composite materials also implies remaining difficulties for the implementation of these materials as practical anode materials for lithium and sodium-ion batteries.

3. A polysulfide viscous solution percolated porous carbon sheet was used as a semi-liquid composite positive electrode for Li-S cells. The highly porous structure from stacks of carbon fibers offered high free volume and high surface area to absorb/adsorb polysulfide solutions, and the conductive PAN-derived carbon fibers also provided large numbers of electrochemically active sites for Li/S redox reactions. The lithium-sulfur cells demonstrated a high reversible capacity of 1010 mAh/g at a constant 1000 mA/g charge-discharge current after 120 cycles. However, limited by the cell chemistry, the detrimental effects of polysulfide species remain a cause of capacity loss. This problem has not yet been properly addressed despite the cycle life of Li anodes in Li-S cells being greatly extended with $LiNO_3$ electrolyte additive. Nevertheless, the tested Li-S cell is still remote from practical battery applications as its overall coulombic efficiencies were below 98% and gradually decrease after prolonged cycling. The poor cycling efficiency will be a major factor that hampers the transformation of Li-S cell from a conceptual design into a practical battery technology.
4. The stibnite (Sb_2S_3)/graphene composite comprising orthorhombic phase stibnite nanoparticles which are uniformly dispersed on graphene sheets based carbon matrices was synthesized with a facile solvothermal synthesis route. The composite electrode exhibited high reversible capacities (595 mAh/g versus

lithium and 560 mAh/g versus sodium) in both lithium and sodium cells. The reversible capacities of this composite electrode can be further extended to 872 mAh/g versus lithium and 651 mAh/g versus sodium by increase the upper cut-off potential to 3.0 V. The enhanced electrochemical behavior of stibnite/graphene composite is attributed to the well dispersed Sb_2S_3 nanoparticles on conductive graphene sheets, which helped maintaining the conductive networks to active phase as well as the structure integrity of electrodes when the Sb_2S_3 nanoparticles react with lithium and sodium ions through conversion reactions. In addition, the excellent rate performance of stibnite/graphene composite also highlights the advantages of microwave-assisted solvothermal method in the preparation of uniform morphology graphene composite materials containing metal chalcogenides, which is attractive for the synthesis of a variety of functional materials. Nevertheless, this material also suffers from a low initial coulombic efficiency, high average voltage, and large voltage hysteresis upon charging. All of this leads to relatively poor combined electrochemical properties to serve as negative electrodes for lithium or sodium secondary batteries, as it will greatly impede the achievable energy in cells with charge balanced designs.

The main effort in this research was devoted to the improved of specific capacities and the rate capabilities of electrode materials via novel designs of nanoarchitectures. The results are very appealing as most of synthesized electrode presented in this thesis have demonstrated high capacities at fast charge-discharge conditions. However, these electrodes being studied failed to demonstrate a coulombic efficiency value within the acceptable range (> 99.9%) for long-term cycling. The decrease of cycling efficiency is attributed to parasitic reactions on electrode/electrolyte interphases and involve both electrode and electrolyte materials, and implies accumulative irreversible capacities of electrode over each charge-discharge cycle, which leads to further penalties in achievable energy of cells. The lithium-sulfur batteries with electrospun carbon fiber as cathode substrate exhibited both high capacities and good rate capabilities. The main disadvantage of semi-liquid cathode (catholyte) design is that the high porous structure carbon fiber membrane and its cut-off voltage of lithium-sulfur batteries, both of which have limited the achievable energy of lithium sulfur batteries. The coulombic efficiency of this sulfur cathode took more than 5 cycles to maintain stable at about 98%, suggesting it requires more compatible electrolyte solutions that have good passivation properties for the solid-electrolyte interphase. Many aspects of the reaction mechanisms in these materials are not fully understood. The irreversible capacity loss is common issue observed in those electrode materials, which can be attributed to unstable SEI films over the large surface area of electrodes. The solution to this issue requires more research and better understanding of reaction mechanisms on the electrode/electrolyte interphase.

8.2 Future perspectives

The lessons learn from the development of lithium-ion batteries is very useful in the search for new electrode materials as well as new battery chemistry. The great success of commercial lithium-ion batteries inspired massive research efforts in the development of commercial sodium-ion batteries which are also operating based on intercalation chemistry. Sodium is one of the most abundant element in Earth’s crust and sea, therefore the sodium-ion battery technology is believed to be a low cost solution for large scale electrochemical energy storage systems. Although the research of electrode materials have showed some promises, further in-depth understanding of the reaction mechanisms and innovative design of electrode materials for sodium-ion batteries are essential because the electrochemical performance of sodium-ion batteries must be improved to meet the demands of battery applications. In addition, the development of Na-ion batteries are facing more technical barriers compared with lithium-ion batteries despite their similarities in battery chemistry.

Bibliography

1. Jasinski, R. *High-Energy Batteries*. (Plenum Press, 1969).
2. Aurbach, D. Review of selected electrode solution interactions which determine the performance of Li and Li-ion batteries. *J. Power Sources* **89,** 206–218 (2000).
3. Brandt, K. Historical development of secondary lithium batteries. *Solid State Ionics* **69,** 173–183 (1994).
4. Zuckerbrod, D.; Giovannoni, R.T.; Grossman, K. R. Life, performance and safety of Grace rechargeable lithium-titanium disulfide cells. *Proc. 34th Int. Power Sources Symp.* 172–175 (1990).
5. Whittingham, M. S. Lithium Batteries and Cathode Materials. *Chem. Rev.* **104,** 4271–4302 (2004).
6. Whittingham, M. S. Electrical energy storage and intercalation chemistry. *Science* **192,** 1126–1127 (1976).
7. Py, M. A. & Haering, R. R. Structural destabilization induced by lithium intercalation in MoS2 and related compounds. *Can. J. Phys.* **61,** 76–84 (1983).
8. Peled, E. *Lithium batteries*. (Academic Press, 1983).
9. Laman, F. C. & Brandt, K. Effect of discharge current on cycle life of a rechargeable lithium battery. *J. Power Sources* **24,** 195–206 (1988).
10. Laman, F. C., Stiles, J. A. R., Shank, R. J. & Brandt, K. Rate limiting mechanisms in lithium—molybdenum disulfide batteries. *J. Power Sources* **14,** 201–207 (1985).
11. Di Pietro, B., Patriarca, M. & Scrosati, B. On the use of rocking chair configurations for cyclable lithium organic electrolyte batteries. *J. Power Sources* **8,** 289–299 (1982).
12. Bittihn, R., Herr, R. & Hoge, D. The SWING system, a nonaqueous rechargeable carbon/metal oxide cell. *J. Power Sources* **43,** 223–231 (1993).
13. Auborn, J. J. & Barberio, Y. L. Lithium Intercalation Cells Without Metallic

Lithium: $MoO_2/LiCoO_2$ and $WO_2/LiCoO_2$. *J. Electrochem. Soc.* **134,** 638–641 (1987).

14. Fong, R., von Sacken, U. & Dahn, J. R. Studies of Lithium Intercalation into Carbons Using Nonaqueous Electrochemical Cells. *J. Electrochem. Soc.* **137,** 2009–2013 (1990).

15. Dahn, J. R., Von Sacken, U., Juzkow, M. W. & Al-Janaby, H. Rechargeable LiNiO2/carbon cells. *J. Electrochem. Soc.* **138,** 2207–2211 (1991).

16. Simon, B., Boeuve, J. P. & Broussely, M. Electrochemical study of the passivating layer on lithium intercalated carbon electrodes in nonaqueous solvents. *J. Power Sources* **43,** 65–74 (1993).

17. (Youngman) Chusid, O., Ein Ely, E., Aurbach, D., Babai, M. & Carmeli, Y. Electrochemical and spectroscopic studies of carbon electrodes in lithium battery electrolyte systems. *J. Power Sources* **43,** 47–64 (1993).

18. Sekai, K. *et al.* Lithium-ion rechargeable cells with $LiCoO_2$ and carbon electrodes. *J. Power Sources* **43,** 241–244 (1993).

19. Tarascon, J. M. & Armand, M. Issues and challenges facing rechargeable lithium batteries. *Nature* **414,** 359–367 (2001).

20. Mizushima, K., Jones, P. C., Wiseman, P. J. & Goodenough, J. B. Li_xCoO_2 ($0<x<-1$): A new cathode material for batteries of high energy density. *Mater. Res. Bull.* **15,** 783–789 (1980).

21. Reimers, J. N. Electrochemical and In Situ X-Ray Diffraction Studies of Lithium Intercalation in LixCoO2. *J. Electrochem. Soc.* **139,** 2091 (1992).

22. DAHN, J., FULLER, E., OBROVAC, M. & VONSACKEN, U. Thermal stability of $LixCoO_2$, Li_xNiO_2 and λ-MnO_2 and consequences for the safety of Li-ion cells. *Solid State Ionics* **69,** 265–270 (1994).

23. Alcántara, R. *et al.* X-ray diffraction, ^{57}Fe Mössbauer and step potential electrochemical spectroscopy study of $LiFe_yCo_{1-y}O_2$ compounds. *J. Power Sources* **81–82,** 547–553 (1999).

24. Madhavi, S., Subba Rao, G. V, Chowdari, B. V. R. & Li, S. F. Y. Effect of Cr dopant on the cathodic behavior of $LiCoO_2$. *Electrochim. Acta* **48,** 219–226 (2002).

25. Stoyanova, R., Zhecheva, E. & Zarkova, L. Effect of Mn-substitution for Co on the crystal structure and acid delithiation of $LiMn_yCo_{1-y}O_2$ solid solutions. *Solid State Ionics* **73,** 233–240 (1994).

26. Scott, I. D. *et al.* Ultrathin Coatings on Nano-$LiCoO_2$ for Li-Ion Vehicular Applications. *Nano Lett.* **11,** 414–418 (2011).

27. Jain, A. *et al.* Commentary: The materials project: A materials genome approach to accelerating materials innovation. *APL Mater.* **1,** (2013).

28. Kalaiselvi, P. K. and N. Various aspects of $LiNiO_2$ chemistry: A review. *Sci. Technol. Adv. Mater.* **6,** 689 (2005).

29. Bloom, I. *et al.* Effect of cathode composition on capacity fade, impedance rise and power fade in high-power, lithium-ion cells. *J. Power Sources* **124,** 538–550 (2003).

30. Yabuuchi, N. & Ohzuku, T. Novel lithium insertion material of $LiCo_{1/3}Ni_{1/3}Mn_{1/3}O_2$ for advanced lithium-ion batteries. *J. Power Sources* **119–121,** 171–174 (2003).

31. Shaju, K. M. & Bruce, P. G. Macroporous $Li(Ni_{1/3}Co_{1/3}Mn_{1/3})O_2$: A High-Power and High-Energy Cathode for Rechargeable Lithium Batteries. *Adv. Mater.* **18,** 2330–2334 (2006).

32. Noh, H.-J., Youn, S., Yoon, C. S. & Sun, Y.-K. Comparison of the structural and electrochemical properties of layered $Li[Ni_xCo_yMn_z]O_2$ (x = 1/3, 0.5, 0.6, 0.7, 0.8 and 0.85) cathode material for lithium-ion batteries. *J. Power Sources* **233,** 121–130 (2013).

33. Gu, M. *et al.* Formation of the Spinel Phase in the Layered Composite Cathode Used in Li-Ion Batteries. *ACS Nano* **7,** 760–767 (2013).

34. Rossen, E., Jones, C. D. W. & Dahn, J. R. Structure and electrochemistry of $Li_xMnyNi_{1-y}O_2$. *Solid State Ionics* **57,** 311–318 (1992).

35. Thackeray, M. M. *et al.* Spinel Electrodes from the Li-Mn-O System for Rechargeable Lithium Battery Applications. *J. Electrochem. Soc.* **139,** 363–366 (1992).

36. Gowda, S. R. *et al.* Oxidation state of cross-over manganese species on the graphite electrode of lithium-ion cells. *Phys. Chem. Chem. Phys.* **16,** 6898–6902 (2014).

37. Padhi, A. K., Nanjundaswamy, K. S. & Goodenough, J. B. Phospho-olivines as Positive-Electrode Materials for Rechargeable Lithium Batteries. *J. Electrochem. Soc.* **144,** 1188–1194 (1997).

38. Nitta, N., Wu, F., Lee, J. T. & Yushin, G. Li-ion battery materials: present and future. *Mater. Today* **18,** 252–264 (2015).

39. Delacourt, C. *et al.* Toward Understanding of Electrical Limitations (Electronic, Ionic) in $LiMPO_4$ (M = Fe , Mn) Electrode Materials. *J. Electrochem. Soc.* **152,** A913–A921 (2005).

40. Okada, S. *et al.* Cathode properties of phospho-olivine $LiMPO_4$ for lithium secondary batteries. *J. Power Sources* **97–98,** 430–432 (2001).

41. Huang, H., Yin, S.-C., Kerr, T., Taylor, N. & Nazar, L. F. Nanostructured Composites: A High Capacity, Fast Rate $Li_3V_2(PO_4)_3$/Carbon Cathode for Rechargeable Lithium Batteries. *Adv. Mater.* **14,** 1525–1528 (2002).

42. Wolfenstine, J. & Allen, J. $LiNiPO_4$–$LiCoPO_4$ solid solutions as cathodes. *J. Power Sources* **136,** 150–153 (2004).

43. Gwon, H., Seo, D.-H., Kim, S.-W., Kim, J. & Kang, K. Combined First-Principle Calculations and Experimental Study on Multi-Component Olivine Cathode for Lithium Rechargeable Batteries. *Adv. Funct. Mater.* **19,** 3285–3292 (2009).

44. Recham, N. *et al.* A 3.6 V lithium-based fluorosulphate insertion positive electrode for lithium-ion batteries. *Nat. Mater.* **9,** 68–74 (2010).

45. Barker, J., Saidi, M. Y. & Swoyer, J. L. Electrochemical Insertion Properties of the Novel Lithium Vanadium Fluorophosphate, $LiVPO_4F$. *J. Electrochem. Soc.* **150,** A1394–A1398 (2003).

46. Qi, Y., Guo, H., Hector, L. G. & Timmons, A. Threefold Increase in the Young's Modulus of Graphite Negative Electrode during Lithium Intercalation. *J. Electrochem. Soc.* **157,** A558 (2010).

47. Bar-Tow, D. A Study of Highly Oriented Pyrolytic Graphite as a Model for the Graphite Anode in Li-Ion Batteries. *J. Electrochem. Soc.* **146,** 824 (1999).

48. Dahn, J. R., Zheng, T., Liu, Y. & Xue, J. S. Mechanisms for Lithium Insertion in Carbonaceous Materials. *Sci.* **270,** 590–593 (1995).

49. Winter, M., Besenhard, J. O., Spahr, M. E. & Novák, P. Insertion Electrode Materials for Rechargeable Lithium Batteries. *Adv. Mater.* **10,** 725–763 (1998).

50. He, Y.-B. *et al.* Effect of solid electrolyte interface (SEI) film on cyclic performance of $Li_4Ti_5O_{12}$ anodes for Li ion batteries. *J. Power Sources* **239,** 269–276 (2013).

51. Song, M.-S. *et al.* Is $Li_4Ti_5O_{12}$ a solid-electrolyte-interphase-free electrode material in Li-ion batteries: Reactivity between the $Li_4Ti_5O_{12}$ electrode and electrolyte. *J. Mater. Chem. A* **2,** 631–636 (2014).

52. Obrovac, M. N. & Christensen, L. Structural Changes in Silicon Anodes during Lithium Insertion/Extraction. *Electrochem. Solid-State Lett.* **7,** A93–A96 (2004).

53. Obrovac, M. N. & Krause, L. J. Reversible Cycling of Crystalline Silicon Powder. *J. Electrochem. Soc.* **154,** A103–A108 (2007).

54. Hochgatterer, N. S. *et al.* Silicon/Graphite Composite Electrodes for High-Capacity Anodes: Influence of Binder Chemistry on Cycling Stability. *Electrochem. Solid-State Lett.* **11,** A76–A80 (2008).

55. Obrovac, M. N., Christensen, L., Le, D. B. & Dahn, J. R. Alloy Design for Lithium-Ion Battery Anodes. *J. Electrochem. Soc.* **154,** A849–A855 (2007).

56. Tao, H.-C., Fan, L.-Z. & Qu, X. Facile synthesis of ordered porous Si@C nanorods as anode materials for Li-ion batteries. *Electrochim. Acta* **71,** 194–200 (2012).

57. Fan, Q., Chupas, P. J. & Whittingham, M. S. Characterization of Amorphous and

Crystalline Tin–Cobalt Anodes. *Electrochem. Solid-State Lett.* **10,** A274–A278 (2007).

58. Ferguson, P. P., Martine, M. L., Dunlap, R. A. & Dahn, J. R. Structural and electrochemical studies of (SnxCo1−x)60C40 alloys prepared by mechanical attriting. *Electrochim. Acta* **54,** 4534–4539 (2009).

59. Foster, D., Wolfstein, J., Read, J. & Allen, J. L. *Performance of Sony's Alloy Based Li-ion Battery*. (2008). at <http://www.dtic.mil/dtic/tr/fulltext/u2/a484773.pdf>

60. Komaba, S. *et al.* Comparative Study of Sodium Polyacrylate and Poly(vinylidene fluoride) as Binders for High Capacity Si–Graphite Composite Negative Electrodes in Li-Ion Batteries. *J. Phys. Chem. C* **116,** 1380–1389 (2012).

61. Bridel, J.-S., Azaïs, T., Morcrette, M., Tarascon, J.-M. & Larcher, D. In Situ Observation and Long-Term Reactivity of Si/C/CMC Composites Electrodes for Li-Ion Batteries. *J. Electrochem. Soc.* **158,** A750–A759 (2011).

62. Lestriez, B., Bahri, S., Sandu, I., Roué, L. & Guyomard, D. On the binding mechanism of CMC in Si negative electrodes for Li-ion batteries. *Electrochem. commun.* **9,** 2801–2806 (2007).

63. Liu, W.-R., Yang, M.-H., Wu, H.-C., Chiao, S. M. & Wu, N.-L. Enhanced Cycle Life of Si Anode for Li-Ion Batteries by Using Modified Elastomeric Binder. *Electrochem. Solid-State Lett.* **8,** A100–A103 (2005).

64. Nakai, H., Kubota, T., Kita, A. & Kawashima, A. Investigation of the Solid Electrolyte Interphase Formed by Fluoroethylene Carbonate on Si Electrodes. *J. Electrochem. Soc.* **158,** A798–A801 (2011).

65. Elazari, R. *et al.* Li Ion Cells Comprising Lithiated Columnar Silicon Film Anodes, TiS2 Cathodes and Fluoroethyene Carbonate (FEC) as a Critically Important Component. *J. Electrochem. Soc.* **159,** A1440–A1445 (2012).

66. Choi, N.-S., Yew, K. H., Kim, H., Kim, S.-S. & Choi, W.-U. Surface layer formed on silicon thin-film electrode in lithium bis(oxalato) borate-based electrolyte. *J. Power Sources* **172,** 404–409 (2007).

67. Philippe, B. *et al.* Improved Performances of Nanosilicon Electrodes Using the Salt LiFSI: A Photoelectron Spectroscopy Study. *J. Am. Chem. Soc.* **135,** 9829–9842 (2013).

68. Choi, N.-S. *et al.* Effect of fluoroethylene carbonate additive on interfacial properties of silicon thin-film electrode. *J. Power Sources* **161,** 1254–1259 (2006).

69. Elazari, R. *et al.* Li Ion Cells Comprising Lithiated Columnar Silicon Film Anodes, TiS2 Cathodes and Fluoroethyene Carbonate (FEC) as a Critically Important Component. *J. Electrochem. Soc.* **159,** A1440–A1445 (2012).

70. Nie, M., Abraham, D. P., Chen, Y., Bose, A. & Lucht, B. L. Silicon Solid Electrolyte Interphase (SEI) of Lithium Ion Battery Characterized by Microscopy and Spectroscopy. *J. Phys. Chem. C* **117,** 13403–13412 (2013).

71. Beattie, S. D., Hatchard, T., Bonakdarpour, A., Hewitt, K. C. & Dahn, J. R. Anomalous, High-Voltage Irreversible Capacity in Tin Electrodes for Lithium Batteries. *J. Electrochem. Soc.* **150,** A701–A705 (2003).

72. Bridel, J.-S. *et al.* Decomposition of ethylene carbonate on electrodeposited metal thin film anode. *J. Power Sources* **195,** 2036–2043 (2010).

73. Idota, Y., Kubota, T., Matsufuji, A., Maekawa, Y. & Miyasaka, T. Tin-based amorphous oxide: a high capacity lithium-ion storage material. *Science (80-.).* **276,** 1395–1397 (1997).

74. Courtney, I. A. & Dahn, J. R. Electrochemical and In Situ X-Ray Diffraction Studies of the Reaction of Lithium with Tin Oxide Composites. *J. Electrochem. Soc.* **144,** 2045 (1997).

75. Tarascon, J., Poizot, P., Laruelle, S., Grugeon, S. & Dupont, L. Nano-sized transition-metal oxides as negative-electrode materials for lithium-ion batteries. *Nature* **407,** 496–499 (2000).

76. Martos, M., Morales, J. & Sánchez, L. Lead-based systems as suitable anode materials for Li-ion batteries. *Electrochim. Acta* **48,** 615–621 (2003).

77. Sarradin, J., Ribes, M., Guessous, A. & Elkacemi, K. Study of Fe2O3-based thin

film electrodes for lithium-ion batteries. *Solid State Ionics* **112,** 35–40 (1998).

78. Morzilli, S. & Scrosati, B. Iron oxide electrodes in lithium organic electrolyte rechargeable batteries. *Electrochim. Acta* **30,** 1271–1276 (1985).

79. Chen, J., Xu, L., Li, W. & Gou, X. α-Fe_2O_3 Nanotubes in Gas Sensor and Lithium-Ion Battery Applications. *Adv. Mater.* **17,** 582–586 (2005).

80. Jiao, F., Bao, J. & Bruce, P. G. Factors Influencing the Rate of Fe_2O_3 Conversion Reaction. *Electrochem. Solid-State Lett.* **10,** A264–A266 (2007).

81. Zeng, S. *et al.* Hematite Hollow Spindles and Microspheres: Selective Synthesis, Growth Mechanisms, and Application in Lithium Ion Battery and Water Treatment. *J. Phys. Chem. C* **111,** 10217–10225 (2007).

82. Reddy, M. V. *et al.* α-Fe_2O_3 Nanoflakes as an Anode Material for Li-Ion Batteries. *Adv. Funct. Mater.* **17,** 2792–2799 (2007).

83. NuLi, Y., Zeng, R., Zhang, P., Guo, Z. & Liu, H. Controlled synthesis of α-Fe_2O_3 nanostructures and their size-dependent electrochemical properties for lithium-ion batteries. *J. Power Sources* **184,** 456–461 (2008).

84. Liu, H. *et al.* Electrochemical performance of α-Fe_2O_3 nanorods as anode material for lithium-ion cells. *Electrochim. Acta* **54,** 1733–1736 (2009).

85. Thackeray, M. M., Baker, S. D., Adendorff, K. T. & Goodenough, J. B. Lithium insertion into Co_3O_4: A preliminary investigation. *Solid State Ionics* **17,** 175–181 (1985).

86. Grugeon, S., Laruelle, S., Dupont, L. & Tarascon, J.-M. An update on the reactivity of nanoparticles Co-based compounds towards Li. *Solid State Sci.* **5,** 895–904 (2003).

87. Obrovac, M. N., Dunlap, R. A., Sanderson, R. J. & Dahn, J. R. The Electrochemical Displacement Reaction of Lithium with Metal Oxides. *J. Electrochem. Soc.* **148,** A576–A588 (2001).

88. Choi, H. C. *et al.* Local Structural Characterization for Electrochemical Insertion−Extraction of Lithium into CoO with X-ray Absorption Spectroscopy. *J.*

Phys. Chem. B **106,** 9252–9260 (2002).

89. Dedryvère, R. *et al.* Contribution of X-ray Photoelectron Spectroscopy to the Study of the Electrochemical Reactivity of CoO toward Lithium. *Chem. Mater.* **16,** 1056–1061 (2004).

90. Do, J.-S. & Weng, C.-H. Preparation and characterization of CoO used as anodic material of lithium battery. *J. Power Sources* **146,** 482–486 (2005).

91. Lou, X. W., Deng, D., Lee, J. Y., Feng, J. & Archer, L. A. Self-Supported Formation of Needlelike Co_3O_4 Nanotubes and Their Application as Lithium-Ion Battery Electrodes. *Adv. Mater.* **20,** 258–262 (2008).

92. Yao, W., Yang, J., Wang, J. & Nuli, Y. Multilayered Cobalt Oxide Platelets for Negative Electrode Material of a Lithium-Ion Battery. *J. Electrochem. Soc.* **155,** A903–A908 (2008).

93. Larcher, D., Sudant, G., Leriche, J.-B., Chabre, Y. & Tarascon, J.-M. The Electrochemical Reduction of Co_3O_4 in a Lithium Cell . *J. Electrochem. Soc.* **149,** A234–A241 (2002).

94. Yuan, Z., Huang, F., Feng, C., Sun, J. & Zhou, Y. Synthesis and electrochemical performance of nanosized Co_3O_4. *Mater. Chem. Phys.* **79,** 1–4 (2003).

95. Du, N. *et al.* Porous Co_3O_4 Nanotubes Derived From $Co_4(CO)_{12}$ Clusters on Carbon Nanotube Templates: A Highly Efficient Material For Li-Battery Applications. *Adv. Mater.* **19,** 4505–4509 (2007).

96. Binotto, G. *et al.* Synthesis, Characterization, and Li-Electrochemical Performance of Highly Porous Co_3O_4 Powders. *Chem. Mater.* **19,** 3032–3040 (2007).

97. Nam, K. T. *et al.* Virus-Enabled Synthesis and Assembly of Nanowires for Lithium Ion Battery Electrodes. *Sci.* **312,** 885–888 (2006).

98. Shaju, K. M., Jiao, F., Debart, A. & Bruce, P. G. Mesoporous and nanowire Co_3O_4 as negative electrodes for rechargeable lithium batteries. *Phys. Chem. Chem. Phys.* **9,** 1837–1842 (2007).

99. Lou, X. W., Deng, D., Lee, J. Y. & Archer, L. A. Thermal formation of mesoporous single-crystal Co_3O_4 nano-needles and their lithium storage properties. *J. Mater. Chem.* **18,** 4397–4401 (2008).

100. Li, Y., Tan, B. & Wu, Y. Mesoporous Co_3O_4 Nanowire Arrays for Lithium Ion Batteries with High Capacity and Rate Capability. *Nano Lett.* **8,** 265–270 (2008).

101. Liu, B. *et al.* Converting cobalt oxide subunits in cobalt metal-organic framework into agglomerated Co_3O_4 nanoparticles as an electrode material for lithium ion battery. *J. Power Sources* **195,** 857–861 (2010).

102. Fu, Z.-W., Wang, Y., Zhang, Y. & Qin, Q.-Z. Electrochemical reaction of nanocrystalline Co_3O_4 thin film with Lithium. *Solid State Ionics* **170,** 105–109 (2004).

103. Podhájecký, P. *et al.* The influence of preparation conditions on the electrochemical behaviour of CuO in a Li/CuO cell. *J. Power Sources* **14,** 269–275 (1985).

104. Grugeon, S. *et al.* Particle Size Effects on the Electrochemical Performance of Copper Oxides toward Lithium. *J. Electrochem. Soc.* **148,** A285–A292 (2001).

105. Débart, A., Dupont, L., Poizot, P., Leriche, J.-B. & Tarascon, J. M. A Transmission Electron Microscopy Study of the Reactivity Mechanism of Tailor-Made CuO Particles toward Lithium. *J. Electrochem. Soc.* **148,** A1266–A1274 (2001).

106. Morales, J., Sánchez, L., Martín, F., Ramos-Barrado, J. R. & Sánchez, M. Nanostructured CuO thin film electrodes prepared by spray pyrolysis: a simple method for enhancing the electrochemical performance of CuO in lithium cells. *Electrochim. Acta* **49,** 4589–4597 (2004).

107. Hu, J., Li, H. & Huang, X. Cr_2O_3-Based Anode Materials for Li-Ion Batteries . *Electrochem. Solid-State Lett.* **8,** A66–A69 (2005).

108. Hu, J., Li, H., Huang, X. & Chen, L. Improve the electrochemical performances of Cr_2O_3 anode for lithium ion batteries. *Solid State Ionics* **177,** 2791–2799 (2006).

109. Dupont, L., Grugeon, S., Laruelle, S. & Tarascon, J.-M. Structure, texture and reactivity versus lithium of chromium-based oxides films as revealed by TEM investigations. *J. Power Sources* **164,** 839–848 (2007).

110. Dupont, L. *et al.* Mesoporous Cr_2O_3 as negative electrode in lithium batteries: TEM study of the texture effect on the polymeric layer formation. *J. Power Sources* **175,** 502–509 (2008).

111. Wu, M.-S., Chiang, P.-C. J., Lee, J.-T. & Lin, J.-C. Synthesis of Manganese Oxide Electrodes with Interconnected Nanowire Structure as an Anode Material for Rechargeable Lithium Ion Batteries. *J. Phys. Chem. B* **109,** 23279–23284 (2005).

112. Zhao, J., Tao, Z., Liang, J. & Chen, J. Facile Synthesis of Nanoporous γ-MnO_2 Structures and Their Application in Rechargeable Li-Ion Batteries. *Cryst. Growth Des.* **8,** 2799–2805 (2008).

113. Thackeray, M. M. Manganese oxides for lithium batteries. *Prog. Solid State Chem.* **25,** 1–71 (1997).

114. Poizot, P., Laruelle, S., Grugeon, S. & Tarascon, J.-M. Rationalization of the Low-Potential Reactivity of 3d-Metal-Based Inorganic Compounds toward Li. *J. Electrochem. Soc.* **149,** A1212–A1217 (2002).

115. Fan, Q. & Whittingham, M. S. Electrospun Manganese Oxide Nanofibers as Anodes for Lithium-Ion Batteries. *Electrochem. Solid-State Lett.* **10,** A48–A51 (2007).

116. Chen, C., Ding, N., Wang, L., Yu, Y. & Lieberwirth, I. Some new facts on electrochemical reaction mechanism for transition metal oxide electrodes. *J. Power Sources* **189,** 552–556 (2009).

117. Wang, Y. & Qin, Q.-Z. A Nanocrystalline NiO Thin-Film Electrode Prepared by Pulsed Laser Ablation for Li-Ion Batteries. *J. Electrochem. Soc.* **149,** A873–A878 (2002).

118. Varghese, B. *et al.* Fabrication of NiO Nanowall Electrodes for High Performance Lithium Ion Battery. *Chem. Mater.* **20,** 3360–3367 (2008).

119. Ji, X., Herle, P. S., Rho, Y. & Nazar, L. F. Carbon/MoO_2 Composite Based on Porous Semi-Graphitized Nanorod Assemblies from In Situ Reaction of Tri-Block Polymers. *Chem. Mater.* **19,** 374–383 (2007).

120. Shi, Y. *et al.* Ordered Mesoporous Metallic MoO_2 Materials with Highly Reversible Lithium Storage Capacity. *Nano Lett.* **9,** 4215–4220 (2009).

121. Ku, J. H., Jung, Y. S., Lee, K. T., Kim, C. H. & Oh, S. M. Thermoelectrochemically Activated MoO_2 Powder Electrode for Lithium Secondary Batteries. *J. Electrochem. Soc.* **156,** A688–A693 (2009).

122. Lee, S.-H. *et al.* Reversible Lithium-Ion Insertion in Molybdenum Oxide Nanoparticles. *Adv. Mater.* **20,** 3627–3632 (2008).

123. Jung, Y. S., Lee, S., Ahn, D., Dillon, A. C. & Lee, S.-H. Electrochemical reactivity of ball-milled MoO_{3-y} as anode materials for lithium-ion batteries. *J. Power Sources* **188,** 286–291 (2009).

124. Riley, L. A., Lee, S.-H., Gedvilias, L. & Dillon, A. C. Optimization of MoO_3 nanoparticles as negative-electrode material in high-energy lithium ion batteries. *J. Power Sources* **195,** 588–592 (2010).

125. Balaya, P., Li, H., Kienle, L. & Maier, J. Fully Reversible Homogeneous and Heterogeneous Li Storage in RuO_2 with High Capacity. *Adv. Funct. Mater.* **13,** 621–625 (2003).

126. Fong, R., Dahn, J. R. & Jones, C. H. W. Electrochemistry of Pyrite-Based Cathodes for Ambient Temperature Lithium Batteries. *J. Electrochem. Soc.* **136,** 3206–3210 (1989).

127. Shao-Horn, Y., Osmialowski, S. & Horn, Q. C. Reinvestigation of Lithium Reaction Mechanisms in FeS_2 Pyrite at Ambient Temperature . *J. Electrochem. Soc.* **149,** A1547–A1555 (2002).

128. Gómez-Cámer, J. L., Martin, F., Morales, J. & Sánchez, L. Precipitation of CoS vs Ceramic Synthesis for Improved Performance in Lithium Cells. *J. Electrochem. Soc.* **155,** A189–A195 (2008).

129. Kim, Y. & Goodenough, J. B. Lithium Insertion into Transition-Metal

Monosulfides: Tuning the Position of the Metal 4s Band. *J. Phys. Chem. C* **112,** 15060–15064 (2008).

130. Takeuchi, T., Sakaebe, H., Kageyama, H., Sakai, T. & Tatsumi, K. Preparation of NiS2 Using Spark-Plasma-Sintering Process and Its Electrochemical Properties. *J. Electrochem. Soc.* **155,** A679–A684 (2008).

131. Chung, J.-S. & Sohn, H.-J. Electrochemical behaviors of CuS as a cathode material for lithium secondary batteries. *J. Power Sources* **108,** 226–231 (2002).

132. Cabana, J., Monconduit, L., Larcher, D. & Palacín, M. R. Beyond intercalation-based Li-ion batteries: The state of the art and challenges of electrode materials reacting through conversion reactions. *Adv. Mater.* **22,** 170–192 (2010).

133. Obrovac, M. N. & Chevrier, V. L. Alloy Negative Electrodes for Li-Ion Batteries. *Chem. Rev.* **114,** 11444–11502 (2014).

134. Du, Z., Dunlap, R. A. & Obrovac, M. N. High Energy Density Calendered Si Alloy/Graphite Anodes. *J. Electrochem. Soc.* **161,** A1698–A1705 (2014).

135. Smith, a. J., Burns, J. C., Trussler, S. & Dahn, J. R. Precision Measurements of the Coulombic Efficiency of Lithium-Ion Batteries and of Electrode Materials for Lithium-Ion Batteries. *J. Electrochem. Soc.* **157,** A196 (2010).

136. Etacheri, V., Marom, R., Elazari, R., Salitra, G. & Aurbach, D. Challenges in the development of advanced Li-ion batteries: a review. *Energy Environ. Sci.* **4,** 3243 (2011).

137. Xu, K. Electrolytes and Interphases in Li-Ion Batteries and Beyond. *Chem. Rev.* **114,** 11503–11618 (2014).

138. Linford, R. G. *Electrochemical Science and Technology of Polymers*. (Springer Netherlands, 1990).

139. Dudley, J. T. *et al.* Conductivity of electrolytes for rechargeable lithium batteries. *J. Power Sources* **35,** 59–82 (1991).

140. Xu, K. Nonaqueous Liquid Electrolytes for Lithium-Based Rechargeable Batteries. *Chem. Rev.* **104,** 4303–4418 (2004).

141. Valøen, L. O. & Reimers, J. N. Transport Properties of LiPF6-Based Li-Ion Battery Electrolytes. *J. Electrochem. Soc.* **152,** A882 (2005).

142. Chen, L., Wang, K., Xie, X. & Xie, J. Enhancing Electrochemical Performance of Silicon Film Anode by Vinylene Carbonate Electrolyte Additive. *Electrochem. Solid-State Lett.* **9,** A512–A515 (2006).

143. Li, M.-Q., Qu, M.-Z., He, X.-Y. & Yu, Z.-L. Electrochemical Performance of Si/Graphite/Carbon Composite Electrode in Mixed Electrolytes Containing LiBOB and LiPF6 . *J. Electrochem. Soc.* **156,** A294–A298 (2009).

144. Täubert, C., Fleischhammer, M., Wohlfahrt-Mehrens, M., Wietelmann, U. & Buhrmester, T. LiBOB as Electrolyte Salt or Additive for Lithium-Ion Batteries Based on $LiNi_{0.8}Co_{0.15}Al_{0.05}O_2$ / Graphite. *J. Electrochem. Soc.* **157,** A721–A728 (2010).

145. Dalavi, S., Guduru, P. & Lucht, B. L. Performance Enhancing Electrolyte Additives for Lithium Ion Batteries with Silicon Anodes. *J. Electrochem. Soc.* **159,** A642–A646 (2012).

146. Ji, X. & Nazar, L. F. Advances in Li–S batteries. *J. Mater. Chem.* **20,** 9821 (2010).

147. Danuta, H. & Juliusz, U. Electric dry cells and storage batteries. (1962). at <http://www.google.com/patents/US3043896>

148. Aurbach, D. *et al.* On the Surface Chemical Aspects of Very High Energy Density, Rechargeable Li–Sulfur Batteries. *Journal of The Electrochemical Society* **156,** A694 (2009).

149. Park, J.-W. *et al.* Solvent Effect of Room Temperature Ionic Liquids on Electrochemical Reactions in Lithium–Sulfur Batteries. *J. Phys. Chem. C* **117,** 4431–4440 (2013).

150. Wang, L. & Byon, H. R. N-Methyl-N-propylpiperidinium bis(trifluoromethanesulfonyl)imide-based organic electrolyte for high performance lithium–sulfur batteries. *J. Power Sources* **236,** 207–214 (2013).

151. Ji, X., Lee, K. T. & Nazar, L. F. A highly ordered nanostructured carbon-sulphur

cathode for lithium-sulphur batteries. *Nat. Mater.* **8,** 500–506 (2009).

152. Wang, D.-W. *et al.* A microporous–mesoporous carbon with graphitic structure for a high-rate stable sulfur cathode in carbonate solvent-based Li–S batteries. *Phys. Chem. Chem. Phys.* **14,** 8703 (2012).

153. Zhang, K., Zhao, Q., Tao, Z. & Chen, J. Composite of sulfur impregnated in porous hollow carbon spheres as the cathode of Li-S batteries with high performance. *Nano Res.* **6,** 38–46 (2013).

154. Wang, B. *et al.* Dual protection of sulfur by carbon nanospheres and graphene sheets for lithium-sulfur batteries. *Chem. - A Eur. J.* **20,** 5224–5230 (2014).

155. Nan, C. *et al.* Durable carbon-coated Li_2S core-shell spheres for high performance lithium/sulfur cells. *J. Am. Chem. Soc.* **136,** 4659–4663 (2014).

156. Ding, B. *et al.* Encapsulating sulfur into hierarchically ordered porous carbon as a high-performance cathode for lithium-sulfur batteries. *Chem. - A Eur. J.* **19,** 1013–1019 (2013).

157. Zhao, M. Q. *et al.* Graphene/single-walled carbon nanotube hybrids: One-step catalytic growth and applications for high-rate Li-S batteries. *ACS Nano* **6,** 10759–10769 (2012).

158. Brun, N. *et al.* Hydrothermal carbon-based nanostructured hollow spheres as electrode materials for high-power lithium-sulfur batteries. *Phys. Chem. Chem. Phys.* **15,** 6080–7 (2013).

159. Li, Z. *et al.* Insight into the electrode mechanism in lithium-sulfur batteries with ordered microporous carbon confined sulfur as the cathode. *Adv. Energy Mater.* **4,** 1–8 (2014).

160. Rosenman, a., Elazari, R., Salitra, G., Aurbach, D. & Garsuch, a. Li-S Cathodes with Extended Cycle Life by Sulfur Encapsulation in Disordered Micro-Porous Carbon Powders. *J. Electrochem. Soc.* **161,** A657–A662 (2014).

161. Song, J. *et al.* Nitrogen-doped Mesoporous carbon promoted chemical adsorption of sulfur and fabrication of high-Areal-capacity sulfur cathode with exceptional cycling stability for lithium-sulfur batteries. *Adv. Funct. Mater.* **24,** 1243–1250

(2014).

162. Schuster, J. *et al.* Spherical ordered mesoporous carbon nanoparticles with high porosity for lithium-sulfur batteries. *Angew. Chemie - Int. Ed.* **51,** 3591–3595 (2012).

163. Elazari, R., Salitra, G., Garsuch, A., Panchenko, A. & Aurbach, D. Sulfur-impregnated activated carbon fiber cloth as a binder-free cathode for rechargeable Li-S batteries. *Adv. Mater.* **23,** 5641–5644 (2011).

164. Guo, J., Xu, Y. & Wang, C. Sulfur-impregnated disordered carbon nanotubes cathode for lithium-sulfur batteries. *Nano Lett.* **11,** 4288–4294 (2011).

165. Xiao, L. *et al.* A soft approach to encapsulate sulfur: Polyaniline nanotubes for lithium-sulfur batteries with long cycle life. *Adv. Mater.* **24,** 1176–1181 (2012).

166. Yang, Y. *et al.* Improving the performance of lithium-sulfur batteries by conductive polymer coating. *ACS Nano* **5,** 9187–9193 (2011).

167. Xiao, L. *et al.* Molecular structures of polymer/sulfur composites for lithium-sulfur batteries with long cycle life. *J. Mater. Chem. A* **1,** 9517–9526 (2013).

168. Wu, F. *et al.* Sulfur/polythiophene with a core/shell structure: Synthesis and electrochemical properties of the cathode for rechargeable lithium batteries. *J. Phys. Chem. C* **115,** 6057–6063 (2011).

169. Chen, H., Dong, W., Ge, J., Wang, C. & Wu, X. Ultrafine Sulfur Nanoparticles in Conducting Polymer Shell as Cathode Materials for High Performance Lithium/Sulfur Batteries. *Sci. Rep.* **3,** 1910 (2013).

170. Li, W. *et al.* Understanding the role of different conductive polymers in improving the nanostructured sulfur cathode performance. *Nano Lett.* **13,** 5534–5540 (2013).

171. Ji, X., Evers, S., Black, R. & Nazar, L. F. Stabilizing lithium-sulphur cathodes using polysulphide reservoirs. *Nat. Commun.* **2,** 325 (2011).

172. Evers, S., Yim, T. & Nazar, L. F. Understanding the nature of absorption/adsorption in nanoporous polysulfide sorbents for the Li-S battery. *J.*

Phys. Chem. C **116,** 19653–19658 (2012).

173. Song, M.-S. *et al.* Effects of Nanosized Adsorbing Material on Electrochemical Properties of Sulfur Cathodes for Li/S Secondary Batteries. *J. Electrochem. Soc.* **151,** A791–A795 (2004).

174. Demir-Cakan, R. *et al.* Cathode Composites for Li–S Batteries via the Use of Oxygenated Porous Architectures. *J. Am. Chem. Soc.* **133,** 16154–16160 (2011).

175. Wei Seh, Z. *et al.* Sulphur-TiO_2 yolk-shell nanoarchitecture with internal void space for long-cycle lithium-sulphur batteries. *Nat. Commun.* **4,** 1331 (2013).

176. Bacon, R. F. & Fanelli, R. The Viscosity of Sulfur. *J. Am. Chem. Soc.* **65,** 639–648 (1943).

177. Fu, Y., Su, Y. S. & Manthiram, A. Highly reversible lithium/dissolved polysulfide batteries with carbon nanotube electrodes. *Angew. Chemie - Int. Ed.* **52,** 6930–6935 (2013).

178. Demir Cakan, R. *et al.* Li-S batteries: simple approaches for superior performances. *Energy Environ. Sci.* 176–182 (2012).

179. Kamyshny Alexey, Gun, J., Rizkov, D., Voitsekovski, T. & Lev, O. Equilibrium Distribution of Polysulfide Ions in Aqueous Solutions at Different Temperatures by Rapid Single Phase Derivatization. *Environ. Sci. Technol.* **41,** 2395–2400 (2007).

180. Barchasz, C. *et al.* Lithium/Sulfur Cell Discharge Mechanism: An Original Approach for Intermediate Species Identification. *Anal. Chem.* **84,** 3973–3980 (2012).

181. Read, J. Characterization of the Lithium/Oxygen Organic Electrolyte Battery. *J. Electrochem. Soc.* **149,** A1190–A1195 (2002).

182. Abraham, K. M. & Jiang, Z. A Polymer Electrolyte-Based Rechargeable Lithium/Oxygen Battery. *J. Electrochem. Soc.* **143,** 1–5 (1996).

183. Ogasawara, T., Débart, A., Holzapfel, M., Novák, P. & Bruce, P. G. Rechargeable Li_2O_2 Electrode for Lithium Batteries. *J. Am. Chem. Soc.* **128,**

1390–1393 (2006).

184. Lu, J. *et al.* Aprotic and Aqueous Li–O_2 Batteries. *Chem. Rev.* **114,** 5611–5640 (2014).

185. Balaish, M., Kraytsberg, A. & Ein-Eli, Y. A critical review on lithium-air battery electrolytes. *Phys. Chem. Chem. Phys.* **16,** 2801–22 (2014).

186. Freunberger, S. A. *et al.* Reactions in the Rechargeable Lithium–O_2 Battery with Alkyl Carbonate Electrolytes. *J. Am. Chem. Soc.* **133,** 8040–8047 (2011).

187. McCloskey, B. D., Bethune, D. S., Shelby, R. M., Girishkumar, G. & Luntz, A. C. Solvents' Critical Role in Nonaqueous Lithium–Oxygen Battery Electrochemistry. *J. Phys. Chem. Lett.* **2,** 1161–1166 (2011).

188. Xu, W. *et al.* Reaction mechanisms for the limited reversibility of Li–O_2 chemistry in organic carbonate electrolytes. *J. Power Sources* **196,** 9631–9639 (2011).

189. Takechi, K. *et al.* Stability of Solvents against Superoxide Radical Species for the Electrolyte of Lithium-Air Battery. *ECS Electrochem. Lett.* **1,** A27–A29 (2012).

190. Bryantsev, V. S. & Blanco, M. Computational Study of the Mechanisms of Superoxide-Induced Decomposition of Organic Carbonate-Based Electrolytes. *J. Phys. Chem. Lett.* **2,** 379–383 (2011).

191. Freunberger, S. A. *et al.* The Lithium–Oxygen Battery with Ether-Based Electrolytes. *Angew. Chemie Int. Ed.* **50,** 8609–8613 (2011).

192. Laoire, C., Mukerjee, S., Plichta, E. J., Hendrickson, M. A. & Abraham, K. M. Rechargeable Lithium/TEGDME- $LiPF_6/O_2$ Battery. *J. Electrochem. Soc.* **158,** A302–A308 (2011).

193. Xu, W. *et al.* The stability of organic solvents and carbon electrode in nonaqueous Li-O_2 batteries. *J. Power Sources* **215,** 240–247 (2012).

194. Jung, H.-G., Hassoun, J., Park, J.-B., Sun, Y.-K. & Scrosati, B. An improved high-performance lithium–air battery. *Nat. Chem.* **4,** 579–585 (2012).

195. Laoire, C. O., Mukerjee, S., Abraham, K. M., Plichta, E. J. & Hendrickson, M. A.

Influence of Nonaqueous Solvents on the Electrochemistry of Oxygen in the Rechargeable Lithium−Air Battery. *J. Phys. Chem. C* **114,** 9178–9186 (2010).

196. Peng, Z., Freunberger, S. a., Chen, Y. & Bruce, P. G. A Reversible and Higher-Rate Li-O_2 Battery. *Science (80-.).* **337,** 563–566 (2012).

197. Trahan, M. J., Mukerjee, S., Plichta, E. J., Hendrickson, M. A. & Abraham, K. M. Studies of Li-Air Cells Utilizing Dimethyl Sulfoxide-Based Electrolyte. *J. Electrochem. Soc.* **160,** A259–A267 (2013).

198. Kim, B. G., Lee, J.-N., Lee, D. J., Park, J.-K. & Choi, J. W. Robust Cycling of Li–O_2 Batteries through the Synergistic Effect of Blended Electrolytes. *ChemSusChem* **6,** 443–448 (2013).

199. Hayyan, M. *et al.* Long term stability of superoxide ion in piperidinium, pyrrolidinium and phosphonium cations-based ionic liquids and its utilization in the destruction of chlorobenzenes. *J. Electroanal. Chem.* **664,** 26–32 (2012).

200. De Giorgio, F., Soavi, F. & Mastragostino, M. Effect of lithium ions on oxygen reduction in ionic liquid-based electrolytes. *Electrochem. commun.* **13,** 1090–1093 (2011).

201. Zhang, D., Li, R., Huang, T. & Yu, A. Novel composite polymer electrolyte for lithium air batteries. *J. Power Sources* **195,** 1202–1206 (2010).

202. Kumar, B. *et al.* A Solid-State, Rechargeable, Long Cycle Life Lithium–Air Battery. *J. Electrochem. Soc.* **157,** A50–A54 (2010).

203. Hassoun, J., Croce, F., Armand, M. & Scrosati, B. Investigation of the O_2 Electrochemistry in a Polymer Electrolyte Solid-State Cell. *Angew. Chemie Int. Ed.* **50,** 2999–3002 (2011).

204. Li, F., Kitaura, H. & Zhou, H. The pursuit of rechargeable solid-state Li-air batteries. *Energy Environ. Sci.* **6,** 2302–2311 (2013).

205. Mohamed, S. N., Johari, N. A., Ali, A. M. M., Harun, M. K. & Yahya, M. Z. A. Electrochemical studies on epoxidised natural rubber-based gel polymer electrolytes for lithium–air cells. *J. Power Sources* **183,** 351–354 (2008).

206. Luntz, A. C. & Mccloskey, B. D. Nonaqueous li-air batteries: a status report. *Chem. Rev.* **114,** 11721–11750 (2014).

207. Delmas, C., Braconnier, J.-J., Fouassier, C. & Hagenmuller, P. Electrochemical intercalation of sodium in NaxCoO2 bronzes. *Solid State Ionics* **3,** 165–169 (1981).

208. Kikkawa, S., Miyazaki, S. & Koizumi, M. Sodium deintercalation from α-NaFeO2. *Mater. Res. Bull.* **20,** 373–377 (1985).

209. Shacklette, L. W., Jow, T. R. & Townsend, L. Rechargeable Electrodes from Sodium Cobalt Bronzes. *J. Electrochem. Soc.* **135,** 2669–2674 (1988).

210. van Zyl, A. Review of the zebra battery system development. *Solid State Ionics* **86,** 883–889 (1996).

211. Wen, Z. *et al.* Research on sodium sulfur battery for energy storage. *Solid State Ionics* **179,** 1697–1701 (2008).

212. Yabuuchi, N., Kubota, K., Dahbi, M. & Komaba, S. Research Development on Sodium-Ion Batteries. *Chem. Rev.* **114,** 11636–11682 (2014).

213. Berg, E. J., Villevieille, C., Streich, D., Trabesinger, S. & Novák, P. Rechargeable Batteries: Grasping for the Limits of Chemistry. *J. Electrochem. Soc.* **162,** A2468–A2475 (2015).

214. Gröger, O., Gasteiger, H. A. & Suchsland, J.-P. Review—Electromobility: Batteries or Fuel Cells? *J. Electrochem. Soc.* **162,** A2605–A2622 (2015).

215. Vikström, H., Davidsson, S. & Höök, M. Lithium availability and future production outlooks. *Appl. Energy* **110,** 252–266 (2013).

216. Sonoc, A. & Jeswiet, J. A review of lithium supply and demand and a preliminary investigation of a room temperature method to recycle lithium ion batteries to recover lithium and other materials. *Procedia CIRP* **15,** 289–293 (2014).

217. Grosjean, C., Herrera Miranda, P., Perrin, M. & Poggi, P. Assessment of world lithium resources and consequences of their geographic distribution on the

expected development of the electric vehicle industry. *Renew. Sustain. Energy Rev.* **16,** 1735–1744 (2012).

218. Gruber, P. W. *et al.* Global lithium availability: A constraint for electric vehicles? *J. Ind. Ecol.* **15,** 760–775 (2011).

219. Speirs, J., Contestabile, M., Houari, Y. & Gross, R. The future of lithium availability for electric vehicle batteries. *Renew. Sustain. Energy Rev.* **35,** 183–193 (2014).

220. Whittingham, M. S. Ultimate Limits to Intercalation Reactions for Lithium Batteries. *Chem. Rev.* **114,** 11414–11443 (2014).

221. Palomares, V., Casas-Cabanas, M., Castillo-Martínez, E., Han, M. H. & Rojo, T. Update on Na-based battery materials. A growing research path. *Energy Environ. Sci.* **6,** 2312–2337 (2013).

222. Hong, S. Y. *et al.* Charge carriers in rechargeable batteries: Na ions vs. Li ions. *Energy Environ. Sci.* **6,** 2067–2081 (2013).

223. Han, M. H., Gonzalo, E., Singh, G. & Rojo, T. A comprehensive review of sodium layered oxides: powerful cathodes for Na-ion batteries. *Energy Environ. Sci.* **8,** 81–102 (2015).

224. Stevens, D. a. & Dahn, J. R. High Capacity Anode Materials for Rechargeable Sodium-Ion Batteries. *J. Electrochem. Soc.* **147,** 1271 (2000).

225. Clément, R. J., Bruce, P. G. & Grey, C. P. Review—Manganese-Based P2-Type Transition Metal Oxides as Sodium-Ion Battery Cathode Materials. *J. Electrochem. Soc.* **162,** A2589–A2604 (2015).

226. Pham, Q. P., Sharma, U. & Mikos, A. G. Electrospinning of polymeric nanofibers for tissue engineering applications: a review. *Tissue Eng.* **12,** 1197–211 (2006).

227. Thompson, A. H. Lithium Ordering in Li_xTiS_2. *Phys. Rev. Lett.* **40,** 1511–1514 (1978).

228. Chevrier, V. L. *et al.* Evaluating Si-Based Materials for Li-Ion Batteries in

Commercially Relevant Negative Electrodes. *J. Electrochem. Soc.* **161,** A783–A791 (2014).

229. Fleischauer, M. D., Topple, J. M. & Dahn, J. R. Combinatorial Investigations of Si-M (M = Cr + Ni , Fe , Mn) Thin Film Negative Electrode Materials. *Electrochem. Solid-State Lett.* **8,** A137–A140 (2005).

230. Wu, Q., Lu, W. & Prakash, J. Characterization of a commercial size cylindrical Li-ion cell with a reference electrode. *J. Power Sources* **88,** 237–242 (2000).

231. Thavasi, V., Singh, G. & Ramakrishna, S. Electrospun nanofibers in energy and environmental applications. *Energy Environ. Sci.* **1,** 205 (2008).

232. Teo, W. E. & Ramakrishna, S. A review on electrospinning design and nanofibre assemblies. *Nanotechnology* **17,** R89–R106 (2006).

233. Nataraj, S. K., Yang, K. S. & Aminabhavi, T. M. Polyacrylonitrile-based nanofibers—A state-of-the-art review. *Prog. Polym. Sci.* **37,** 487–513 (2012).

234. Ali, A. a. & El-Hamid, M. a. Electro-spinning optimization for precursor carbon nanofibers. *Compos. Part A Appl. Sci. Manuf.* **37,** 1681–1687 (2006).

235. Mathews, N. *et al.* Oxide nanowire networks and their electronic and optoelectronic characteristics. *Nanoscale* **2,** 1984–98 (2010).

236. Miao, J., Miyauchi, M., Simmons, T. J., Dordick, J. S. & Linhardt, R. J. Electrospinning of Nanomaterials and Applications in Electronic Components and Devices. *J. Nanosci. Nanotechnol.* **10,** 5507–5519 (2010).

237. Reneker, D. H. & Yarin, A. L. Electrospinning jets and polymer nanofibers. *Polymer (Guildf).* **49,** 2387–2425 (2008).

238. Reneker, D. H., Yarin, A. L., Zussman, E. & Xu, H. in (ed. Mechanics, H. A. and E. van der G. B. T.-A. in A.) **Volume 41,** 43–346 (Elsevier, 2007).

239. Persano, L., Camposeo, A., Tekmen, C. & Pisignano, D. Industrial Upscaling of Electrospinning and Applications of Polymer Nanofibers: A Review. *Macromol. Mater. Eng.* **298,** 504–520 (2013).

240. Gu, S. Y., Ren, J. & Wu, Q. L. Preparation and structures of electrospun PAN

nanofibers as a precursor of carbon nanofibers. *Synth. Met.* **155,** 157–161 (2005).

241. Zhang, C., Yuan, X., Wu, L., Han, Y. & Sheng, J. Study on morphology of electrospun poly(vinyl alcohol) mats. *Eur. Polym. J.* **41,** 423–432 (2005).

242. Zhao, Y. Y., Yang, Q. B., Lu, X. F., Wang, C. & Wei, Y. Study on correlation of morphology of electrospun products of polyacrylamide with ultrahigh molecular weight. *J. Polym. Sci. Part B Polym. Phys.* **43,** 2190–2195 (2005).

243. Koski, a., Yim, K. & Shivkumar, S. Effect of molecular weight on fibrous PVA produced by electrospinning. *Mater. Lett.* **58,** 493–497 (2004).

244. Hohman, M. M., Shin, M., Rutledge, G. & Brenner, M. P. Electrospinning and electrically forced jets. II. Applications. *Phys. Fluids* **13,** 2221–2236 (2001).

245. Hohman, M. M., Shin, M., Rutledge, G. & Brenner, M. P. Electrospinning and electrically forced jets. I. Stability theory. *Phys. Fluids* **13,** 2201 (2001).

246. Yao, L. *et al.* Electrospinning and stabilization of fully hydrolyzed poly(vinyl alcohol) fibers. *Chem. Mater.* **15,** 1860–1864 (2003).

247. Yarin, A. L., Koombhongse, S. & Reneker, D. H. Taylor cone and jetting from liquid droplets in electrospinning of nanofibers. *J. Appl. Phys.* **90,** 4836 (2001).

248. Yarin, a. L., Koombhongse, S. & Reneker, D. H. Bending instability in electrospinning of nanofibers. *J. Appl. Phys.* **89,** 3018–3026 (2001).

249. Qian, J. *et al.* High capacity Na-storage and superior cyclability of nanocomposite Sb/C anode for Na-ion batteries. *Chem. Commun.* **48,** 7070 (2012).

250. Darwiche, A. *et al.* Better cycling performances of bulk sb in na-ion batteries compared to li-ion systems: An unexpected electrochemical mechanism. *J. Am. Chem. Soc.* **134,** 20805–20811 (2012).

251. Baggetto, L. *et al.* Intrinsic thermodynamic and kinetic properties of Sb electrodes for Li-ion and Na-ion batteries: experiment and theory. *J. Mater. Chem. A* **1,** 7985 (2013).

252. Zhu, Y. *et al.* Electrospun Sb/C Fibers for a Stable and Fast Sodium-Ion Battery

Anode. *ACS Nano* **7,** 6378–6386 (2013).

253. Zhou, X., Dai, Z., Bao, J. & Guo, Y.-G. Wet milled synthesis of an Sb/MWCNT nanocomposite for improved sodium storage. *J. Mater. Chem. A* **1,** 13727–13731 (2013).

254. Zhou, X. *et al.* Sb nanoparticles decorated N-rich carbon nanosheets as anode materials for sodium ion batteries with superior rate capability and long cycling stability. *Chem. Commun.* **50,** 12888–12891 (2014).

255. Nithya, C. & Gopukumar, S. rGO/nano Sb composite: a high performance anode material for Na+ ion batteries and evidence for the formation of nanoribbons from the nano rGO sheet during galvanostatic cycling. *J. Mater. Chem. A* **2,** 10516–10525 (2014).

256. Xia, X., Obrovac, M. N. & Dahn, J. R. Comparison of the Reactivity of NaxC6 and LixC6 with Non-Aqueous Solvents and Electrolytes. *Electrochem. Solid-State Lett.* **14,** A130–A133 (2011).

257. Komaba, S. *et al.* Fluorinated ethylene carbonate as electrolyte additive for rechargeable Na batteries. *ACS Appl. Mater. Interfaces* **3,** 4165–4168 (2011).

258. Ponrouch, A., Goñi, A. R. & Palacín, M. R. High capacity hard carbon anodes for sodium ion batteries in additive free electrolyte. *Electrochem. commun.* **27,** 85–88 (2013).

259. Rauh, R. D., Abraham, K. M., Pearson, G. F., Surprenant, J. K. & Brummer, S. B. A Lithium/Dissolved Sulfur Battery with an Organic Electrolyte. *J. Electrochem. Soc.* **126,** 523–527 (1979).

260. Akridge, J. R., Mikhaylik, Y. V & White, N. Li/S fundamental chemistry and application to high-performance rechargeable batteries. *Solid State Ionics* **175,** 243–245 (2004).

261. Manthiram, A., Fu, Y., Chung, S.-H., Zu, C. & Su, Y.-S. Rechargeable Lithium–Sulfur Batteries. *Chem. Rev.* **114,** 11751–11787 (2014).

262. Manthiram, A., Fu, Y. & Su, Y. S. Challenges and prospects of lithium-sulfur batteries. *Acc. Chem. Res.* **46,** 1125–1134 (2013).

263. Gao, J. & Abruña, H. D. Key Parameters Governing Energy Density of Rechargeable Li/S Batteries. *J. Phys. Chem. Lett.* **5,** 140217131902000 (2014).

264. Manthiram, A., Chung, S.-H. & Zu, C. Lithium-Sulfur Batteries: Progress and Prospects. *Adv. Mater.* **27,** 1980–2006 (2015).

265. Cheon, S.-E. *et al.* Rechargeable Lithium Sulfur Battery I. Structural change of sulfur cathode during discharge and charge. *J. Electrochem. Soc.* **150,** A796 (2003).

266. Cheon, S.-E. *et al.* Rechargeable Lithium Sulfur Battery II. Rate capability and cycle characteristics. *J. Electrochem. Soc.* **150,** A800 (2003).

267. Son, Y., Lee, J.-S., Son, Y., Jang, J.-H. & Cho, J. Recent Advances in Lithium Sulfide Cathode Materials and Their Use in Lithium Sulfur Batteries. *Adv. Energy Mater.* **5,** 1500110 (2015).

268. Rosenman, A. *et al.* Review on Li-Sulfur Battery Systems: an Integral Perspective. *Adv. Energy Mater.* **5,** 1500212 (2015).

269. Urbonaite, S., Poux, T. & Novák, P. Progress Towards Commercially Viable Li-S Battery Cells. *Adv. Energy Mater.* **5,** 1500118 (2015).

270. Hagen, M. *et al.* Lithium–Sulfur Cells: The Gap between the State-of-the-Art and the Requirements for High Energy Battery Cells. *Adv. Energy Mater.* **5,** 1401986 (2015).

271. Eroglu, D., Zavadil, K. R. & Gallagher, K. G. Critical Link between Materials Chemistry and Cell-Level Design for High Energy Density and Low Cost Lithium-Sulfur Transportation Battery. *J. Electrochem. Soc.* **162,** A982–A990 (2015).

272. Zhang, S. S. & Tran, D. T. A proof-of-concept lithium/sulfur liquid battery with exceptionally high capacity density. *J. Power Sources* **211,** 169–172 (2012).

273. Gao, J., Lowe, M. A., Kiya, Y. & Abruña, H. D. Effects of Liquid Electrolytes on the Charge–Discharge Performance of Rechargeable Lithium/Sulfur Batteries: Electrochemical and in-Situ X-ray Absorption Spectroscopic Studies. *J. Phys. Chem. C* **115,** 25132–25137 (2011).

274. Park, C.-M., Hwa, Y., Sung, N.-E. & Sohn, H.-J. Stibnite (Sb_2S_3) and its amorphous composite as dual electrodes for rechargeable lithium batteries. *J. Mater. Chem.* **20,** 1097–1102 (2010).